Title
Aerodynamics and optimal design of biplane wind turbine blades

Author
Chiu, Phillip

Publication Date
2017

Peer reviewed|Thesis/dissertation

UNIVERSITY OF CALIFORNIA
Los Angeles

Aerodynamics and optimal design of biplane wind turbine blades

A dissertation submitted in partial satisfaction
of the requirements for the degree
Doctor of Philosophy in Aerospace Engineering

by

Phillip Chiu

2017

ABSTRACT OF THE DISSERTATION

Aerodynamics and optimal design of biplane wind turbine blades

by

Phillip Chiu
Doctor of Philosophy in Aerospace Engineering
University of California, Los Angeles, 2017
Professor Richard E. Wirz, Chair

In order to improve energy capture and reduce the cost of wind energy, in the past few decades wind turbines have grown significantly larger. As their blades get longer, the design of the inboard region (near the blade root) becomes a trade-off between competing structural and aerodynamic requirements. State-of-the-art blades require thick airfoils near the root to efficiently support large loads inboard, but those thick airfoils have inherently poor aerodynamic performance. New designs are required to circumvent this design compromise. One such design is the "biplane blade", in which the thick airfoils in the inboard region are replaced with thinner airfoils in a biplane configuration. This design was shown previously to have significantly increased structural performance over conventional blades. In addition, the biplane airfoils can provide increased lift and aerodynamic efficiency compared to thick monoplane inboard airfoils, indicating a potential for increased power extraction.

This work investigates the fundamental aerodynamic aspects, aerodynamic design and performance, and optimal structural design of the biplane blade. First, the two-dimensional aerodynamics of biplanes with relatively thick airfoils are investigated, showing unique phenomena which arise as a result of airfoil thickness. Next, the aerodynamic design of the full biplane blade is considered. Two biplane blades are designed for optimal aerodynamic loading, and their aerodynamic performance quantified. Considering blades with practical chord distributions and including the drag of the mid-blade joint, it is shown that biplane blades have comparable power output to conventional monoplane designs. The results of this

analysis also show that the biplane blades can be designed with significantly less chord than conventional designs, a characteristic which enables larger blade designs. The aerodynamic loads on the biplane blades are shown to be increased in gust conditions and decreased under extreme conditions. Finally, considering these aerodynamic loads, the blade mass reductions achievable by biplane blades are quantified. The internal structure of the biplane blades are designed using a multi-disciplinary optimization which seeks to minimize mass, subject to constraints which represent realistic design requirements. Using this approach, it is shown that biplane blades can be built more than 45% lighter than a similarly-optimized conventional blade; the reasons for these mass reductions are examined in detail. As blade length is increased, these mass reductions are shown to be even more significant. These large mass reductions are indicative of significant cost of electricity reductions from rotors fitted with biplane blades. Taken together, these results show that biplane blades are a concept which can enable the next generation of larger wind turbine rotors.

The dissertation of Phillip Chiu is approved.

Jeffrey D. Eldredge

Ertugrul Taciroglu

Xiaolin Zhong

Richard E. Wirz, Committee Chair

University of California, Los Angeles

2017

To my family.

TABLE OF CONTENTS

List of Figures

List of Tables

ACKNOWLEDGMENTS

I would like to thank my academic advisor Professor Richard Wirz for his mentorship, motivation, and enduring optimism for my research over the course of my graduate career. I thank my committee for their guidance – Professors Xiaolin Zhong, Jeffrey Eldredge, and Ertugrul Taciroglu.

I would also like to acknowledge the support of my fellow graduate students, many of whom became friends, confidantes, tennis partners, and more. Specifically, I would like to thank Perry Roth-Johnson, whose graduate work paved the way for the structural analyses here, and who never hesitated to lend his support in any way possible, in or out of the lab. I only have the best memories of our years shared in a tiny office and the middle-of-nowhere conferences we attended together.

A number of undergraduate researchers also contributed to this work. I thank Alex Baker, for solid modeling of wind tunnel test articles; Sennan Sulaiman for helping to get structural analysis tools up and running; Christos Voutsaras for working on the development and validation of cross sectional modeling tools.

My family has provided me unwavering encouragement in my pursuits, academic and otherwise, and has inspired me in ways they may not know. I thank my mom, whose strength and sharp wit I can only hope I've inherited a fraction of. I thank my dad, who encouraged me to tinker at a young age. I thank my sister, who continues to inspire me as a model of kindness.

I gratefully acknowledge the financial support of the Link Foundation Energy Fellowship, as well as the California Energy Commission for sponsoring some of the early work.

Finally, I would like to acknowledge the staff of the UCLA Mechanical and Aerospace Engineering department. I can only imagine the number of forms filled out and calls made by Angie Castillo, Abel Lebon, Lance Kono, and others on my behalf.

VITA

2008	B.S., Mechanical Engineering with Honors, UC Davis.
2009	Graduate Researcher, Materials Science Technologies, Los Alamos National Laboratories.
2009–2010	UCLA Mechanical and Aerospace Engineering, Departmental Fellow.
2011–2013	Link Foundation Energy Fellow.
2012	M.S., Mechanical Engineering, UCLA.
2013–2015	Teaching Assistant, Mechanical and Aerospace Engineering, UCLA.
2014–2016	Graduate Researcher, Wind Energy Technologies, Sandia National Laboratories.
2015–2016	Teaching Fellow, Mechanical and Aerospace Engineering, UCLA.
2016–present	Research Engineer, Envision Energy.

PUBLICATIONS

P. K. Chiu and R. E. Wirz. "Aerodynamic Performance of Biplane Airfoils for Wind Turbine Blades," in AWEA Windpower, (Atlanta, GA). Jun. 2012 (presentation).

D. C. Maniaci, P. K. Chiu, and C. Kelley "Assessment of Scaled Rotors for Wind Tunnel Experiments.," *Sandia National Laboratories Technical Report*, SAND2015-5850R, Jul. 2015.

P. K. Chiu and R. E. Wirz, "Optimal Aerodynamic Design of a Biplane Wind Turbine Blade," in *34th Wind Energy Symposium, SciTech 2016*, AIAA 2016-1266, (San Diego, CA), Jan. 2016. doi: *10.2514/6.2016-1266*

P. K. Chiu and R. E. Wirz, "Effects of airfoil thickness in potential flow over biplanes," (in review), 2017.

P. K. Chiu and R. E. Wirz, "Biplane Wind Turbine Blades - Aerodynamic Design, Performance, and Loads," (in review), 2017.

P. K. Chiu and D. C. Maniaci, "Investigation of wind tunnel wall effects on loading and wake development of HAWTs using a free-wake vortex method," *Sandia National Laboratories Technical Report*, (in press), 2017.

P. K. Chiu and R. E. Wirz, "Mass Reductions Enabled by Biplane Wind Turbine Blades," (in review), 2017.

CHAPTER 1

Introduction

1.1 Wind energy – resource and background

Wind energy is a major source of renewable energy throughout the world. For example, the United States alone has between 8.2 TW and 13.9 TW available onshore* [2], with more available offshore. The highest quality land-based resources are concentrated in the central plains, while off-shore resources are located along the country's major coastlines, as seen in Figure 1.1.

In 2008, the U.S. Department of Energy set a goal to produce 20% of its electricity from the wind by 2030[4]. This target was a response to rising energy prices, uncertainty of supply in fossil fuels, and environmental changes. All of these concerns could be eased with a larger portfolio of clean and renewable wind-generated electricity. In the year 2014, about 4.44% of all generated electrical energy was produced from wind power [5].

The installation of wind turbines is driven primarily by the cost of electricity (COE) that can be produced from them. Reducing the COE increases the penetration of wind energy in two ways. First, cheaper wind-generated electricity could be more cost-competitive with conventional sources of electricity, such as coal and natural gas. Second, reducing COE could enable installations in locales which were previously economically infeasible.

One way to reduce costs is through subsidies; this approach has been taken by the United States with its Production Tax Credit, as well as other countries including China, the United Kingdom, and Denmark. A more direct approach is to reduce the cost of wind-generated electricity through technological improvements to the turbines themselves.

*These estimates are based on turbine hub heights ranging from 80 m to 140 m.

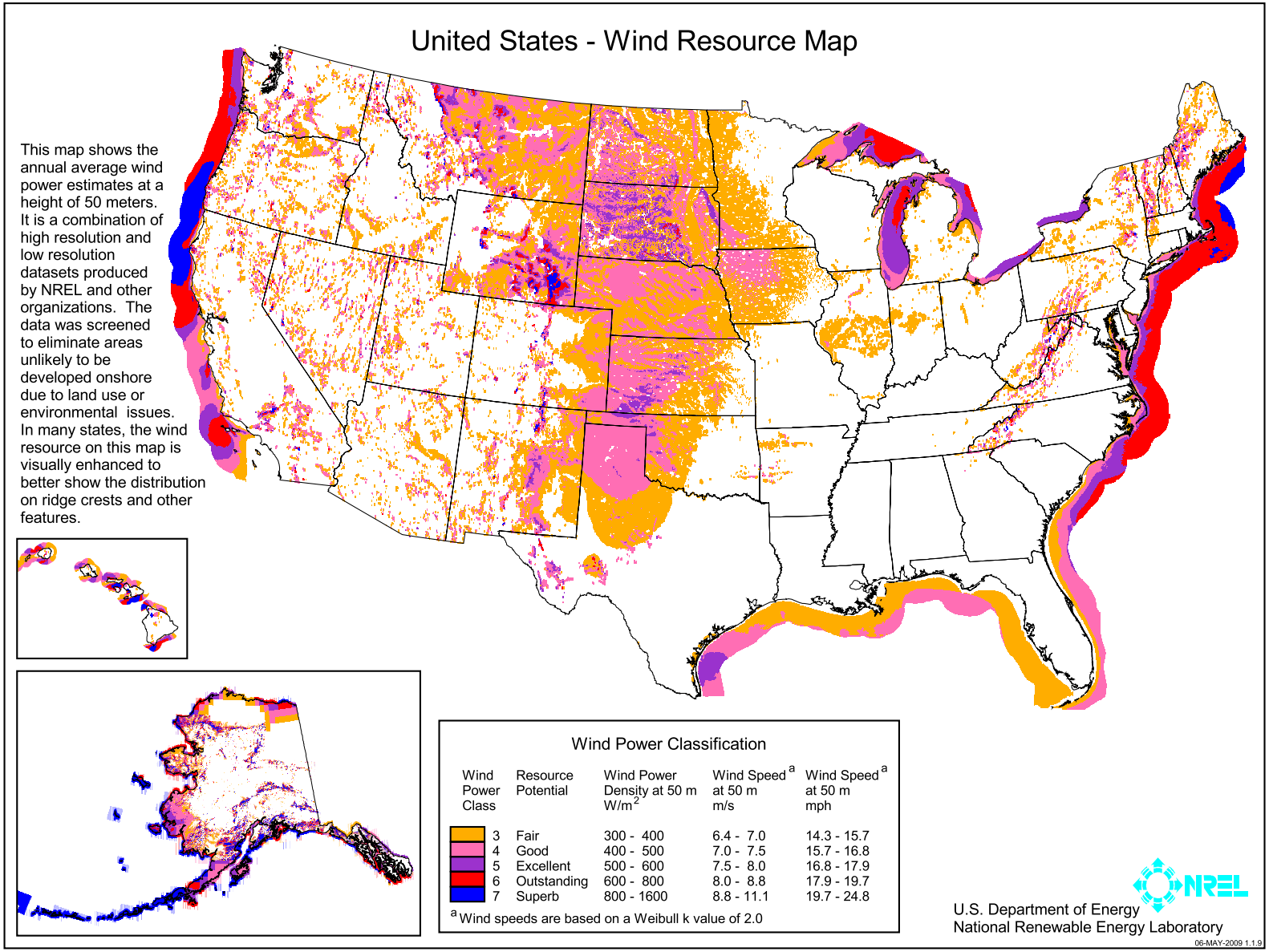

Figure 1.1: Map of the wind resource at a 50 m height in the United States. Onshore, high quality winds are concentrated in the central plains, while good off-shore resources are located along the country's coastlines. [3]

To first order, the cost of electricity, or COE, of electricity produced from a turbine may be given by the relation

$$\text{COE} \propto \frac{\text{C}}{\text{AEP}} \tag{1.1}$$

where C is the total cost of a turbine over it's lifespan – this includes materials, manufacturing, transportation, installation, and maintenance – and AEP is the annual energy production of the turbine. It follows that the COE can be reduced be reduced either by increasing the energy production or reducing the cost.

Improvements to turbine rotors, the principle component responsible for extracting energy from the wind, affect both terms in this relation to decrease COE. Increasing rotor performance directly increases turbine power output and thus the AEP. Decreasing rotor cost, which accounts for 10%-25% of the total turbine cost [6], can also also play a significant factor in reducing the COE. In addition, reducing rotor mass reduces dynamic loading and may also enable cost-reductions in downstream components such as the gearbox, bearings, and tower. For reference, a schematic of a turbine is shown in Figure 1.2.

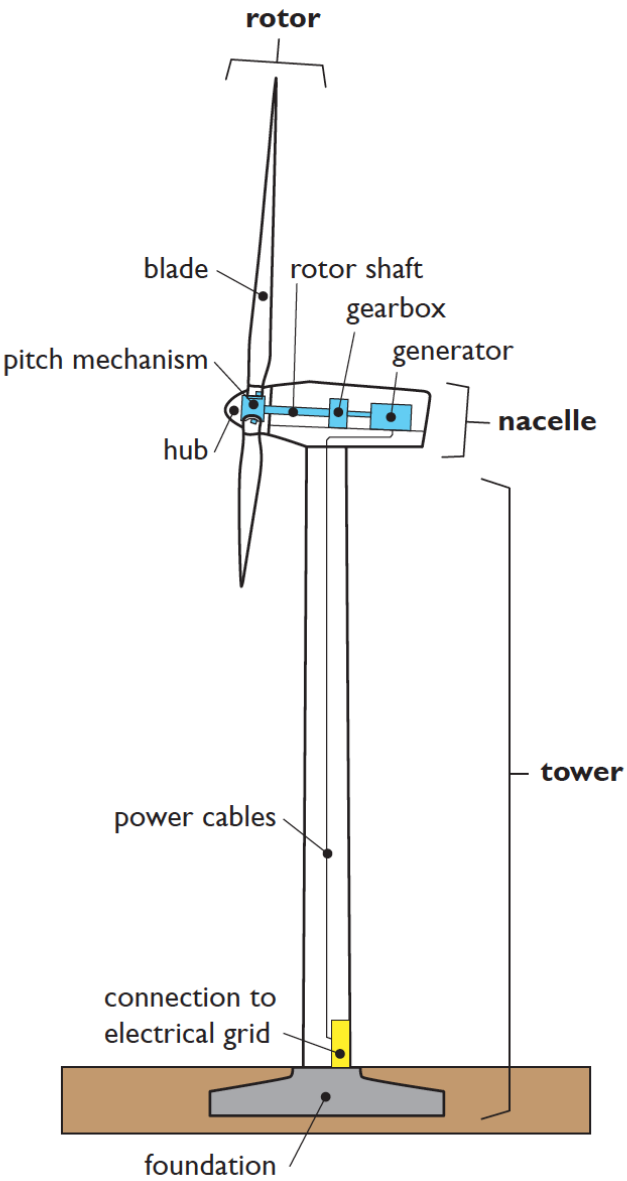

Figure 1.2: Key mechanical components of wind turbines. Figure reproduced from [7], and originally adapted from [8].

1.2 A trend towards larger turbines

Wind turbine blades have grown dramatically over time; the blades of today are ten times longer than the largest blades of the early 1980. This trend towards larger wind turbine blades (Figure 1.3) has been driven by technical and economic factors which seem to indicate that the cost of wind-generated electricity is cheaper from larger turbines.

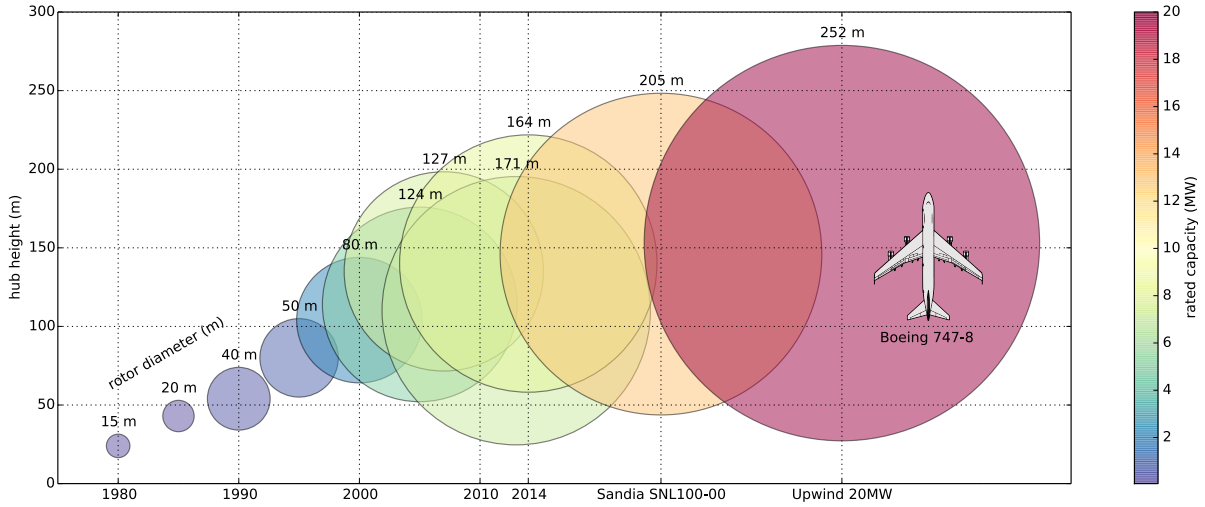

Figure 1.3: Height, size, and power of wind turbines over time: hub height (y-axis position of circle centers), rotor diameter (size of circles), and rated capacity (color of circles). Wind turbines have grown dramatically from 1980 to 2014 [4, 9, 10, 11, 12, 13]. Researchers are focused on developing even larger tubine concepts for the future: the Sandia 100-m blade [14] and the Upwind 20MW turbine [15]. Taller hub heights can access faster winds and larger rotor diameters can capture more wind, both of which increase turbine power. Figure reproduced from [7].

This trend can be partially explained by the following equation

$$P_{\text{rotor}} = \frac{1}{2} C_P \rho \pi R^2 V^3 \tag{1.2}$$

which states that a rotor's power extraction is determined by the power coefficient of the rotor C_P, the air density ρ, the rotor radius R, and the velocity of the wind V. A turbine's power output scales with the swept area of its rotor, or with R^2. Larger turbines are also taller, and can reach faster winds higher in the terrestrial boundary layer, which is significant

since the power output scales with V^3. Both of these indicate that larger turbines are able to produce more power than smaller ones [7]. Larger rotor sizes are also enabling for sites with lower average wind speeds.

This explanation addresses only the power output of a single turbine. However, wind farms also benefit from scale. Larger turbines can extract more power from for the same footprint, which allows for more energy to be produced from the same site. This is a strong consideration when siting costs are high, or the resource area small. In wind farms, larger turbines are also correlated with reduced costs (per unit energy) of infrastructure required to transmit wind-generated electricity to the grid [16].

In order to further drive down COE, the next generation of wind turbines will require blades which are longer than the current state of the art. Longer blades will also be enabling for accessing lower wind speed sites, both on- and off-shore, many of which are located near densely populated areas. Recently-built offshore turbines rated at 7+ MW feature blades in excess of 80 m [11]; researchers continue to investigate the feasibility of 100 m [14, 17] and 120 m [18] blades. The 120 m long blades are projected to weigh as much as 160 t per blade – as discussed in the following section, such massive blades demand transformative design changes.

1.3 Upscaling of turbine blades

A simple approach to design large wind turbine blades would be to isometrically upscale them. However this approach is problematic for a number of reasons.

A high-level view of the problem can be taken using the "square-cube law," which states that the mass of an isometrically upscaled object scales with the square of its area. This has direct application to wind turbines blades – a turbine's power output scales with its area and thus R^2, while its mass (and thus cost) scales with the R^3. This seems to indicate that there exists a critical size above which an isometrically upscaled turbine is no longer economical. Alternately, it can be interpreted that the ability to scale blades even larger requires technological innovations to drive down blade mass – a technology which allwos

blade radius to be increased with a smaller penalty in blade mass enables longer

In addition to the economic problem, geometrical upscaling is not feasible for technical reasons. While stresses due to aerodynamic loads in geometrically-upscaled blades are shown to be scale invariant, those due to gravitational loads are shown to increase linearly with scale [16, 6]. Stresses due to gravitational loads typically require that material be added to combat fatigue damage. This indicates that above a certain scale, additional material will be necessary to maintain constant stresses with smaller-scale designs. Blade lengths are primarily limited by this penalty of weight growth [14].

1.4 Design challenges for large turbine blades

Wind turbine blades are designed to minimize the cost of electricity. In practice, this is a complex and highly constrained multi-disciplinary optimization problem. Blades must have good aerodynamic performance, but must also withstand large bending moments from aerodynamic loads, self-weight, and structural dynamic loads. The blades should be stiff to avoid tower strike for upwind turbines, but should also be light to ensure good dynamic response. Further coupling arises from the fact that aerodynamic performance and loads are closely related.

These design objectives are often in direct contention; the thin, streamlined profiles associated with high aerodynamic effiency have low second area moments in the "flapwise" direction, leading to poor structural efficiency. As such, the design of the inboard region, where bending moments are largest, is a compromise. Typical blade designs use thick airfoils inboard in order to fit the tall internal load-bearing spar structure needed to endure bending loads, but these thick airfoils have poor aerodynamic performance [19], reducing overall aerodynamic performance. Cross-sections near the root are typically cylindrical, both for structural reasons and to ensure compatibility with the hub, and gradually transition to airfoils. At a radial location 15% from the blade root, the airfoil thickness on conventional blades may be as thick as 40% [14].

As a result of the poor aerodynamic performance of thick inboard airfoil sections, the

inboard region of traditional blade designs is often *underloaded* – the lift force produced inboard is significantly lower than what is required for maximum energy capture [20]. This lift force can be increased either by using airfoils with higher lift coefficient, C_l, or by increasing the chord length, c, of airfoils. The lift coefficient is limited by the thick airfoils which must be used inboard, while the chord length inboard is limited by mass requirements, manufacturing capability, and transportation constraints[†] [20].

This aerodynamic underloading, characteristic of traditional blade designs, results in inefficient power extraction. Recent investigations have demonstrated that increased loading in the inboard region of large blades can improve total power output 5-8% [21, 22, 23]. With regards to aerodynamic performance, this indicates that the inboard region is one aspect of blade design which could be greatly improved.

1.5 Towards new blade designs

Considering Eq. (1.1), there are two blade design objectives for reducing a turbine's cost of electricity:

1. reduce blade cost (often through reduction of blade mass)

2. improve aerodynamic performance

In search of reduced blade cost, an approach often taken is to seek reduced blade mass. This is because blade cost is proportional to the material cost, and because accurate cost models are not available in the public domain [24]. Researchers have used numerical optimization to find composite layups for conventional blade designs which minimize blade mass [25, 24]. Similarly, topology optimization has been used in an attempt to discover cross sectional configurations with increased structural efficiency compared to conventional configurations [26, 27]. In both approaches, constraints are imposed to ensure that struc-

[†]Above a certain size, road transportation becomes increasingly costly. In the United States, standard trailer dimensions are limited to loads of 4.1 m high by 2.6 m; loads higher than 4.83 m in height require expensive rerouting [4].

tural design requirements are satisfied. Advanced composite materials, such as carbon fiber, [17] have also been considered; while these materials have improved stiffness-to-weight ratios and can reduce blade mass, the material cost and the additional cost of integrating these materials in the manufacturing process must also be considered [28].

Improved aerodynamic performance has also been an area of continued research interest. The review here is limited to solutions which seek to improve the aerodynamic performance of the inboard region of the blade. Many have investigated the design of high thickness airfoil shapes for improved maximum lift coefficient [29, 30, 31, 32]. Notable improvements have been made to the inboard region with blunt trailing-edge "flatback" airfoils, which have both aerodynamic and structural advantages over standard thick airfoils. Structural advantages include a higher moment of inertia, contributing to increased bending stiffness for the same mass. Aerodynamic advantages include higher lift and reduced sensitivity to surface soiling [33, 19, 34, 35]. Flatback airfoils are now commonly in use in mass-production blades.

Alternatively, a number of blade concepts have been proposed which use multiple airfoils to improve aerodynamic performance inboard. These "multi-element" blade designs all seek to improve turbine performance by increasing lift and aerodynamic efficiency inboard [36, 37, 22, 20]. The aerodynamic benefits of such concepts are clear. Multi-element airfoils have higher lift coefficients than conventional airfoils, and can be used to increase the aerodynamic loading of the inboard region without increasing chord length. Multi-element airfoils can also be designed for increased aerodynamic efficiency compared to conventional thick airfoils, reducing parasitic drag. Some multi-element airfoil configurations (for example, leading edge slats) are also attractive as "add-ons" which can be used to retrofit existing turbines and improve power ouput by increasing inboard loading.

Despite these aerodynamic improvements, a shared challenge for multi-element designs is in their structural implementation; none of the aforementioned multi-element concept studies address this aspect. In the case of the leading edge slats [20], at operational angles of attack, a large proportion of the lift force comes from the much smaller slat. This presents a structural challenge as the small, heavily loaded slat must be securely attached to the blade. Some methods for attaching such slats to a blade have been proposed [38], but are

(a) Leading-edge slat concept of [22, 20]

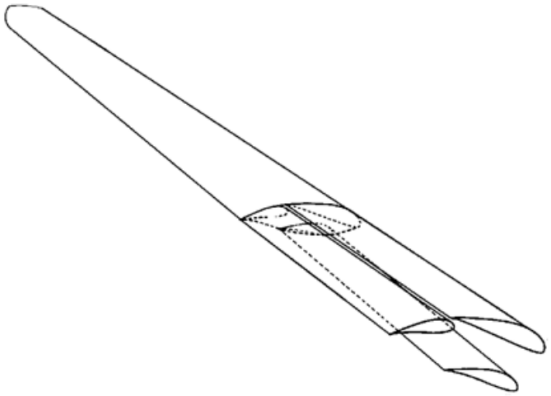

(b) Multi-element concept of [36]

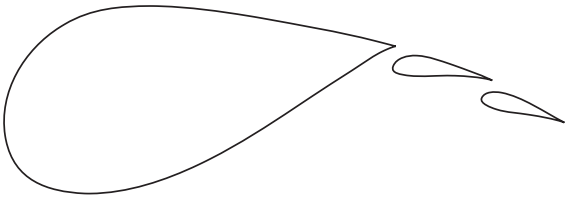

(c) Multi-element concept of [37]

Figure 1.4: Multi-element blade concepts

not demonstrably practical. In other multi-element concepts, for example, that of [36], it is difficult to conceptualize a structural implementation at all.

1.6 The biplane blade

Wirz [39] and others [40] proposed the biplane blade, a multi-element design which has the potential to improve both the structural and aerodynamic performance of the inboard region (Figure 1.5). In this design, a biplane inboard section merges to a monoplane outboard. The blade root transitions to a cylinder which can be bolted on to a conventional hub.

The biplane design replaces the thick single airfoil of the conventional blade with two thinner airfoils in a biplane configuration; this configuration has increased lift and aerodynamic efficiency. Increased lift can reduce underloading in the inboard region, while improved aerodynamic efficiency can minimize drag losses typical to the thick inboard airfoils of traditional designs. The 2-D aerodynamic benefits were first described by Wirz & Johnson, who used computational fluid dynamics (CFD) to show that a canonical biplane airfoil had improved maximum lift and aerodynamic efficiency over thick airfoils [39]. Brodsgaard also used CFD to investigate the 2-D aerodynamics of biplane airfoils, demonstrating similar aerodynamic improvements [41]. That work further explored the 2-D aerodynamic design of biplane airfoils through computational optimization, manipulating the relative positioning and camber of biplane airfoils in order to design a biplane airfoil with maximal lift coefficient and aerodynamic efficiency.

Perhaps more significantly, and in contrast to other multi-element concepts, the biplane blade has demonstrated structural improvements over traditional designs. The structural performance of the biplane blade was first investigated by Wirz and Roth-Johnson [39]; a simplified biplane blade was shown to have 30% better resistance to flapwise tip deflection than a monoplane structure of the same mass. Similar benefits were observed by Brodsgaard [41]. Follow-on analyses of a more complex biplane blade spar (a 100-meter tapered spar made of composite materials) reaffirmed the preliminary results [42, 7]. These analyses also showed a reduction in bending moment at the blade root – bending moments are carried as

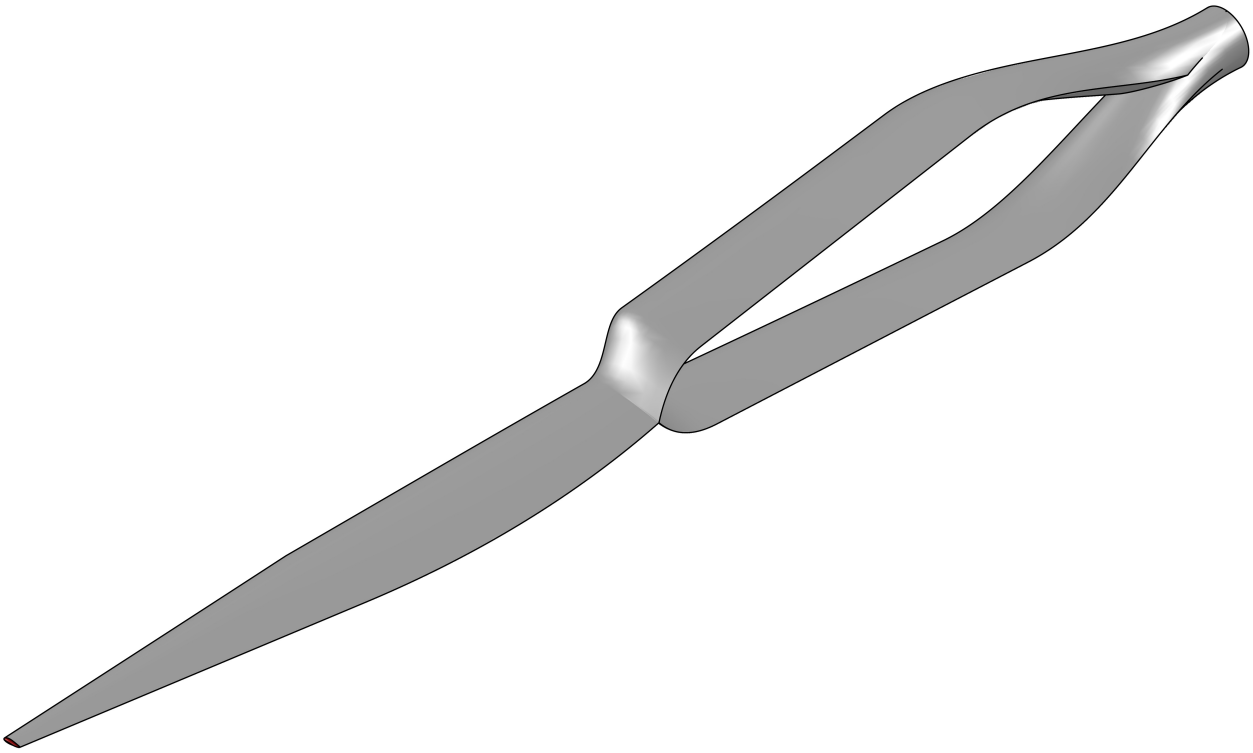

Figure 1.5: The biplane blade design uses a biplane inboard and merges to a single airfoil (monoplane) towards the tip.

axial load in the branches of the biplane.

These aerodynamic and structural benefits indicate that the biplane blade concept has the potential to improve both power output and reduce the mass/cost of wind turbine blades. However, a number of open questions remain regarding the 2-D aerodynamics, the overall rotor performance, the aerodynamic loads, and the structural design of biplane blades. Most importantly, it is unknown how these factors come together in the holistic, multi-disciplinary blade design process.

1.7 Objective and Overview of Dissertation

In an effort to assess the viability of the biplane blade concept for future large wind turbines, this thesis investigates a number of open issues related to the aerodynamics and design of biplane wind turbine blades. The overall objective of this work is to improve the understanding of the aerodynamics and design advantages/challenges of biplane wind

turbine blades to the level where these blades may be considered for commercial application. A general theme is to use low-fidelity models where possible to reveal the physics, phenomena, and trends of interest. The work is divided into three main sections, each summarized below.

For structural reasons, the biplane sections used in biplane wind turbine blades need to use thick airfoils in the inboard region [7]. The aerodynamic performance of biplanes with thin airfoils has been investigated extensively, but those of biplanes with thick airfoils has not. In Chapter 2 the lift performance of biplanes with thick airfoils are investigated. Due to the high Reynolds numbers and low Mach numbers experienced in the inboard part of large turbine blades, an inviscid, incompressible simplification is taken. Key phenomenona related to the lift of biplanes with thick airfoils are revealed.

While past studies sought to quantify and optimize the aerodynamic performance of 2-D biplane airfoils wind turbines, the overall aerodynamic design of the blade itself has not been considered in detail. In addition, the maximum achievable rotor performance, and aerodynamic blade loads of biplane wind turbine blades have not quantified. In Chapter 3, these issues are examined using blade element momentum (BEM) theory. It is shown that the aerodynamic performance of biplane blades is comparable with that of monoplane blades, but at the expense of increased loads under gust conditions. Under other certain extreme conditions, the loads on biplane blades are shown to be reduced.

The design of wind turbine blades is not only an aerodynamic problem; the aerodynamic performance, aerodynamic loads, and structural performance must all be considered simultaneously. This multi-disciplinary design problem is investigated in Chapter 4, which considers the internal structural design of biplane blades for minimum mass subject to realistic aerodynamic loads and design constraints. Through numerical optimization, it is shown that biplane blades can be built *significantly* lighter than conventional blade designs, indicating the potential for significant COE reductions from turbines fitted with biplane blades.

Finally, the impact of these studies is summarized, and ideas for improvements to and extensions of this work are discussed in Chapter 5.

CHAPTER 2

Effects of airfoil thickness in potential flow over biplanes

Airfoil thickness has been shown in the past to be important to the aerodynamic performance of biplanes. In this work we investigate how system and individual force coefficients are affected by increasing airfoil thickness for biplanes in two-dimensional, incompressible potential flow. A panel method is used to compare the aerodynamic performance of biplanes with varying airfoil thickness (12% to 35%), gap (0.5 to 1.0 chord), and stagger (-0.75 to 0.75 chord). Airfoil thickness is shown to increase lift-reducing interference and, when the two airfoils are staggered, to produce an effective camber which shifts the system lift curve. An acceleration of fluid is observed between the two airfoils, leading to an attractive force which strongly contributes to both lift and drag forces on the individual airfoils; this acceleration also strongly modifies the pressure distributions on the inner airfoil surfaces. The results demonstrate that airfoil thickness effects in biplanes can be significant, particularly on the individual airfoil forces, and should be taken into consideration when designing biplanes with thick, closely-interacting airfoils.

2.1 Introduction

In the early days of aviation, biplane wings were popular due to their high lift per span, structural rigidity, and simple construction. These biplane wings typically used very thin airfoils with structural support provided by external struts or wires. The external supports suffered from high drag; as the design and construction of internally-braced monoplane wings improved, biplane wings fell out of favor among aircraft designers. In more recent years, biplanes have been proposed for a number of specialized applications, such as cargo transports [43] and sensorcraft [44]. Biplane airfoils have also been suggested as a method of improving the aerodynamic performance of wind turbine blades [40, 41, 45, 42, 46]; the wind turbine application is the original motivation for the investigation herein. Compared to the biplanes of the early 1900s, these modern biplane wing and blade configurations would require thicker, internally-braced airfoils. These applications, and others (including biological ones [47]), have brought renewed interest in the aerodynamics of biplanes.

Considerable effort was devoted to understanding the aerodynamics of biplanes in the early 20th century. Much of this work investigated how the aerodynamic performance of biplane configurations changed with the relative positioning of the two airfoils, commonly parameterized by the *gap*, *stagger*, and *decalage* as shown in Figure 2.1, and investigated biplanes with thin airfoils (12% or less). Increased thickness, however, has been shown to increase the interaction between the two airfoils and to affect the performance of the biplane system [48]. A review of previous efforts relevant to the study herein is presented in Section 2.2.

The objective of this work is to develop a qualitative understanding of the aerodynamic phenomena responsible for the performance of biplanes with thick airfoils and varying gap and stagger. In particular, we focus on biplanes with thick airfoils at small staggers (of less than a chord length). We limit our analyses to incompressible potential flow which, which, despite their simplicity, reveal important aerodynamic phenomena. This flow regime (very high Reynolds number, low Mach number), is the one in which airfoils in the inboard region of large wind turbine blades operate, as the chord lengths and thus Reynolds numbers are

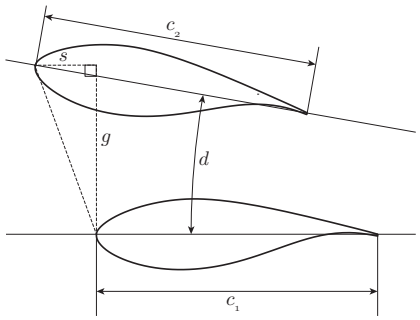

Figure 2.1: The relative position of airfoils in a biplane configuration can be described by the gap, g, stagger, s, and the decalage angle, d. The conventions shown indicate positive stagger (upper airfoil leading) and decalage (upper airfoil at a higher angle of incidence than the lower).

large, but the velocities low.

In this study, we first use an approximate lumped vortex approach to demonstrate some of the qualitative flow phenomena and lift characteristics of biplanes with infinitely thin airfoils. We then use a panel method to solve for the flow field around a number of two-dimensional biplane configurations with appreciably thick airfoils. From these results, we identify key aerodynamic phenomena and investigate how their effects vary with changes in airfoil thickness and relative positioning (gap and stagger). The system lift and individual airfoil loads of these biplanes are compared to those of biplanes with thin airfoils from the lumped vortex method and the literature.

2.2 Review of biplane aerodynamics

Many researchers have investigated the aerodynamic performance of biplanes using theoretical, experimental, and numerical methods. A summary of key results follows.

In 1918, Norton [49] experimentally investigated the effect of stagger on the aerodynamic performance of two wings in a biplane configuration. The gap was fixed at one chord length and the stagger was varied from $-1.0c$ to $+1.0c$. The maximum normal force and aerodynamic efficiency of the wing system were both shown to be increased with increasing positive

stagger (upper wing leading the lower wing). A series of experiments by Knight and Noyes [50, 51, 52] quantified the loads on each airfoil in a finite aspect ratio biplane wing of two airfoils ($t/c = 11.7\%$), and showed how these loads varied with gap, stagger, and decalage. Increased normal force and more equal airfoil loading were shown with increased gap and stagger. Nenadovic [53] was the first to perform two-dimensional wind tunnel measurements. He measured the lift and drag of infinite aspect ratio biplane sections with varying gap, stagger, and decalage. As with the finite aspect ratio studies, he showed increased lift coefficient and reduced drag coefficient when the airfoils were spaced further apart. His results also showed a minimum drag configuration at a gap of 1/3 chord lengths, stagger of 1 chord length, and a decalage of -6 degrees.

Concurrently, analytical methods were developed for biplane aerodynamics. The exact solution for two-dimensional incompressible potential flow over biplanes with thin airfoils was first given by Munk in 1923 [54], using a conformal transformation to solve for the potential flow around two zero-thickness plates. These results provided a way to compute the loads on biplane systems with infinitely thin airfoils. Simpler approximate methods were also developed to quantify the loads. In [55], Millikan used von Karman's thin airfoil theory to find the "disturbance velocity" caused by flow around a single zero-thickness plate. This disturbance velocity was superimposed onto the flow over another airfoil to approximate the flow of a biplane system. Millikan points out that the approximation is valid only for gaps greater than approximately one chord length, limiting the model's applicability. Another class of approximate methods models each airfoil as a point vortex. Enforcing no flow-through at a single point along each airfoil's chord produces a linear system which can be solved for the individual strengths of each vortex. These vortex strengths represent the circulation about each airfoil. These "lumped vortex" models have been applied to the problem of biplanes with thin airfoils [56, 57, 58] and provide a way to calculate both system lift and the individual lifts on each airfoil. Rokhsaz [59] used a vortex filament approach in an effort to qualitatively understand the aerodynamic phenomena about biplanes with infinitely thin airfoils. He showed the existence of an "induced camber" of one airfoil on the other, which was argued in [48] to affect the zero angle of attack lift coefficient, $C_{l,0}$, of the

individual airfoils. For a biplane with positive stagger, the trailing (lower) airfoil is seen to induce a positive camber on the leading airfoil.

The previously mentioned experimental, numerical, and theoretical studies above were limited to biplanes with thin airfoils ($t/c < 12\%$). However, exact solutions for the incompressible potential flow over biplanes with arbitrarily shaped airfoils have also been found. Such solutions rely on transforming the generic airfoil shapes into two stacked lifting cylinders, for which the potential flow solution was given in [60]. An iterative method to map arbitrary shapes to the stacked cylinder problem was developed in [61], and was used to solve for the surface pressures of a specific biplane configuration. This iterative mapping method was later improved upon [62, 63]. Despite the mathematical significance of these exact solutions, few results using these methods appear in the literature. This is likely due to changes in both aircraft design and in computational methods – as construction of internally-braced wings improved, biplane wings fell out of interest. Later on, the advent of general panel methods and increases in computing power made the exact analytical solutions for potential flow obsolete for engineering purposes.

In [59], a two-dimensional panel method was developed to investigate the aerodynamic performance of biplanes, using a one-way integral boundary layer formulation to estimate skin friction drag. This investigation focused on a large stagger and small gap biplane configuration ($s/c = +1.0$, $g/c = 0.26$, $d = -6^\circ$) comprised of two NACA 63(2)-215 airfoils ($t/c = 15\%$). For this particular configuration, which is perhaps more of a tandem configuration than it is a biplane, it was shown that the changes in airfoil surface velocities and pressures led to favorable boundary layer characteristics. At some angles of attack, the biplane configuration showed decreased drag coefficient when compared to the single airfoil, which was attributed to these improved boundary layer characteristics. The effect of airfoil thickness was briefly investigated in [48], wherein a panel method was used to compute the lift and surface pressure coefficients of biplanes with ($s/c = +1.0$, $g/c = 0.26$, $d = -6^\circ$) and airfoils of varying thickness ($t/c = \{6\%, 12\%, 18\%\}$) in two-dimensional, incompressible potential flow. For this relative positioning, it was shown that increased thickness led to increased lift of the lower airfoil and reduced lift of the upper airfoil, however the reasons

for this were not fully explored.

2.3 Preliminary topics

In this section, a few preliminary topics are covered which facilitate later discussion. An aerodynamic performance metric is defined which is useful to compare the amount of *lift interference* in various biplane systems. Next we discuss in-depth the solutions for two cases – biplanes with infinitely thin airfoils (flat plates), and biplanes with cylindrical airfoils (lifting cylinders). These two cases exhibit different aerodynamic phenomena; we later show that the flow around biplanes with thick airfoils has similarities with both.

2.3.1 The biplane lift parameter

We define here the *biplane lift parameter*, and denote it β. This parameter is the ratio of the biplane system lift to the sum of the individual airfoils' lifts if each airfoil were flying independently. Using the superscript I to denote the independent airfoil case, β can be written as

$$\beta(\alpha^*) = \frac{C_{l,\text{biplane}}(\alpha^*_{\text{biplane}})}{\frac{1}{2}\left(C^I_{l,\text{lower}}(\alpha^*_{\text{lower}}) + C^I_{l,\text{upper}}(\alpha^*_{\text{upper}})\right)} \tag{2.1}$$

The parameter α^* is the camber-corrected angle of attack, and is given by $\alpha^*_i = \alpha - \alpha_{0,i}$, where $\alpha_{0,i}$ is the angle of attack at which the lift coefficient of airfoil i is zero. In this work, we consider only biplanes with identical upper and lower airfoils. In such cases the biplane lift parameter simplifies to

$$\beta(\alpha^*) = \frac{C_{l,\text{biplane}}(\alpha^*_{\text{biplane}})}{C^I_{l,\text{mono}}(\alpha^*_{\text{mono}})}, \quad \text{lower} = \text{upper} \tag{2.2}$$

The lift coefficient of biplanes and monoplanes are both non-dimensionalized using the total wing area, or in 2-D, the total chord length. With these non-dimensionalizations and assuming biplanes with matching airfoils, we can give meaning to the value of β at different

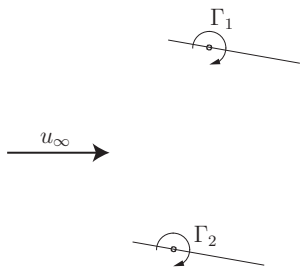

Figure 2.2: Biplane with infinitely thin airfoils.

values. When $\beta = 1$, the lift force produced by a biplane system of wing area S is equal to that which would be produced by a monoplane of the same airfoil and wing area. For $\beta < 1$, the lift of the system is less than if the airfoil were flying alone. Thus, β is a measure of lift-reducing *interference* between the airfoils; when $\beta = 1$, interference has no detrimental effect on the lift. In general, β is a function of the angle of attack, α, the airfoil shapes, and their relative positioning.

2.3.2 Exact solution for biplanes with thin airfoils

The exact potential solution for a biplane with two infinitely thin airfoils (Figure 2.2) was first developed by Munk [54]. His solution used a conformal map to transform two flat plates in a biplane configuration to two flat plates in tandem.

Munk showed that for a biplane with unstaggered, symmetric (uncambered) thin airfoils, the system lift coefficient is equal to

$$C_{l,\text{Munk}} = 2B\pi \sin\alpha \tag{2.3}$$

where α is the angle of attack, and B is a function of the gap to chord ratio g/c and stagger to chord ratio s/c containing elliptic integrals. The value of B approaches unity as g/c or s/c is increased. This result was obtained by evaluating the circulations about the individual

airfoils and employing the Kutta-Joukowski theorem

$$F_x - iF_y = i\rho u_\infty \Gamma \tag{2.4}$$

For a biplane with unstaggered, symmetric (uncambered) thin airfoils, it was shown that the circulations around each airfoil are equal. The lift forces on each airfoil, however, are not equal. While the lift of a solitary body with circulation Γ is given by the Kutta-Joukowski theorem, this relation does not necessarily hold true for a body in the presence of others. As pointed out by Crowdy [64], the proof of the Kutta-Joukowski theorem requires the integration contour (of Blasius' theorem) to be deformed to a region large enough that the circulating body can be approximated by a point vortex. In the case of two (or more) circulating bodies, the presence of the other airfoil prevents such a deformation. Munk demonstrated that the two airfoils in a biplane experience a mutual *repulsive force*, whose magnitude increases approximately as the angle of attack squared (α^2). This repulsive force, which arises from the same-signed circulation about the two airfoils, increases lift on the upper airfoil and decreases lift on the lower airfoil, resulting in non-equal lift on the two airfoil forces despite their having equal circulations. The repulsive force also results in a drag force on both airfoils, the sum of which is equal to zero.

While mathematically significant, the solution of Munk can be difficult to interpret. This is due to its conformal mapping approach, which transforms the physical problem to a non-physical one, and to the existence of elliptic integrals in the coefficients, both of which obscure the dependence on physical parameters.

2.3.3 Approximate solution for biplane with thin airfoils – lumped vortex method

Simpler approximate solutions based on the physically representative "lumped vortex" methods can provide qualitatively similar results to Munk's solution, with clearer insight into the important geometric parameters. In lumped vortex methods, each airfoil is modeled by a point vortex; this implies that the airfoil is infinitely thin. Enforcing no flow-through or flow tangency at a chosen point (the *collocation point*) along each airfoil's chord produces a

linear system which can be solved for the individual strengths of each vortex. These vortex strengths represent the circulations about each airfoil. A number of authors have applied such vortex methods [56, 57, 58] to the problem of biplanes with thin airfoils.

In this section, we develop an approximate solution for the potential flow around biplanes with thin airfoils, generalizing the method of McBain [58] to account for non-zero stagger.

Applying the lumped vortex method to a biplane with equal-length airfoils ($c_1 = c_2 = c$), and a collocation point located at the three-quarter chord point of each airfoil, it can be shown that the circulations about the lower and upper airfoils, Γ_1 and Γ_2 respectively, can be written

$$\begin{aligned} \Gamma_1 &= 2\zeta_1 c\pi u_\infty \sin\alpha \\ \Gamma_2 &= 2\zeta_2 c\pi u_\infty \sin\alpha \end{aligned} \tag{2.5}$$

where ζ_1 and ζ_2 are algebraic, non-dimensional, functions of c, s, and g which are given by:

$$\begin{aligned} \zeta_1 &= \frac{(cs + 2g^2 + 2s^2)\,(c^2 - 4cs + 4g^2 + 4s^2)}{8c^2g^2 - 4c^2s^2 + 16g^4 + 32g^2s^2 + 16s^4} \\ \zeta_2 &= \frac{(-cs + 2g^2 + 2s^2)\,(c^2 + 4cs + 4g^2 + 4s^2)}{8c^2g^2 - 4c^2s^2 + 16g^4 + 32g^2s^2 + 16s^4} \end{aligned} \tag{2.6}$$

The circulations about each airfoil, Γ_1 and Γ_2, are directly proportional to ζ_1 and ζ_2. Noting that the system lift is proportional to the total system circulation, $\Gamma = \Gamma_1 + \Gamma_2$, the system lift coefficient can be computed from 2.4 as

$$C_{l,\mathrm{LV}} = (\zeta_1 + \zeta_2)\, 2\pi \sin\alpha$$

The lumped vortex method can also be used to give the forces on each individual airfoil. The lift force of each vortex (representing an airfoil) can be computed by the Kutta-Joukowski theorem (Eq. (2.4)). In addition to their lifting forces, both vortices also experience a mutual

repulsive force (per unit span), R', whose magnitude is given in [56] by

$$R' = \frac{\Gamma_1 \Gamma_2}{2\pi r}\rho$$

Where $r = \sqrt{g^2 + s^2}$ is the distance between the vortices. This force acts along the line connecting the two vortices. Substituting the circulations from Eq. (2.5) and non-dimensionalizing by $1/2\rho u_\infty^2 c$ gives C_r, the *repulsive force coefficient*

$$C_r = \frac{2\zeta_1 \zeta_2 c}{r} 2\pi \sin^2 \alpha \tag{2.7}$$

It can be seen that C_r is directly proportional to the non-dimensional parameter $\zeta_1\zeta_2 c/r$, and grows with angle of attack as $\sin^2 \alpha$.

The repulsive force acts on the line which connects the two vortices. This force can be decomposed into contributions in the lift and drag directions. For angles of attack between 0 and 90 degrees, a positive repulsive force will increase the lift on the upper airfoil, and decrease lift on the lower airfoil. For cases with stagger, the repulsive force will produce a negative drag force on the leading airfoil and a positive drag force on the trailing airfoil. The sum of these drag forces is equal to zero, in accordance with D'alembert's paradox.

The functions ζ_1/c and ζ_2/c, which are proportional to the individual airfoil circulations, are plotted against the g/c and s/c in Figure 2.3a. These functions give insight into how the lift performance in a lumped vortex biplane varies with airfoil relative positioning. For a fixed gap, positive stagger tends to increase the circulation about the upper airfoil while reducing the circulation about the lower airfoil, up to a certain point. This is an effect of the lower airfoil's upwash increasing the angle of attack on the leading airfoil. Negative stagger has the opposite effect on the airfoil circulations. At zero stagger, the upper and lower airfoils always have equal circulation. The sum of the circulation contributions, which is directly proportional to the total system lift, is shown in Figure 2.3b. It can be seen that increases in both gap and stagger increase the total system circulation and thus system lift coefficient. Last, the function $2\zeta_1\zeta_2 c/r$, which is proportional to the repulsive force, is

plotted in Figure 2.4. It can be seen that the strength of the repulsive force is symmetric about $s/c = 0$, and decreases as gap or stagger are increased.

The biplane lift parameter, β, defined earlier, can be used to evaluate the lift interference predicted by the lumped vortex methods. The lift coefficient for a single flat plate airfoil is given by $C_l = 2\pi \sin\alpha$ [57]. It follows from Eq. (2.2) that β for the lumped vortex methods is independent of α, and is given by

$$\beta_{\text{LV}} = \zeta_1 + \zeta_2$$

Again looking at Figure 2.3a it can be seen that the two lines for $\zeta_1 = 0.5$ and $\zeta_2 = 0.5$ are parallel, indicating that the β is always less than 1 – the lumped vortex method predicts that the lift coefficient of the biplane airfoil will always be less than those of the individual airfoils at a given angle of attack.

2.3.3.1 The unstaggered biplane with equal chord lengths

The further simplified case of unstaggered ($s = 0$) biplanes can provide some more insight into the lift performance. In this case, it follows from from Eq. (2.6) that $\zeta_1 = \zeta_2 = \zeta$, and the circulations about each airfoil are equal. The system lift coefficient simplifies to

$$C_{l,\text{LV}} = 2\zeta\pi \sin\alpha, \quad s/c = 0 \tag{2.8}$$

where

$$\zeta\left(g/c\right) = \frac{4\left(g/c\right)^2 + 1}{8\left(g/c\right)^2 + 4}, \quad s/c = 0$$

The biplane lift parameter for these unstaggered biplanes is equal to

$$\beta_{\text{LV}} = 2\zeta, \quad s/c = 0$$

For comparison, the biplane lift parameter from Munk's solution can be computed as

$$\beta_{\text{Munk}} = B$$

The two parameters β_{Munk} and β_{LV} are compared for a range of gap to chord ratios in Figure 2.5. There is good qualitative agreement between β_{LV} and β_{Munk}, and improved agreement with larger g/c, demonstrating that the lumped vortex method predicts qualitatively similar system lift when compared to the more complicated exact solution. A similar result was previously presented in [56]

Looking at the individual airfoil loads, the lift coefficients of the lower and upper airfoils, $C_{l,1}$ and $C_{l,2}$, respectively, can be written

$$\begin{aligned} C_{l,1} &= 4\pi \left[\zeta \sin\alpha - \frac{c}{g}\zeta^2 \sin^2\alpha \cos\alpha \right] \\ C_{l,2} &= 4\pi \left[\zeta \sin\alpha + \frac{c}{g}\zeta^2 \sin^2\alpha \cos\alpha \right] \end{aligned} \tag{2.9}$$

In each of the above equations, the first term in the brackets is the lift contribution due to each vortex's own circulation, while the second terms are the lift contributions of the repulsive force. As can be seen, the repulsive force increases lift on the upper airfoil and decreases lift on the lower. The strength of the repulsive force scales with ζ^2, and decreases as $\zeta c/g$. Taking a small angle approximation, the influence of the repulsive force on the lift coefficient increases approximately as α^2 – the same relationship was reported in Munk's exact solution for unstaggered biplanes with thin, equal chord length airfoils. Despite its simple approach, the lumped vortex method is able to qualitatively reproduce key characteristics of the exact solution for biplanes with thin airfoils.

The lift coefficients predicted by the lumped vortex method for a thin airfoil biplane with a gap of $g/c = 0.5$ and no stagger $s/c = 0$ are plotted in Figure 2.6. As can be seen, the lumped vortex method predicts that the upper airfoil always generates more lift than the lower airfoil due to the repulsive force between the two airfoils. The discrepancy between the upper and lower airfoil lift increases with angle of attack.

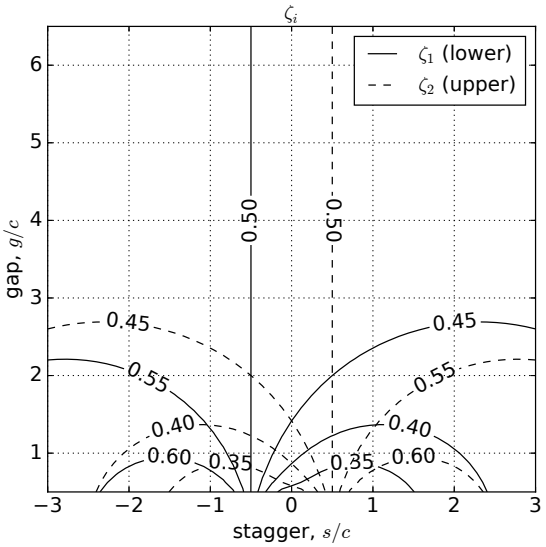

(a) Circulation contribution coefficients of biplanes with equal length airfoils, as predicted by lumped vortex method.

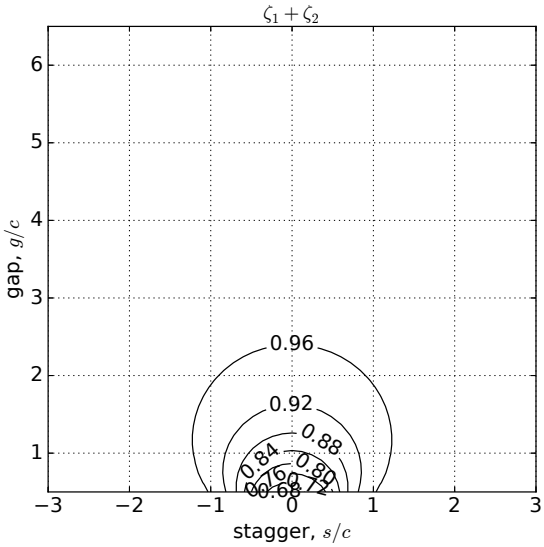

(b) Total circulation of biplanes with equal length airfoils, as predicted by lumped vortex method.

Figure 2.3: Variation in ζ_1, ζ_2 with relative airfoil positioning predicted by the lumped vortex method.

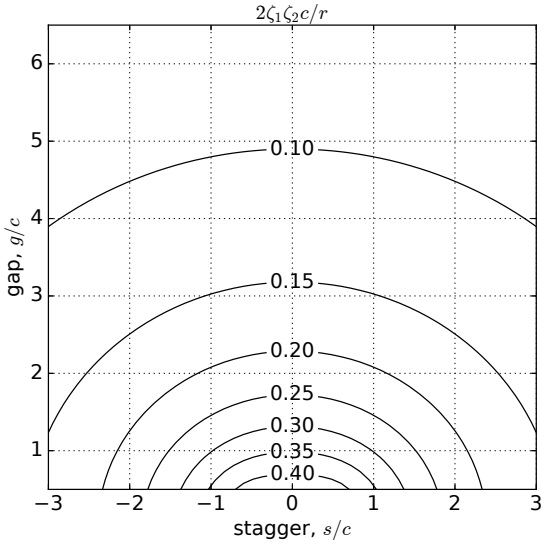

Figure 2.4: Non-dimensional repulsive force influence coefficient for biplanes with equal length airfoils, as predicted by lumped vortex method.

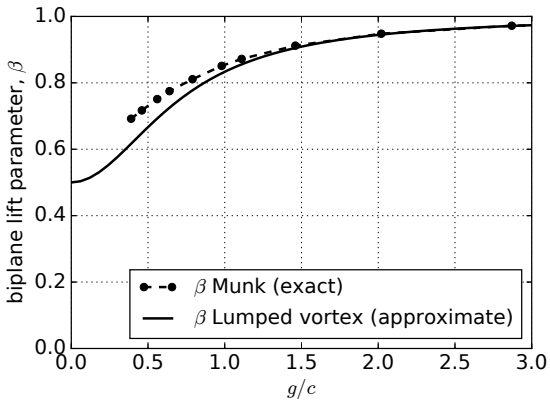

Figure 2.5: Comparison of exact (Munk) and approximate (lumped vortex) lift performance parameter for unstaggered ($s/c = 0$) biplanes with varying gap.

2.3.4 Exact solution for stacked lifting cylinders

The thin airfoil solutions presented above describe the variation of lift and repulsive force with angle of attack for biplanes with thin airfoils. However, both the exact solution of Munk and the approximate lumped vortex solutions neglect the airfoil thicknesses.

The problem of potential flow around stacked lifting cylinders (Figure 2.7) has obvious similarities to the problem of biplanes with thick airfoils. Lagally was the first to develop an exact solution to this problem [60]. Additional insight was provided by Crowdy [64], who examined the individual forces on each cylinder (and proposed an alternative to Lagally's solution that could be generalized to more than two cylinders).

There are a few key differences between the thin airfoil and lifting cylinders cases. First, for the cases with flat plate airfoils, the circulations about each airfoil arise by enforcing external conditions – either the Kutta condition, in the case of Munk's exact solution, or the no flow-through condition for the lumped vortex models. In the case of stacked lifting cylinders, the circulations must be prescribed. Secondly, for biplanes with flat plate airfoils and at zero angle of attack, fluid passes around the airfoils unimpeded. However, for biplanes with cylinders, the same is not true; fluid passing *between* the cylinders experiences an increased velocity and reduced pressure compared to the freestream. This low pressure region results in an apparent "attractive" force between the two cylinders.

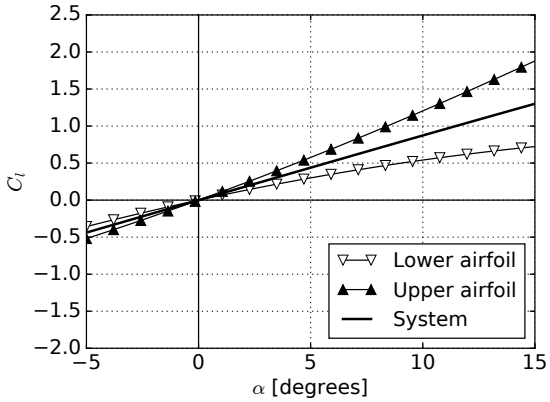

Figure 2.6: Lift coefficient predicted by the lumped vortex method for biplane with equal length airfoils, $g/c = 0.5$, and $s/c = 0$. The upper airfoil has a larger lift than the lower airfoil.

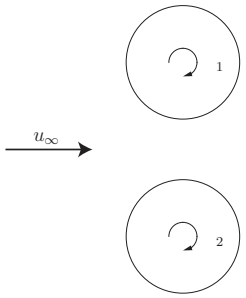

Figure 2.7: Biplane with lifting cylinders. Γ_1 and Γ_2 are the circulations about each cylinder.

This attractive force is in the direction of lift on the lower airfoil and opposite it on the upper airfoil. Crowdy showed that when there is no circulation ($\Gamma_1 = \Gamma_2 = 0$), the cylinders experience a net attractive force. As the circulations are increased, the net attractive force decreases. At larger circulations, the net forces on the cylinders may switch signs, indicating a repulsive force between the cylinders. In light of the discussion above regarding the repulsive force experienced by two vortices, we recognize that this phenomena is due to the competing attractive force, which arises from the low pressure pressure between the two cylinders, and repulsive force, attributable to the same-signed circulation about the two cylinders.

2.4 Biplanes with thick airfoils

We now investigate biplanes with airfoils of moderate thickness. A two-dimensional panel method is used to compute the incompressible potential flow around a number of biplane airfoil configurations. In the panel method, the surface of each airfoil is discretized by a number of vortex sheets (or in two dimensions, vortex filaments) with linear vorticity distributions. No flow-through is enforced at each panel center and tangential flow is enforced at the trailing edge of both airfoils (i.e., the Kutta condition). This method is detailed in [57]; the implementation used in this work is JavaFoil by M.H. Hepperle [65].

The biplanes studied here all use symmetric, uncambered NACA 4-digit airfoils (NACA 0012, NACA 0025, and NACA 0035), shown in Figure 2.8. Only biplanes with airfoils of equal length ($c_1 = c_2 = c$) and with zero decalage ($d = 0$) are considered. We compare the system lift, individual airfoil loading, and surface pressure distributions for a number of biplanes with varying non-dimensional gap, g/c, non-dimensional stagger, s/c , and airfoil thickness, t/c.

2.4.1 Effects of gap and airfoil thickness

First we consider three unstaggered ($s/c = 0$) biplanes, at moderate gaps ($g/c = 0.5$, 0.75, 1) with 25% thick airfoils (NACA 0025), shown in Figure 2.9. The computed system lift coefficients for these are shown in Figure 2.10. Also plotted for comparison is the computed

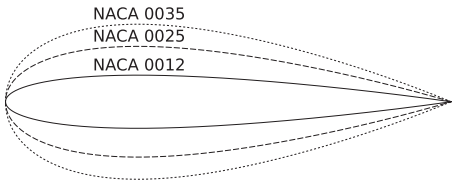

Figure 2.8: Three uncambered 4-digit NACA airfoils of varying thickness.

lift of a single NACA 0025 airfoil. In general, the biplanes have a reduced lift coefficient and lift curve slope compared to the lone NACA 0025 airfoil, due to interference between the two airfoils. The system lift performance (lift curve slope) is shown to increase with increased gap.

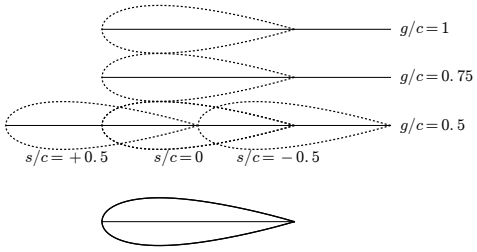

Figure 2.9: Biplane configurations using NACA 0025 airfoils with varying gap and stagger.

The biplane lift parameter, β, defined in Eq. (2.2) is a useful metric to quantify the lift interference in these biplane systems. In general, β, is a function of both the angle of attack and geometry. However, in incompressible, potential flow, the total lift of any airfoil or system of airfoils is of the form $C_l = K \sin(\alpha^*)$, where K is a constant, and in this case it can be seen that the biplane lift parameter, β, is constant.

This constant value of β was computed for a number of biplane configurations with varying gap, stagger, and airfoil thickness. The biplane lift parameter β is plotted for unstaggered biplanes with NACA 0012, NACA 0025, and NACA 0035 airfoils in Figure 2.11, along with the exact relationship for β given by Munk for the case of thin airfoils. In agreement with the thin airfoil results of lumped vortex methods and the results of Munk, the biplanes with thick airfoils demonstrate a trend towards increased β as g/c increases –

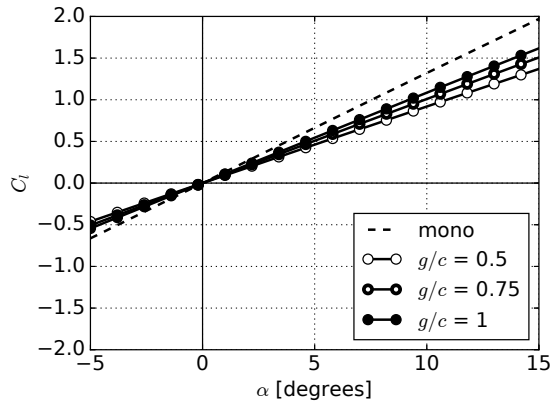

Figure 2.10: System lift coefficients for the three biplane configurations with $g/c = 0.5$, 0.75, and 1 are compared. For reference, the lift coefficient of a single NACA 0025 airfoil is shown. These configurations have $\beta = 0.695$, 0.765, and 0.821, respectively.

increased spacing reduces interference between the two airfoils. For a fixed gap, increased airfoil thickness is shown to reduce system lift performance.

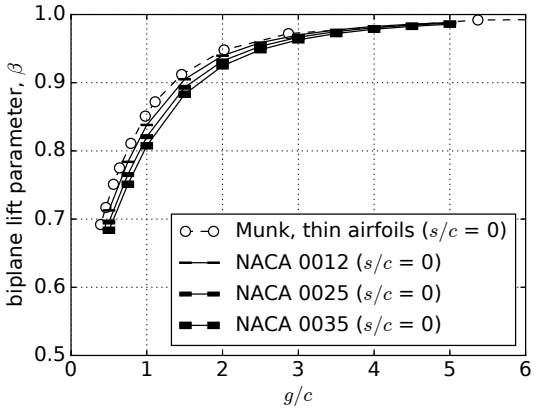

Figure 2.11: Biplane lift parameter β for NACA 0012, 0025, and NACA 0035 biplanes, computed from panel method results. Increased thickness increases interference between the airfoils, reducing β.

2.4.2 Effects of stagger and airfoil thickness

The effect of stagger was assessed by computing the lift performance of biplanes with NACA 0025 airfoils at a fixed gap ($g/c = 0.5$) and various positive staggers ($s/c = 0.25, 0.5, 0.75$)

(see Figure 2.9). The system lift coefficients for these configurations are plotted in Figure 2.12. Positive stagger is seen to shift the zero lift angle of attack, α_0, to the left, corresponding to an *effective camber* for the airfoil system. This is not to be confused with the "induced camber" described in [59], which describes the virtual camber on each individual airfoil induced by the circulation of the other. The effective system camber demonstrated here is unique to biplanes with thick airfoils and cannot be predicted by thin airfoil theories for biplanes; at $\alpha = 0$ (and with $d = 0$), these thin airfoil theories predict zero lift and circulation. Increased stagger is also shown to slightly increase the lift curve slope.

The zero lift angles of attack for biplanes with the fixed gap ($g/c = 0.5$) and various airfoil thicknesses (NACA 0012, NACA 0025, NACA 0035) are plotted against stagger in Figure 2.13; this gap is chosen since the induced camber effects are most pronounced with smaller gap. The zero lift angles of attack (and thus the strengths of the induced camber) are shown to increase with positive stagger up to a certain stagger magnitude – for the tested configurations, around $|s/c| = 0.75$ – above which the magnitude of the system effective camber decreases. Negative stagger results in a negative effective camber which is symmetric in magnitude about $s/c = 0$. Increased airfoil thickness is shown to increase the magnitude of the effective camber, supporting the idea that the effective camber is a result of airfoil thickness.

The constant values of β are computed for the staggered configurations, and are plotted in Figure 2.14. As was also predicted by the lumped vortex method, β is shown to increase symmetrically with positive or negative stagger, indicating that the lift interference is reduced when stagger is increased or decreased. Similarly to the cases plotted in Figure 2.11, increasing airfoil thickness reduces β.

2.4.3 Individual airfoil loads

The previous section examined the trends in the total system lift coefficients with varying gap, stagger, and airfoil thickness. However, of equal interest to the overall lift performance are the forces on the individual airfoils, which are important to the structural design of

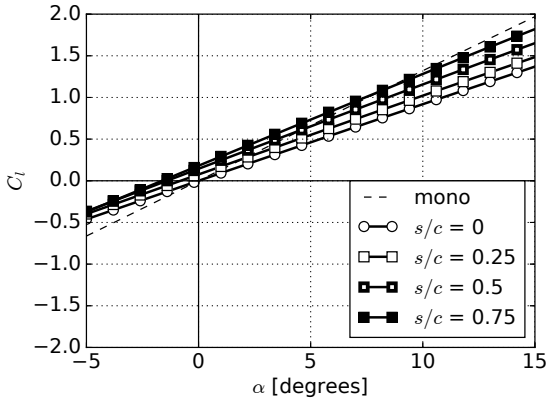

Figure 2.12: System lift coefficients for the three biplane configurations with a fixed gap g/c = 0.5 and varying stagger (s/c = 0, 0.25, 0.5, 0.75). For reference, the lift coefficient of a single NACA 0025 airfoils is shown.

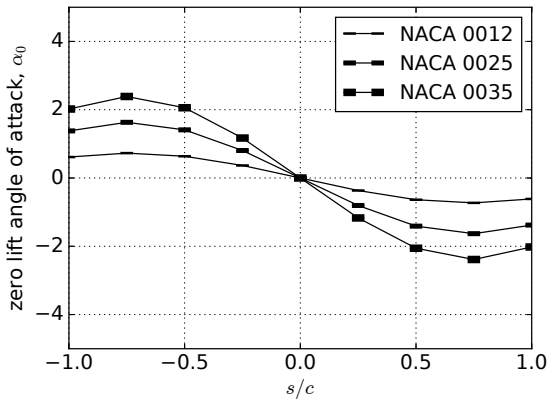

Figure 2.13: System zero-lift angle of attack, α_0, for biplane configurations with a fixed gap ($g/c = 0.5$) and varying stagger and airfoil thickness

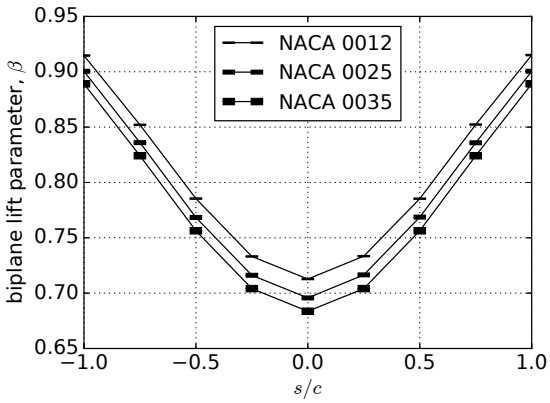

Figure 2.14: Biplane lift parameter, β, for the biplane configurations with a fixed gap ($g/c = 0.5$) and varying stagger and airfoil thickness.

biplane airfoil and wing systems. In this section, we compute these forces through integration of the surface pressures for biplanes with NACA 0025 airfoils and varying gap and stagger.

The lift coefficients, with the forces on each airfoil decomposed, are plotted for biplanes with NACA 0025 airfoils, no stagger ($s/c = 0$), and varying gap ($g/c = 0.5, 0.75, 1$) in Figure 2.15, and for fixed gap ($g/c = 0.5$), and varying positive/negative stagger ($s/c = \pm 0.25, \pm 0.5, \pm 0.75$) in Figures 2.16 and 2.17 respectively. For all decomposed lift polars, the airfoils experience unequal loading throughout the computed angle of attack range. At the system zero lift angle of attack, α_0, the upper airfoil experiences *negative* lift, while the lower airfoil experiences an equal positive lift. This result disagrees with the thin airfoil results of Munk and the result of the lumped vortex method (Eq. (2.9)), which show that in unstaggered biplanes with thin airfoils, both airfoils should experience zero lift at α_0. Thin airfoil analyses also predict increased lift on the upper and reduced lift on the lower airfoils due to the repulsive force; however for these biplanes with thick airfoils we see that the lower airfoil has considerably higher lift forces.

2.4.3.1 The attractive force

The contradiction between the results for biplanes with thick and thin airfoils is due to the increased velocity of fluid in the *channel* between the two airfoils of a biplane with thick

airfoils; we refer to this as the *channel acceleration*. Figures 2.19 and 2.20 show that fluid in the channel experiences an increased velocity compared to the case where the airfoil flies individually. The increased velocity in the channel is accompanied by a pressure drop along the adjacent airfoil surfaces, giving rise to a net attractive force between the two airfoils which affects the loads experienced by each airfoil. A similar effect was observed in [64] for the case of stacked lifting cylinders. It can be seen that the peak velocity and thus strength of the channel acceleration increases at smaller gaps. Stagger, positive or negative, is shown to decrease the strength of the channel acceleration, since the gap between the airfoils is larger in these cases.

For the biplanes with thick airfoils here, the attractive force is seen to significantly affect the individual airfoil loading. In the $g/c = 0.5$, $s/c = 0$ case shown in Figure 2.15a, at $\alpha = 0$ the attractive force leads to a lift coefficient on the upper airfoil of approximately -1, and a lift coefficient of 1 on the lower airfoil. Mirroring the trends in the centerline velocity, the strength of the attractive force decreases as the gap is reduced. As can be seen in Figure 2.15b, (again considering $\alpha = 0$) when g/c is increased to 0.75, the upper and lower airfoils experiences a lift coefficient of approximately ± 0.4. When $g/c = 1$ (Figure 2.15c), the lift coefficient is approximately ± 0.2. This effect also persists to higher angles of attack; for the $g/c = 0.5$ case, the lift on the upper airfoil remains negative until $\alpha \approx 9$ degrees.

Stagger is shown to affect the attractive force between airfoils. As shown in Figures 2.16 and 2.17, positive and negative stagger both lead to more equal loading on both airfoils. This happens for a number of reasons. First, as was shown in Figure 2.20, stagger reduces the strength of the channel acceleration and thus the attractive force. Secondly, because the airfoils are staggered, the attractive force acts along a vector which is misaligned from the lift vector, contributing to a force in both the lift and drag directions. It should be noted that the effect of stagger will depend on the specific profiles of the upper and lower airfoils.

The drag forces on the individual airfoils are plotted in Figure 2.18. For the unstaggered cases at positive angles of attack shown in Figure 2.18a, it can be seen that the upper airfoil experiences a negative drag force, while the lower airfoil experiences a positive drag force. This again contradicts the results of thin airfoil analyses, which predict the opposite – positive

drag on the upper and negative drag on the lower – as a result of the repulsion between airfoils. As for the lift forces discussed above, this is a result of the channel acceleration and attractive force. The magnitude of the drag force coefficient for the small gap case $g/c = 0.5$ is approximately 0.2; this decreases quickly as the gap is increased. Figure 2.18b shows the variation in drag coefficient with stagger. Positive stagger, which shifts the upper airfoil forward, results in a positive drag on the upper airfoil and negative on the lower airfoil, since the attractive force between airfoils is more closely aligned with the drag vector. The opposite is true for negative stagger. For all all cases, the drag forces acting on the two airfoils are equal and opposite so that their sums are zero, in accordance with D'Alembert's paradox.

The attractive force is shown to have a strong influence on the loading of individual airfoils in a biplane configuration. This force contributes significantly to the lift and drag loads on the airfoils, resulting in loading trends that differ from those predicted by biplane thin airfoil analyses. The effects of the attractive force are likely to be important in the structural design of biplane wings or airfoil systems with thick airfoils.

2.4.3.2 The repulsive force

For biplanes with thin airfoils, both exact and approximate solutions showed the existence of a repulsive force due to the same-signed circulation of the airfoils; the same repulsive force exists when the airfoils have thickness. The lumped vortex model showed that the contribution of the repulsive force to the lift coefficient grows with angle of attack approximately as α^2, and decreases with the gap to chord (as $c\zeta^2/g$). This repulsive force was shown to increase the lift experienced by the upper airfoil and reduce the lift experienced by the lower airfoil; it can also be seen that the repulsive force increases the lift curve slope of the upper airfoil and decreases the lift curve slope of the lower airfoil as α is increased.

The decomposed lift coefficients for the computed biplane configurations all show these trends – the lift curve slope of the upper airfoil is increased with α, and that of the lower is decreased, an effect of the repulsive force which grows in α. The repulsive force due

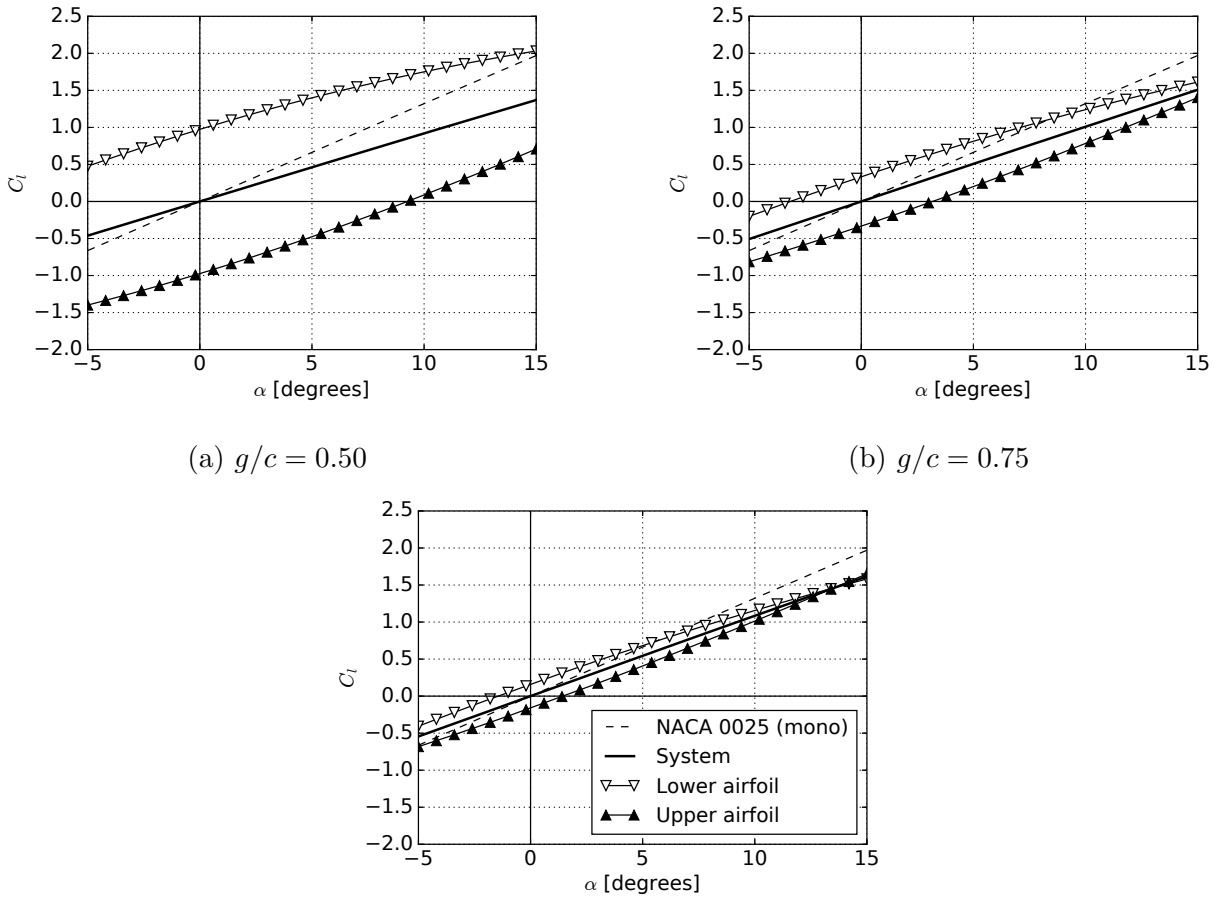

(a) $g/c = 0.50$

(b) $g/c = 0.75$

(c) $g/c = 1.00$

Figure 2.15: Lift coefficients for unstaggered ($s/c = 0$) biplanes with NACA 0025 airfoils and varying gap to chord ratios, g/c.

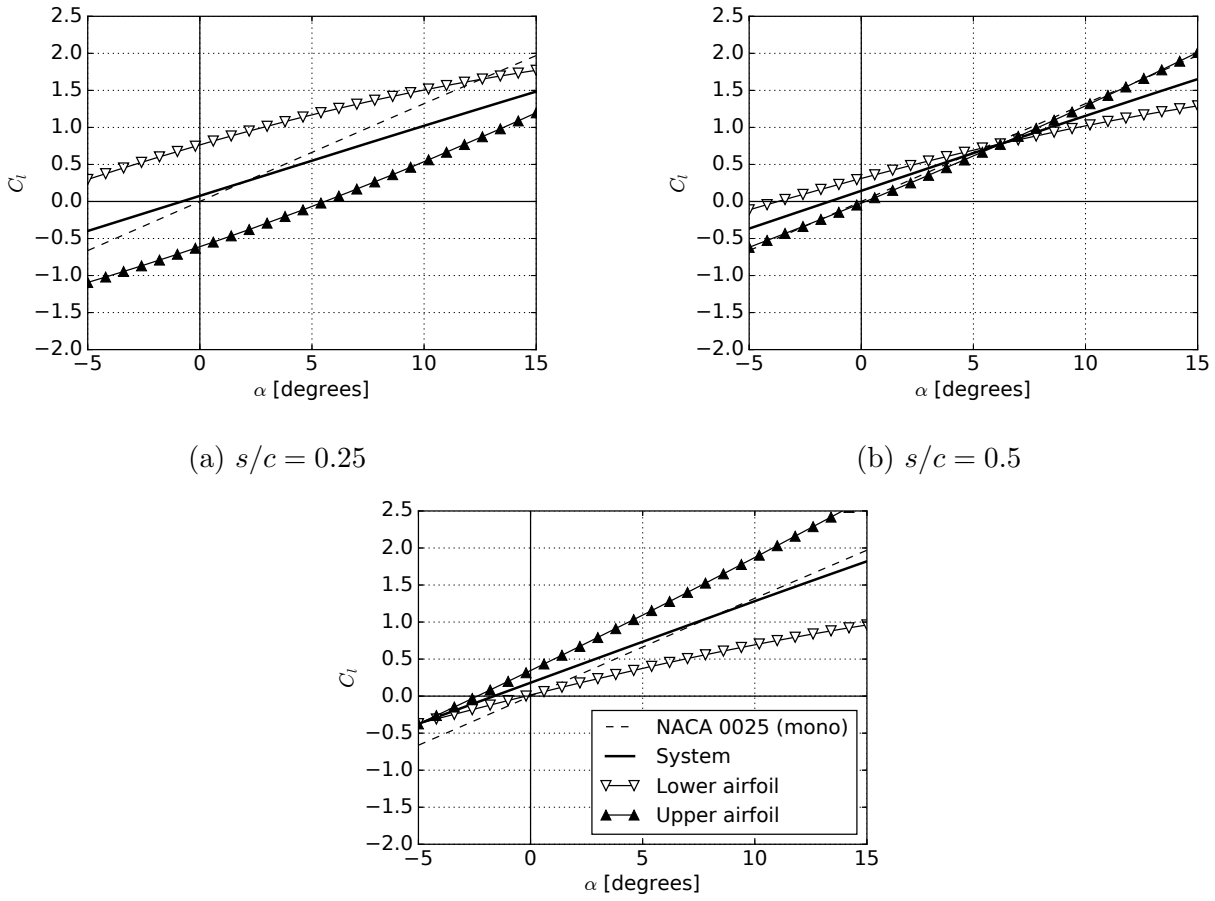

(a) $s/c = 0.25$

(b) $s/c = 0.5$

(c) $s/c = 0.75$

Figure 2.16: Lift coefficients for biplanes with NACA 0025 airfoils, fixed gap ($g/c = 0.5$), and varying positive stagger.

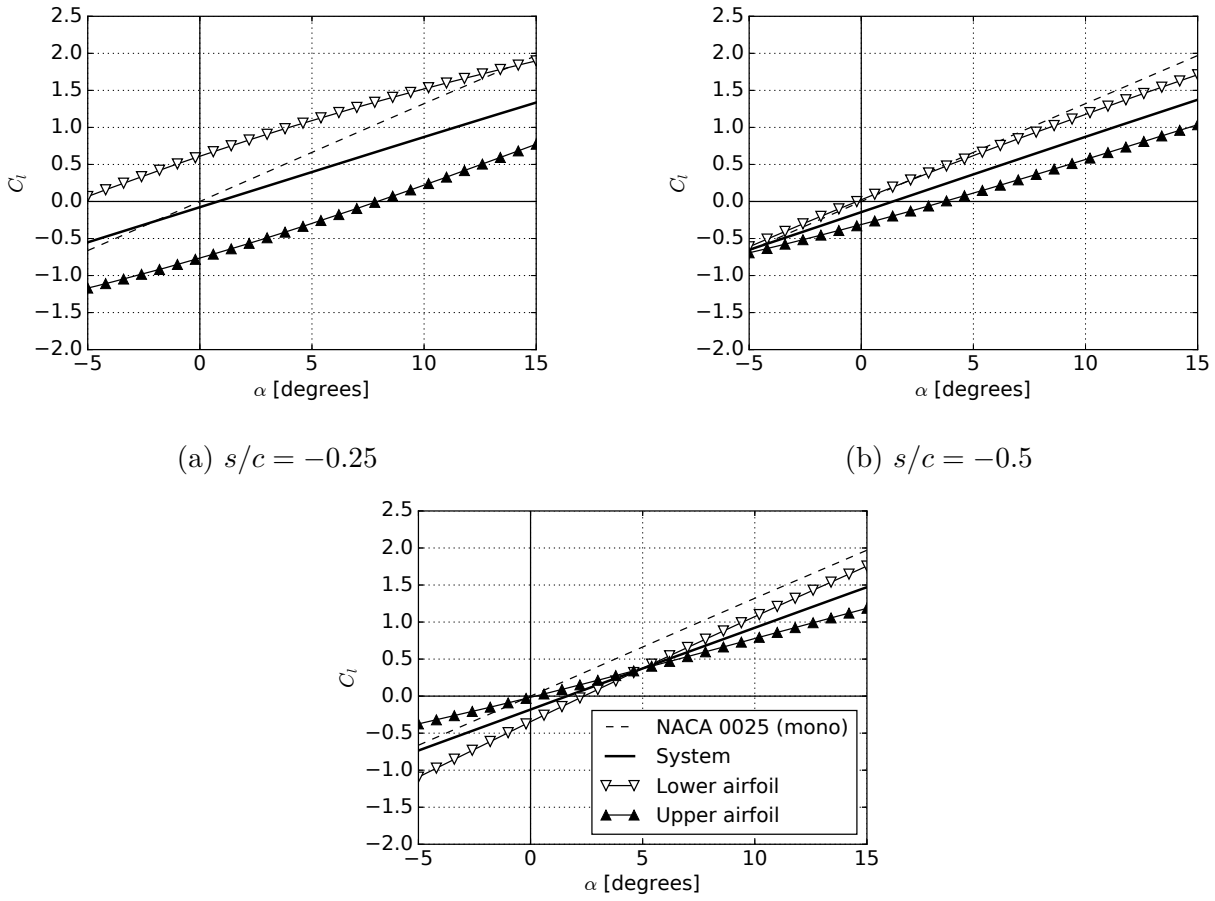

(a) $s/c = -0.25$

(b) $s/c = -0.5$

(c) $s/c = -0.75$

Figure 2.17: Lift coefficients for biplanes with NACA 0025 airfoils, fixed gap $g/c = 0.5$, and varying negative stagger.

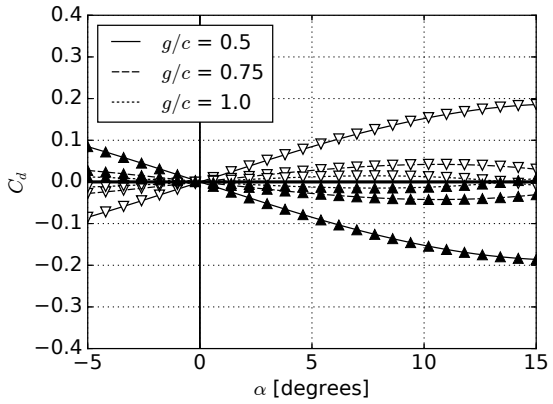

(a) Unstaggered ($s/c = 0$) biplanes with varying gap.

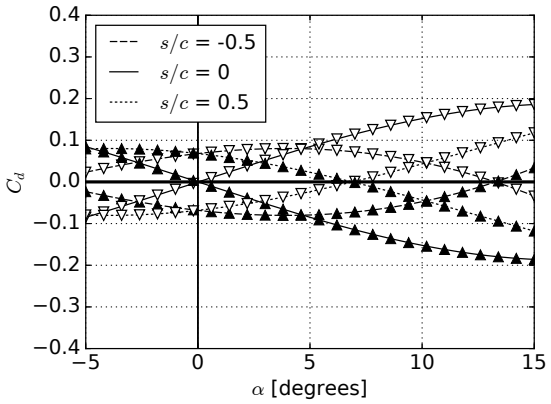

(b) Biplanes with fixed gap ($g/c = 0.5$) and varying stagger.

Figure 2.18: Computed drag coefficient, C_d, for biplanes with NACA 0025 airfoils with varing gap and stagger, decomposed into contributions of upper airfoil (upward triangle) lower airfoil (downward triangle). The total system drag is nominally zero for all cases.

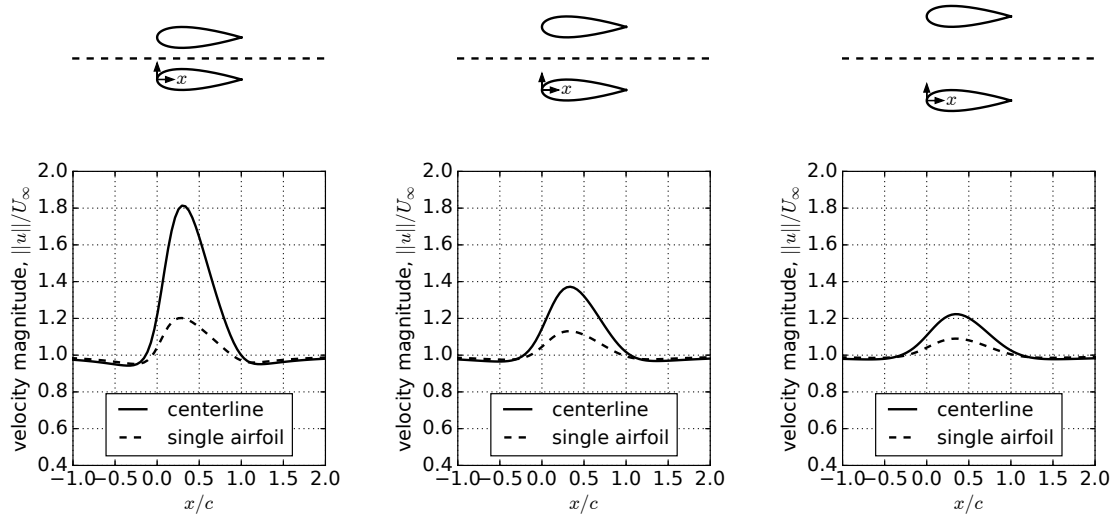

(a) $g/c = 0.5$ (b) $g/c = 0.75$ (c) $g/c = 1$

Figure 2.19: Centerline velocity magnitude at $\alpha = 0$ for unstaggered biplanes ($s/c = 0$) using NACA 0025 airfoils with varying g/c. Dashed lines show the velocity magnitudes at the same distances away ($g/2c$) from a single NACA 0025 airfoil.

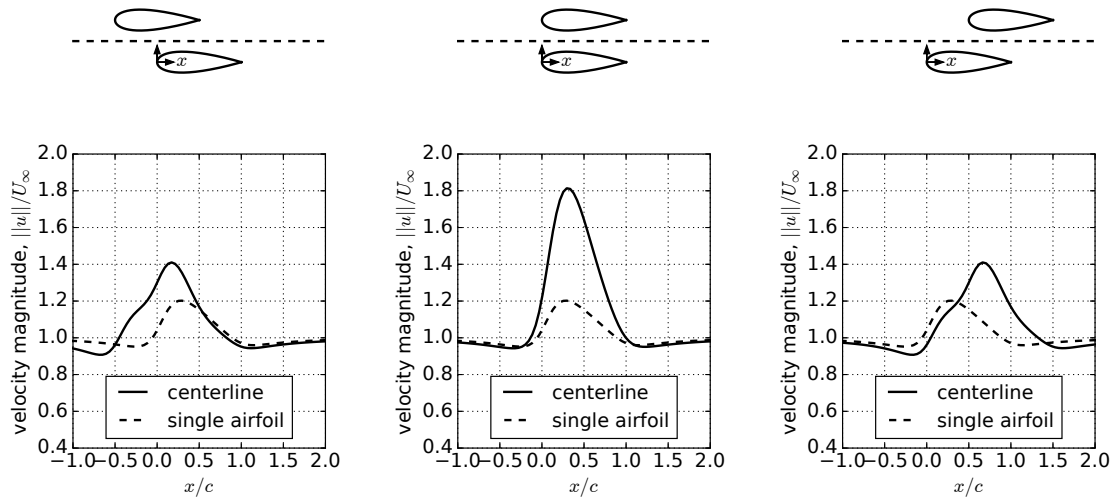

(a) $s/c = 0.5$ (b) $s/c = 0$ (c) $s/c = -0.5$

Figure 2.20: Centerline velocity magnitude at $\alpha = 0$ for biplanes using NACA 0025 airfoils with fixed gap ($g/c = 0.5$) and varying s/c. Dashed lines show the velocity magnitudes at the same distances away ($g/2c$) from a single NACA 0025 airfoil.

to airfoil circulation acts directly opposite to the attractive force due to airfoil thickness discussed previously, contributing to both lift and drag. The net forces on the upper and lower airfoils are affected by the relative strengths of the attractive forces, which increase lift on the lower airfoil and reduce it on the upper, and the repulsive force, which do the opposite. The repulsive forces also contribute to drag. The decomposed lift plots for the unstaggered biplane in Figure 2.15 show that the lower airfoil produces more lift for most of the plotted α range, indicating that the effects of attractive forces dominate over the the repulsive ones for biplanes with thick airfoils spaced closely.

2.4.4 Effect of channel acceleration on surface pressure distributions

The surface pressure distributions reveal phenomena that cannot be seen in the integrated lift forces. Computed pressure distributions for NACA 0025 biplane configurations with $g/c = 0.5$ and varying stagger are plotted for a number of angles of attack in Figures 2.21 and 2.22. Also plotted for comparison is the surface pressure distribution of a single NACA 0025 airfoil; this is the pressure distribution that either airfoil in a biplane would experience

if the two airfoils were spaced infinitely far apart.

First, we examine the unstaggered case Figure 2.21. It can be seen that at all angles of attack, the pressure distributions along the *inner* surfaces of the biplanes – the upper surface of the lower airfoil, and the lower surface of the upper airfoil – differ significantly from those of the individually-flying NACA 0025 airfoil as a result of the channel acceleration. The pressures along the *outer* surfaces, however, are only slightly altered by the presence of the other airfoil. At $\alpha = 0$, large suction peaks are observed on both inner surfaces near the location of minimum channel width, which is for these biplanes around $x/c = 0.3$. These suction peaks are due to the channel acceleration, and increase as the gap is decreased. The net suction on the inner surfaces reflects the attractive forces discussed in Section 2.4.3.

As the angle of attack is increased and airfoil circulations develop, the channel velocities are superposed with the circulation flows. The effects of this are most evident for the small gap ($g/c = 0.5$) case shown in Figure 2.21. At $\alpha = 5$ degrees, the suction peak around $x/c = 0.3$ is strongly visible, both on the suction side of the lower airfoil and the pressure side of the upper airfoil. At $\alpha = 10$ degrees, the superposition of this suction peak with the more traditional leading edge suction peak produces an atypical flat-topped pressure distribution on the suction side of the lower airfoil. Generally, as the angle of attack is increased, the surface pressures on both upper and lower airfoils more closely resemble those of the individual airfoil.

The pressure distributions for a case with positive stagger is plotted in Figure 2.22. With stagger, the channel acceleration is reduced, as discussed in Section 2.4.3. In addition, the modification of the surface pressures is limited to the region where the airfoils most closely overlap. The pressures along the outer surfaces are slightly different in magnitude from those of the single NACA 0025 airfoil, although their shapes are still similar. This discrepancy can be attributed to the induced upwash and downwash of the staggered airfoils, which affects each airfoil's local angle of attack and thus their circulations and surface pressures.

The pressure distributions presented here were computed for an inviscid flow. However, the shapes of the pressure distributions can still give some insight into the stall characteristics

of biplanes with thick airfoils in viscous flows. The slopes of the pressure distributions, $\partial C_P/\partial x$, which often dictate the stall behavior of wing systems, are strongly modified by the channel acceleration. Consider again the small gap ($g/c = 0.5$) case at $\alpha = 0$. The channel acceleration leads to a suction peak along both inner airfoil surfaces. As a result of this peak, an increased adverse pressure gradient exists on the inner surfaces in the pressure recovery region. In viscous flows, this could lead to earlier onset of separation compared to the single airfoil. This adverse pressure gradient can be seen to persist at higher angles of attack. Particularly interesting is the fact that a strong adverse pressure gradient exists on the pressure side of the upper airfoil, a surface on which boundary layer separation would typically not be expected

The shapes of the surface pressure distributions for these biplanes with thick airfoils showed considerable diversity and sensitivity to relative airfoil spacing. However, these surface pressure distributions (and similarly, the velocity distributions) are likely to strongly affect boundary layer transition and stall characteristics of the airfoils in biplanes with thick airfoils and should be taken into consideration when designing biplanes with thick airfoils.

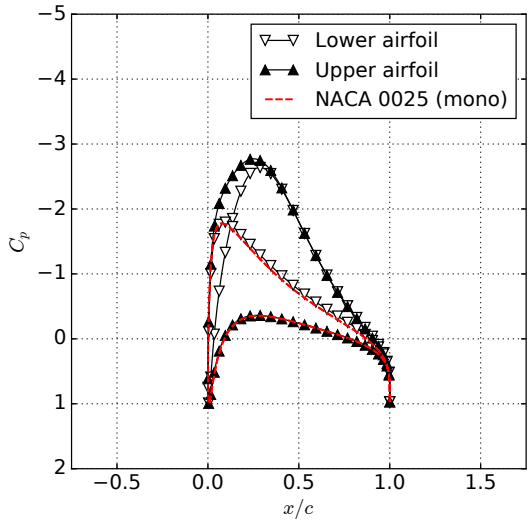

(a) $\alpha = -5$ deg.

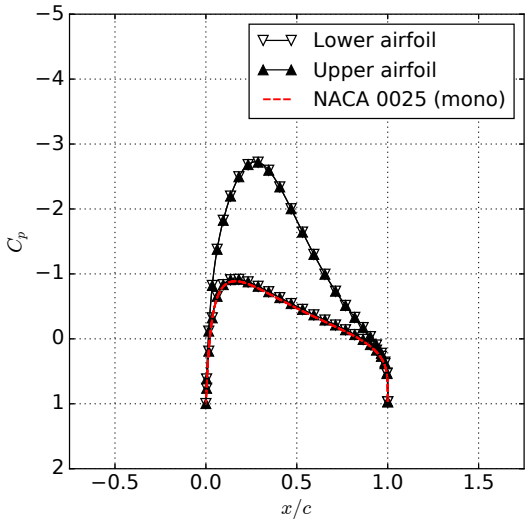

(b) $\alpha = 0$ deg.

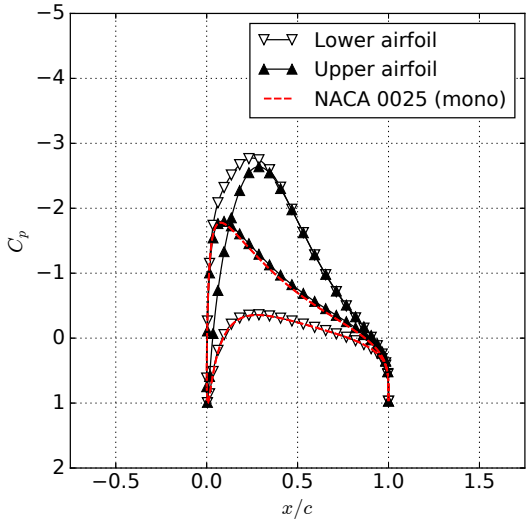

(c) $\alpha = 5$ deg.

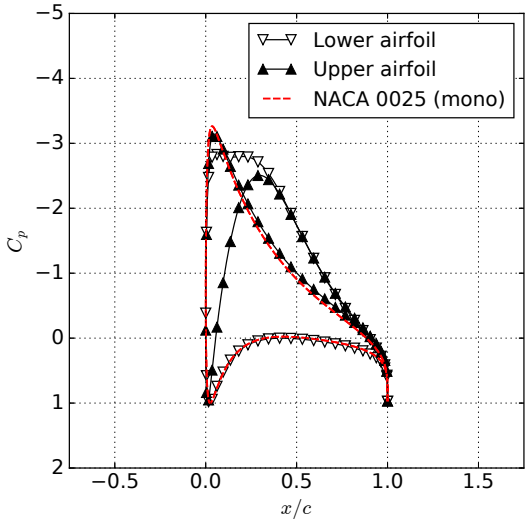

(d) $\alpha = 10$ deg.

Figure 2.21: Surface pressures for NACA 0025 biplanes with $g/c = 0.5$, $s/c = 0$

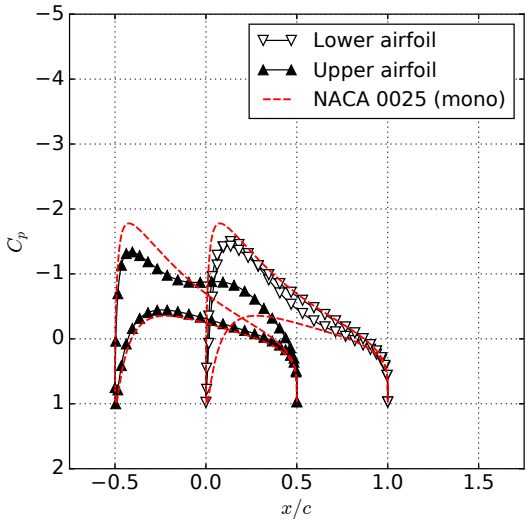

(a) $\alpha = -5$ deg.

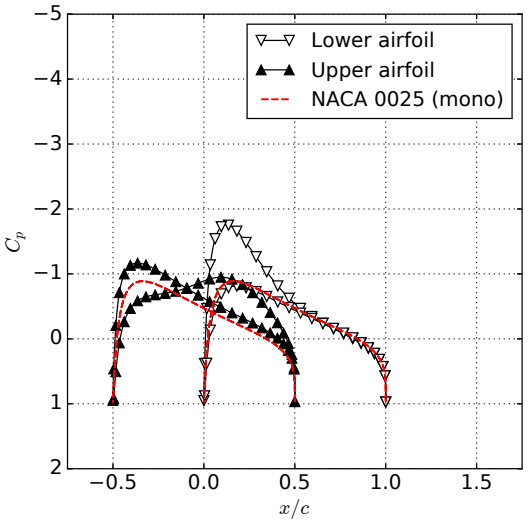

(b) $\alpha = 0$ deg.

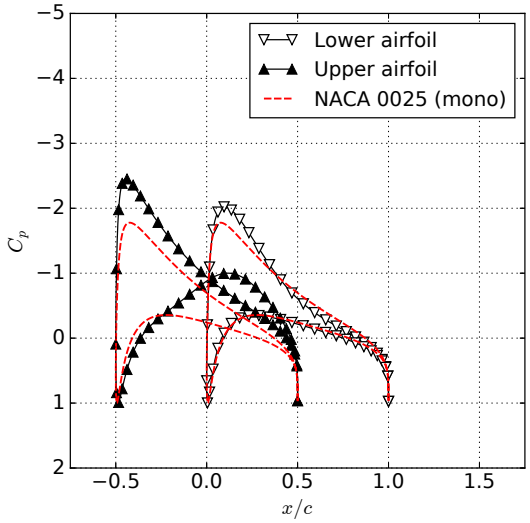

(c) $\alpha = 5$ deg.

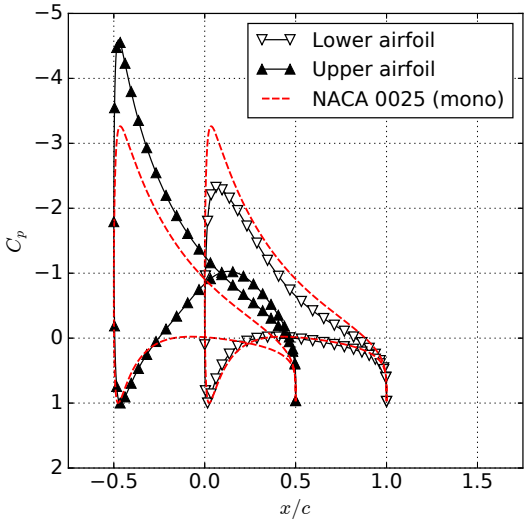

(d) $\alpha = 10$ deg.

Figure 2.22: Surface pressures for NACA 0025 biplanes with $g/c = 1$, $s/c = 0.5$.

2.5 Conclusions

In this work, we sought to qualitatively investigate the aerodynamic phenomena for biplanes with thick airfoils in incompressible potential flow. First, a lumped vortex method was used to demonstrate the qualitative behavior of biplanes with thin airfoils. Then a two-dimensional panel method was used to investigate the incompressible potential flow around such biplanes.

The system lift performance, the forces on the individual airfoils in the biplanes, and the surface pressure distributions were examined for a number of biplane configurations with varying gap, stagger, and airfoil thickness. A new parameter called the lift performance parameter, β, was defined here and was used to quantify the performance of the biplane systems. As was previously known for biplanes with thin airfoils, the system lift performance of biplanes with thick airfoils was shown to improve as the spacing between airfoils, or the gap, was increased. For biplanes with thick airfoils, stagger produced an effective camber which shifted the system lift curve. Increased airfoil thickness was shown to reduce β, and to increase the strength of the effective camber.

The loads on each airfoil were shown to be strongly influenced by an attractive force between the airfoils of the biplane, resulting from the *channel acceleration* – the high speed and low pressure fluid in the channel between the two airfoils – which is significant for biplanes with thick airfoils and at small gaps. The attractive force was shown to affect both lift and drag the airfoils, reducing lift on the upper airfoil and increasing lift on the lower. Similarly, this attractive force produced significant drag forces on the airfoils. Thin airfoil analyses showed the existence of a repulsive force, due to the same-signed circulations about each airfoil, but for the finite-thickness biplanes investigated here, the attractive forces were shown to dominate.

Trends in the surface pressures along the airfoil surfaces were also examined. For unstaggered biplanes, the surface pressures along the outer surfaces of the biplane were shown to be similar to those about a single airfoil of the same profile flying on its own. The surface pressures on the inner surfaces were shown to be significantly modified by the channel ac-

celeration. Biplanes with stagger also experienced similar, but weaker, modifications to the surface pressure. These variations in the shape of the surface pressure distributions are likely to change the separation and stall characteristics of the airfoils, and should be considered when designing biplane airfoil systems intended for operation at high angles of attack in viscous flows.

Overall, airfoil thickness was shown to have a strong affect on the performance of biplane systems, leading to an effective camber, significant attractive force, and modified surface pressure distributions due to channel acceleration, none of which are predicted by analyses for biplanes with thin airfoils.

The effects of viscosity and compressibility were neglected in the present analyses, but the qualitative effects of thickness demonstrated here will exist in real (viscous and compressible) flows around biplane airfoils at high Reynolds numbers and at moderate angles of attack. While more detailed design should consider the viscosity and compressibility effects, the results here may serve as a guide in the preliminary design of biplanes which use thick airfoils.

CHAPTER 3

Aerodynamic design, performance, and loads of biplane wind turbine blades

Biplane blades have been proposed as an enabling concept for larger, lighter horizontal axis wind turbines blades. Past work has shown that these blades have significantly improved structural efficiency in flapwise bending when compared to conventional blade designs. Given such compelling improvements in structural performance, the aerodynamic performance of biplane blades is of considerable interest. In this work, the aerodynamic design of biplane blades is examined, the rotor performance quantified, and the aerodynamic loads evaluated and discussed. Using the NREL 5 MW blade as a reference, two biplane blades are designed to give optimal loading in the biplane region, and the aerodynamic performance of all blades quantified using BEM. The biplane blades are shown to have significantly reduced chord lengths compared to the reference blade, indicating a potential for improved transportability. Results show that the biplane blades can be designed with improved inboard loading compared to conventional blades, leading to small increases ($< 1\%$) in rotor power coefficient. However, these increases are partially offset by efficiency decreases required to maintain a smooth chord distribution, and by the drag of the merging region. The aerodynamic loads, which are strongly related to blade mass and loads on the turbine structure, are also quantified for normal and extreme operating conditions. It is shown that under design-driving extreme wind events, biplane blades are able to reduce thrust and flapwise root bending moment by as much as 11.0% and 6.5% respectively. This indicates a potential to reduce both tower and blade mass in medium- and high- wind sites, including offshore. The aerodynamic performance, in conjunction with the load reductions, reduced chord lengths, and previously demonstrated structural efficiency, indicate that biplane-equipped turbines can

be built lighter than conventional turbines, with equal or better power output.

3.1 Introduction

Recently a number of horizontal axis wind turbine blade concepts that use high lift multi-element airfoils [36] in the near-root region have been proposed. Examples include designs with multi-element airfoils and leading edge slats [66, 22, 20]. A shared goal of these designs is to improve the aerodynamic performance in the inboard by increasing the local aerodynamic loading. The root region of conventional blade designs is typically aerodynamically underloaded (loaded less than is required for optimal power production), since the chord length and thus thrust force are constrained by non-aerodynamic design requirements, e.g., transportation, manufacturing, or material limitations. In addition to having non-optimal loading, conventional blades typically use thick airfoils which have poor aerodynamic efficiency, leading to parasitic drag losses inboard.

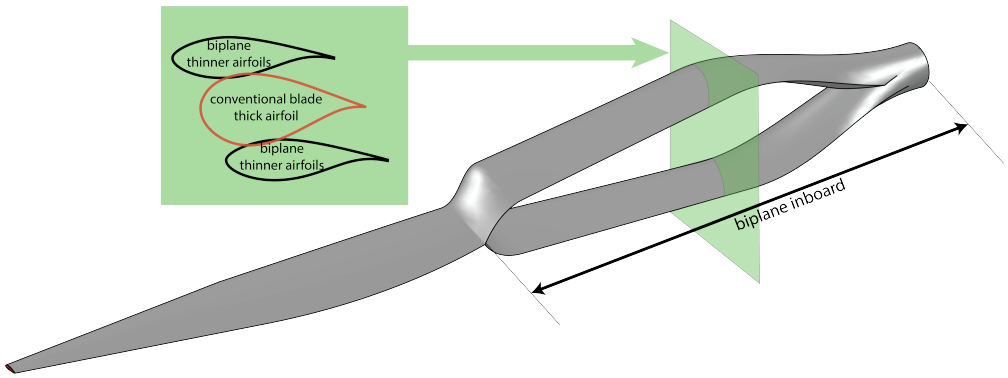

Figure 3.1: Biplane blade concept. A biplane inboard region merges to a monoplane outboard, improving both structural and aerodynamic performance.

The biplane blade (Figure 3.1) is a concept which seeks to address these deficiencies. A biplane inboard merges to a monoplane outboard; in contrast with other lift-augmenting concepts, this design has been shown to have approximately 30% better flapwise structural efficiency (flapwise stiffness per unit mass) compared to conventional blade designs [45, 42]. This increased structural efficiency indicates that a biplane blade could be built lighter (for the same tip deflection and length), or longer (for the same tip deflection and mass) than conventional blades. Biplane airfoils also have higher lift coefficients and aerodynamic efficiency compared to the thick airfoils traditionally used inboard. The high-lift biplanes can

be used to improve loading and power output in the inboard region, while the aerodynamic efficiency can lead to reduced parasitic drag losses compared to traditional blade designs.

In light of the demonstrated structural benefits of the biplane blade, it is important to assess the aerodynamic performance and design considerations of biplane wind turbine blades. The basic aerodynamic benefits of biplane airfoils were quantified by Roth-Johnson and Wirz [45], who showed increased max lift and aerodynamic efficiency for biplane airfoils when compared to a thick inboard monoplane airfoil. However, the aerodynamic design and performance of biplane blades have to date only been examined at a cursory level. The improvements in inboard loading and power production enabled by using high lift biplane airfoils were discussed in [41], but not quantified. With regards to aerodynamics, that work focused on the optimization of biplane airfoil profiles for maximum lift and aerodynamic efficiency. In an earlier effort [46], the planform design (chord, twist, airfoil distributions) for a biplane blade was examined in more detail. That work discussed the planform design process and quantified the *design point* performance of biplane blades. It was shown that when applying a traditional design approach which sought to achieve constant loading and efficient aerodynamic operation along the blade span, the discontinuous lift performance of the airfoils at the merge from biplane to monoplane led to discontinuous chord distributions. Instead, a prescribed chord approach was used to design a number of optimally-loaded biplane blades with more realistic chord distributions. The design point performance (C_P) of these blades were compared to an aerodynamically ideal but structurally unrealistic "fantasy" monoplane blade which used an 18% thick airfoil along its entire blade span.

While design point performance is closely correlated to a rotor's AEP, it is only one consideration in the design of wind turbine blades. Wind turbines do not always operate at their design point due to unsteady winds, limitations of downstream components, or physical system/controller response times. Therefore, the aerodynamic performance at off-design conditions is also important. Aerodynamic loads under design point and off-design conditions are also of critical importance as these loads drive the structural design of the blades and thus blade mass, and also have an impact on the loads for downstream components.

In an effort to provide a better understanding of the aerodynamics of biplane wind tur-

bine blades, the objectives of this work are to design biplane turbine blades, assess their performance (design point and off-design), and quantify their aerodynamic loads. Two biplane blades, both based on the NREL 5 MW blade [1], are designed to have optimal loading using BEM theory. The aerodynamic performance and loads of these blades are compared to those of the NREL 5 MW monoplane blade. In addition to improved design point performance and off-design performance, the biplane blades are shown to have reduced design-driving aerodynamic loads, and reduced chord lengths inboard. These conclusions, in concert with previously demonstrated structural benefits, show the potential for cost of energy reductions using biplane blades.

3.2 Biplane design candidates

In this work the aerodynamic performance and characteristics of two biplane blades with different prescribed chord distributions is investigated. This section describes the approach used to design the biplane blades.

3.2.1 Design approach – optimal loading with prescribed chord distribution

The blades here are designed using simplified BEM equations. Neglecting tip/root losses, airfoil drag and its effect on the wake, and the effect of wake rotation on pressure, BEM theory predicts that the maximum blade power coefficient is achieved when the axial induction factor, a, is constant and equal to 1/3 across the span of the blade. A relationship governing the local blade geometry required to give this axial induction, or loading, distribution is given by Burton [67] as:

$$\frac{B}{2\pi}\frac{c}{R}\lambda C_l = \frac{8/9}{\sqrt{\left[1-\frac{1}{3}\right]^2 + \lambda^2 \left(r/R\right)^2 \left[1+\frac{2}{9\lambda^2 (r/R)^2}\right]^2}} \tag{3.1}$$

The local inflow angle, ϕ, corresponding to this loading condition is given by:

$$\tan\phi = \left[\frac{1-\frac{1}{3}}{\lambda\,(r/R)\left[1+\frac{2}{9\lambda^2(r/R)^2}\right]}\right] \tag{3.2}$$

When the blade radius, R, rotor tip speed ratio, λ, and number of blades, B, are fixed, the product of the local chord, c, and the lift coefficient, C_l, must be equal to some function value which varies smoothly with the non-dimensionalized radial location, r/R. From these equations, it is straightforward to design a conventional blade for power-maximizing loading at some design operating condition, defined by the tip speed ratio, λ_{design}.

While drag is neglected in the derivation of the blade geometry equation (its effect on the wake is small), it cannot be ignored in computing the rotor performance. Thus, a common approach to maximizing the rotor power coefficient, C_P, is to design the blade such that that all airfoil sections operate at the angle of attack which maximizes C_l/C_d; this minimizes the drag losses of each section. The lift coefficient at which C_l/C_d is maximized is known as $C_{l,\text{design}}$ and occurs at an angle of attack α_{design}. Substituting $C_{l,\text{design}}$ into Eq. (3.1), one can solve for the chord distribution, $c(r)$, which gives $a = 1/3$ along the blade. Then using Eq. (3.2) and noting the relationship $\phi = \alpha + \beta$, the twist distribution, $\beta(r)$, can be solved for. This simple method is used by a number of authors [67, 21] to design aerodynamically optimal turbine blades.

It was shown in [46], however, that using the above method to design a biplane blade for both optimal loading and maximum L/D operation along its blade span produces unrealistic and non-continuous chord distributions. Instead, a prescribed chord approach is used, in which the chord distribution, $c(r)$, is specified, and the required C_l distribution is computed from Eq. (3.1). Knowing the relationship between C_l and α, the twist distribution can again be computed from Eq. (3.2). Blades designed using this process do not operate at maximum L/D along their entire spans, and are in that sense aerodynamically non-optimal.

3.2.2 Aerodynamic design details

The prescribed chord approach is used to design two biplane blades with different chord distributions. The distributions are continuous (C^0) to facilitate manufacturing and smoothness of the blade profile.

The NREL offshore 5 MW wind turbine [1] serves as a "parent" for the biplane blade designs. The biplane blades are designed by replacing the inboard section – $(r/R)_{\text{root}} \leq r/R \leq (r/R)_{\text{joint}}$ – of the NREL 5 MW blade with biplane airfoils, a prescribed chord twist distribution, and an appropriate twist distribution required to achieve constant $a = 1/3$ loading. For the biplane blades considered here, $(r/R)_{\text{root}}$ is 0.15, and $(r/R)_{\text{joint}}$ is 0.5. From 0 to $0.15R$, the NREL blade is not modified; in this region, the airfoil shapes must transition from the cylindrical root, and are likely to be non-lifting or low-lifting transition airfoils which contribute little to the aerodynamic performance of the rotor. Outboard of $0.5R$, the chord, twist, and airfoil distribution of the NREL blade are used without modification. The joint location halfway along the blade was shown in previous studies to provide good flapwise stiffness while minimizing bending moments in the biplane branches of the blade [42].

A single biplane airfoil configuration is used for the entire biplane region of the blade. The airfoil section, shown in Figure 3.3, is comprised of two identical DU 91-W2-250 (DU 25) airfoils[31], each with a thickness-to-chord ratio of $t/c = 0.25$ and separated by a gap of 1 chord, 0 stagger, and 0 decalage. A gap of 1 chord was chosen, as further increases in gap were shown to give diminishing returns in both aerodynamic performance (lift, drag, efficiency) and flapwise stiffness. The aerodynamic representation of these blades is shown in Figure 3.2.

The lift and drag data for the DU 25 biplane were computed using the MSES [68] solver at Re = 3 million and Ma = 0.22; the polars are shown in Figure 3.4. For details on this analysis, see Appendix A. Note that the force coefficients for the biplane airfoil are non-dimensionalized using a length scale of one chord length, c, as opposed to the total chord length as is occasionally done in biplane aircraft literature – this is the non-dimensionalization that is more relevant to wind turbine blade design. The computed polars are extrapolated

to ± 180 degrees using the method of Viterna [69], where the maximum drag coefficient has been set to match the value of the DU 25 airfoil. It should be noted that this extrapolation method was developed for single airfoils, yet is applied to biplane airfoils here. It is likely that this approximation is invalid across a large range of angles of attack, but should be reasonably accurate for the high angles of attack considered in Section 3.4.3. The biplane airfoil configuration has considerably higher max lift (increased lift curve slope and max lift) compared to the conventional airfoils it replaces. Drag is increased; the peak lift to drag ratio is better than the DU 30 and DU 40 airfoils but worse than the thinner DU airfoils.

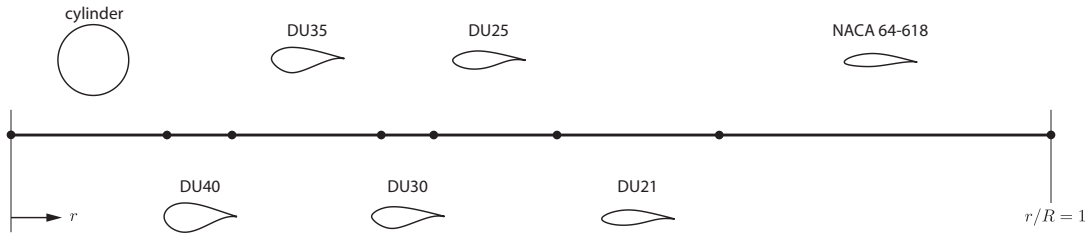

(a) NREL 5 MW blade

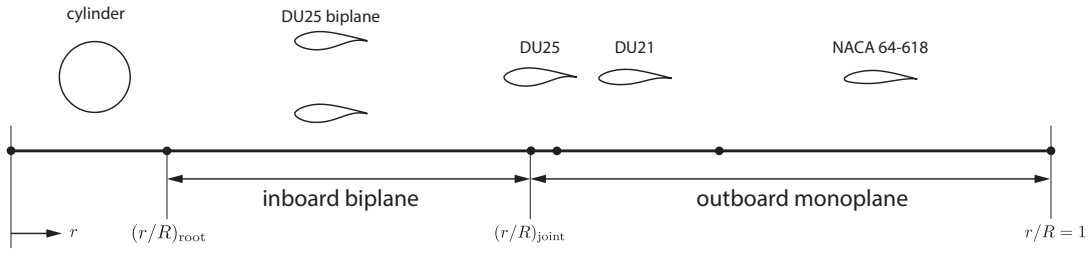

(b) Biplane blades

Figure 3.2: Aerodynamic representations of the baseline monoplane blade (NREL 5 MW) and biplane blades. The biplane blades are created by substituting the inboard region – $(r/R)_{\text{root}} \leq r/R \leq (r/R)_{\text{joint}}$ – of the NREL 5 MW blade with a blade section using a DU25 biplane airfoil, and an appropriate chord and twist distribution. For the blades considered here, $(r/R)_{\text{root}} = 0.15$ and $(r/R)_{\text{joint}} = 0.5$.

In order to investigate the influence of chord distribution, two blades with different chord distributions are designed. Using Equations (3.1) and (3.2), the twist distributions are chosen to give optimal loading along the entire blade span at the design operating condition of the

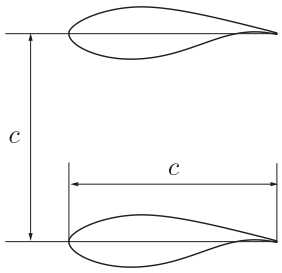

Figure 3.3: Profile of DU 91-W2-250 biplane.

Table 3.1: Properties and design (rated) operating conditions for the NREL offshore 5 MW baseline wind turbine [1].

Power Rating	5 MW
Configuration	Upwind, 3 Blades
Rotor Diameter	126 m
Rated Wind speed, U_∞	11.4 m s^{-1}
Rated Rotation Rate, Ω	12.1 rpm
Rated Tip Speed Ratio, λ	7.55

NREL blade (Table 3.1). The prescribed chord distributions for the two biplane blades studied here are described below.

- The LC biplane blade uses a linear chord in the biplane region. The chord is linear between $r/R = 0.15$ and the joint location at $r/R = 0.5$, and is coincident with the chord distribution of the NREL blade at both locations.

- The CC biplane blade uses a constant chord in the biplane region, and is coincident with the chord distribution of the NREL blade at $r/R = 0.5$

From the discussion in the previous section, it can be understood that these blades are all aerodynamically compromised in some sense. While they do achieve optimal loading, due to the constraint of a continuous chord distribution, a biplane blade cannot be designed which operates the design angle of attack along its entire span. Therefore, both biplane blade candidates discussed above have "sub-optimal" power coefficients.

The chord distributions are shown in Figure 3.5a, along with their corresponding twist distributions, $\beta(r)$, in Figure 3.5b Also shown in Figure 3.5 are the chord and twist dis-

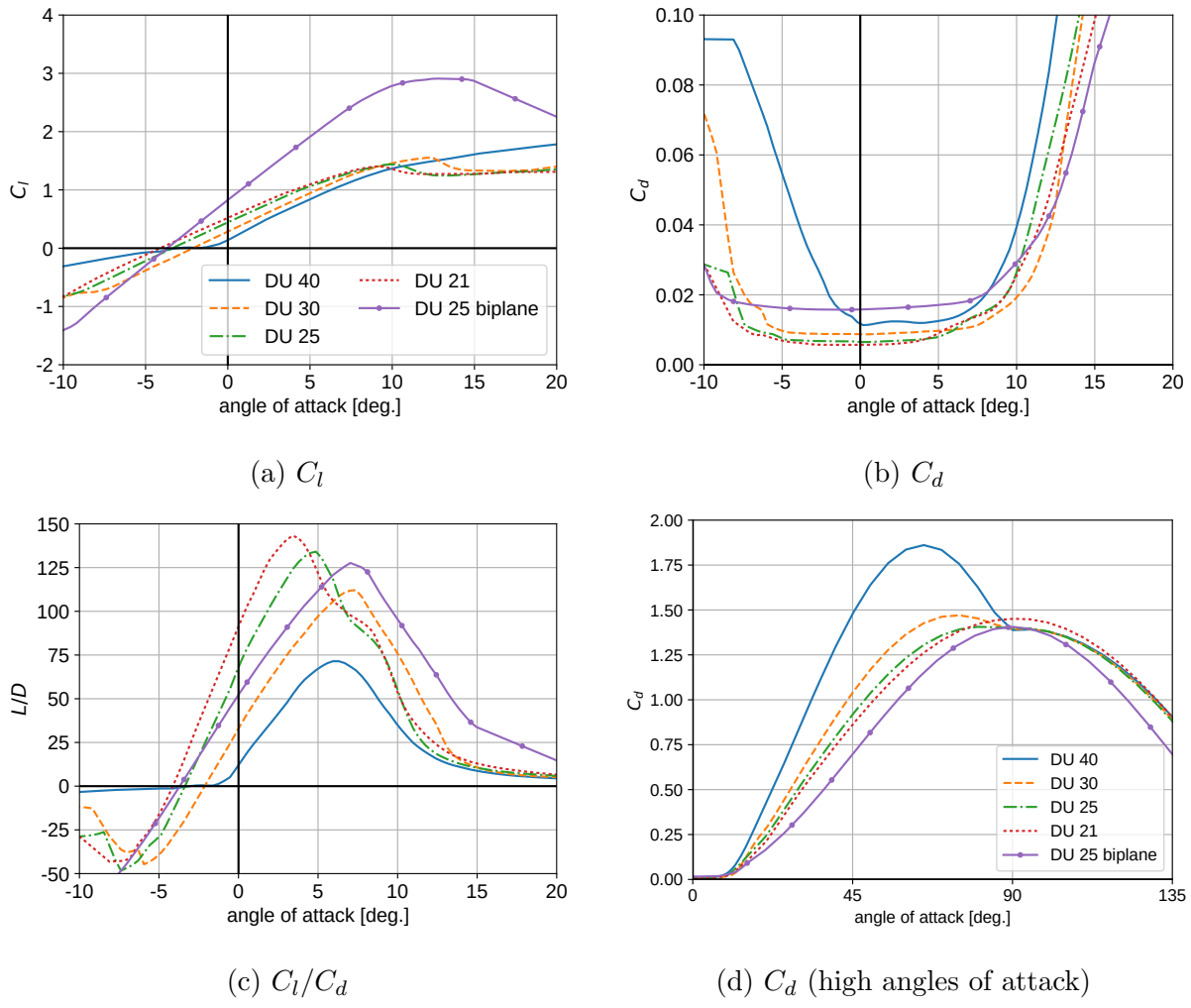

(a) C_l

(b) C_d

(c) C_l/C_d

(d) C_d (high angles of attack)

Figure 3.4: Lift coefficient, drag coefficient, and aerodynamic efficiency for the various airfoils used. The DU 25 biplane airfoil data is computed using MSES at Re = 3 million and Ma = 0.22. All other airfoil data are taken directly from the NREL 5 MW reference paper [1], and are derived from wind tunnel tests. For the airfoils used in the NREL 5 MW blade, lift and drag data are are corrected for 3-D rotational effects using the methods of [70] and [71], respectively.

tributions of the NREL 5 MW blade. Compared to the NREL 5 MW blade, the biplane blades have significantly reduced chord lengths; this arises from the high lift of the biplane airfoils. This chord reduction has positive impacts on extreme loads (further discussed in Section 3.4), and on transportability – biplane blades may be able to circumvent transport constraints which currently limit the size of land-based turbines [72].

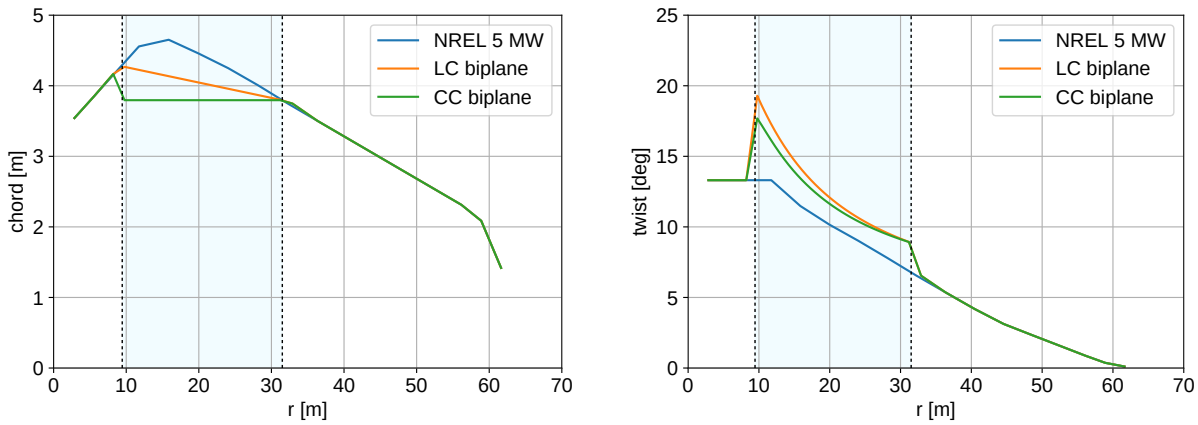

(a) Chord distribution, $c(r)$

(b) Twist distribution, $\beta(r)$

Figure 3.5: Chord, c, and twist, β, distributions for the five blades considered in this study. All blades are designed to achieve $a = 1/3$ along their entire span at $\lambda = 7.55$.

3.3 Results - rotor aerodynamic characteristics

The aerodynamic performance of the NREL 5 MW monoplane, LC biplane, and CC biplane blades were solved numerically using NREL's *WT Perf* BEM code [73]. Loads were computed at their design tip speed ratio of $\lambda = 7.55$. To simplify analysis, the rotor was untilted and unyawed, and the inflow was uniform and steady.

3.3.1 Rotor performance

The design point rotor coefficients are shown in Table 3.2. Both LC and CC biplane blades have an approximate 0.85% increase over the monoplane blade. The thrust coefficients for the LC and CC blades are increased by about 3.63%. Note that at the design operating condition, the power and thrust coefficients for the CC and LC biplane blades are nearly identical (within 0.05% of each other).

The rotor power coefficients are plotted as a function of tip speed ratio (often referred to as the $C_P - \lambda$ curves) in Figure 3.6a. As was seen in Table 3.2, the peak C_P for both biplanes is marginally increased over that of the baseline blade. The shape of the C_P curve is different for the biplane blades, with a broader peak towards the low tip speed ratios. The small increase in C_P seen at the design point is maintained at higher tip speed ratios. At

Table 3.2: Computed power and thrust coefficients at design point ($\lambda = 7.55$, zero pitch). Percent difference in parentheses shows relative difference with respect to the NREL 5 MW baseline blade.

blade	C_P	C_T
NREL 5 MW monoplane	0.4928 (0.00%)	0.7953 (0.00%)
LC biplane	0.4969 (0.84%)	0.8242 (3.63%)
CC biplane	0.4971 (0.88%)	0.8242 (3.63%)

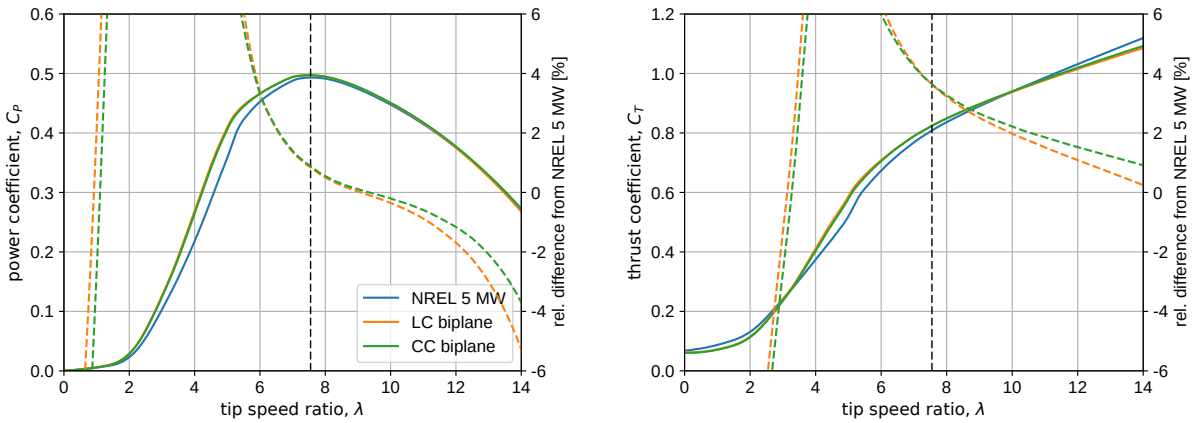

(a) C_P (b) C_T

Figure 3.6: Variation of rotor power coefficient, C_P, and thrust coefficient, C_T, with tip speed ratio, λ. Relative difference of the C_P and C_T distributions from the NREL 5 MW blade is shown in dashed colored lines. Design tip speed ratio of $\lambda = 7.55$ is shown as dashed vertical line.

tip speed ratios in the vicinity of the design point, this could contribute to improved power production under unsteady or turbulent inflow.

The relationship of thrust coefficient with tip speed ratio ($C_T - \lambda$ curves) are shown in Figure 3.6b. The increased C_T of the biplane blades at the design point is apparent. Compared to the baseline blade, the biplanes have increased thrust coefficients at low tip speed ratios (which often occur at high wind speeds) and reduced thrust coefficients at high tip speed ratios (which often occur at low wind speeds). The load implications of this are further examined in Section 3.4.

3.3.2 Local aerodynamic quantities

Additional information about the blade performance is available from the local aerodynamic quantities along the blade span. Some of these distributions are plotted here for operation at the design tip speed ratio of $\lambda = 7.55$.

The axial induction factor, a, is plotted in Figure 3.7a. The baseline monoplane blade is underloaded in the inboard region, producing considerably less than $a = 1/3$; this underloading is a result of structural and manufacturing constraints which limit the chord length and achievable lift of the airfoils used. In contrast, the biplane blades are designed to achieve $a = 1/3$ in the biplane region; because the biplane airfoils have much higher lift coefficients, they are able to achieve optimal loading with less chord than the monoplane blade.

The local angle of attack distributions are plotted in Figure 3.7b, and differ considerably between the monoplane and the biplanes. The high lift biplane airfoils operate at a much lower angle of attack while producing the desired loading. The stall angles are also plotted. Note that for the NREL 5 MW blade, the airfoils very far inboard have a high stall angle due to 3-D stall corrections which have been applied [70]. No such corrections were applied to the polars for the biplane airfoil. The stall margin is directly plotted in Figure 3.7b. With the exception of the near-root region where stall corrections are strongest, the biplane blades have more stall margin inboard. This improved stall margin could improve off-design performance and alleviate stall-induced load fluctuations – flow over the inboard airfoils will stay attached longer in low λ and gusty conditions which result in increased angle of attack along blades, particularly inboard. This, however, also results in increased aerodynamic loads; the implications of this are quantified and discussed in Section 3.4.

The lift coefficient distributions plotted in Figure 3.7d show that the biplane blades indeed operate at higher C_l inboard than the monoplane blade. It is the high lift coefficient of the biplane airfoil configuration which allows the required loading to be produced at a reasonable chord length and angle of attack. The aerodynamic efficiency is shown in Figure 3.7e. For the NREL 5 MW blade, the efficiency increases along the blade span, as the airfoils get thinner. Relative to the NREL 5 MW blade, the biplane blades operate at higher efficiency

inboard of about 15 m, but lower efficiencies outboard. This lower efficiency is the result of the aerodynamic tradeoff described at the end of Section 3.2.1 – the chord continuity constraint forces these airfoils to operate away from their most efficient angle of attack.

The local power coefficients are shown in Figure 3.7f. The monoplane blade has low local C_p along most of the inboard region. This is a result of both the aerodynamic underloading (insufficient lift) and low aerodynamic efficiency of the thick airfoils used inboard. The biplane blades are able to produce adequate loading inboard, and therefore operate at a higher local C_p along most of the inboard region. However, the biplanes do have lower local C_p towards the outboard end of the biplane region due to the reduced operational C_l/C_d there.

This section revealed some of the aerodynamic operating characteristics of biplane blades. As intended, the biplane blades operate much closer to optimal axial induction along the inboard region. The power increases due to this increased induction were offset in part by reductions in local C_l/C_d. Compared to the monoplane blade, the biplane blades operate at higher lift coefficients and at lower angles of attack. This provides increased stall margin, which is one reason for the improved C_P at lower tip speed ratios that was observed in the previous section. The aerodynamic characteristics of the LC and CC biplane blades, were very similar, indicating a general insensitivity of aerodynamic performance to chord length in the biplane region.

3.3.3 Impact of the *merging region* on blade performance

In the above analysis, it was assumed that the blade airfoils transition sharply from a biplane inboard to a monoplane outboard at the joint location. This is an idealization for the aerodynamic simulations; a physically realizable biplane blade would need a joint transition, or *merging region*, as is shown in Figure 3.1, over which the two biplane airfoils merge to a single monoplane airfoil. Due to the complex geometry required to make this transition, there is considerable uncertainty about the impact of the merging region on the rotor aerodynamic performance. The flow in this merging region is likely to have a three-

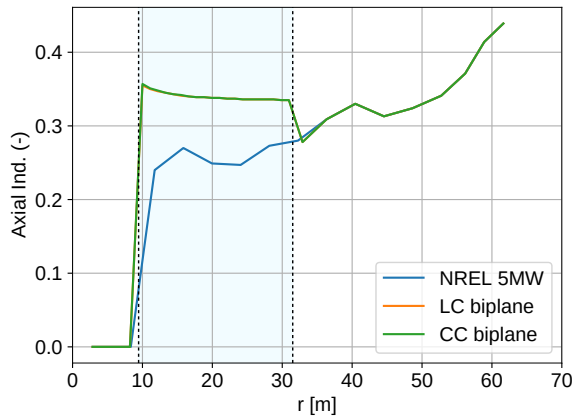

(a) Axial induction factor, a.

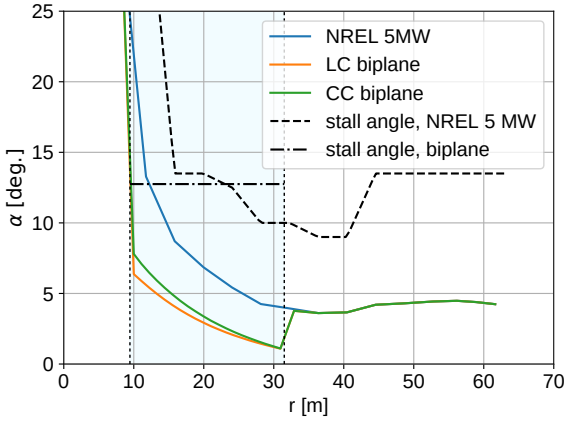

(b) Angle of attack, α.

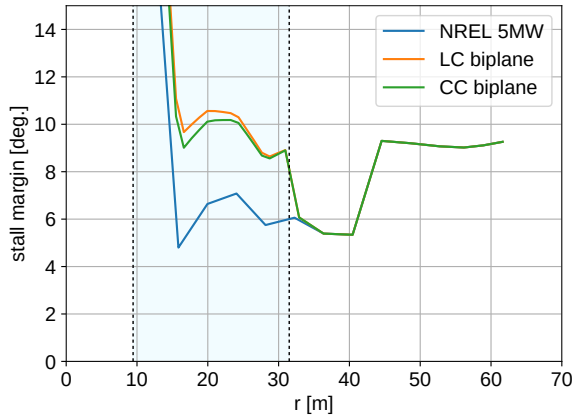

(c) Stall margin.

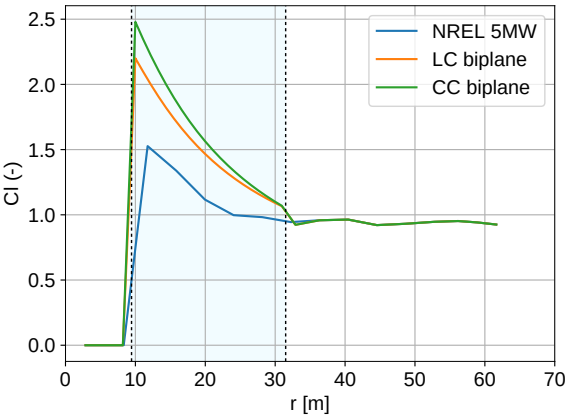

(d) Lift coefficient, C_l.

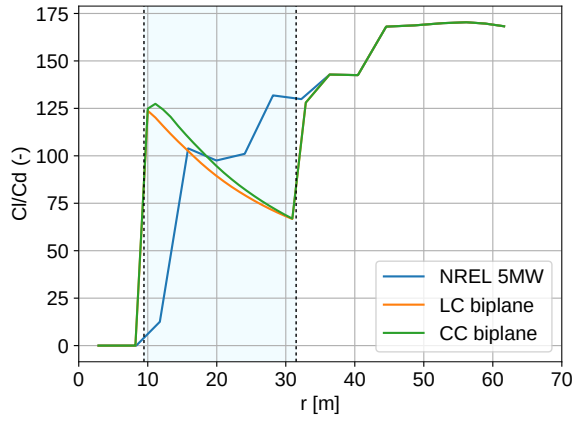

(e) Lift to drag ratio, C_l/C_d.

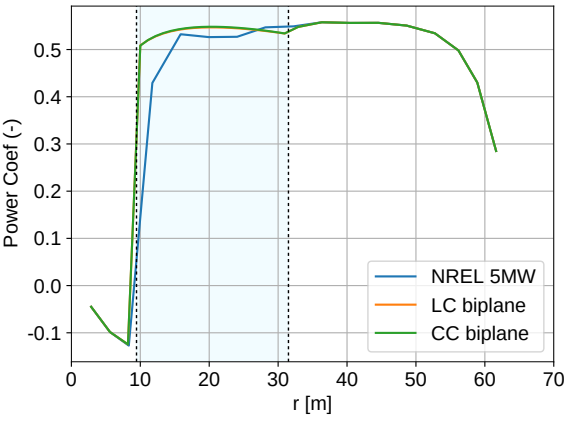

(f) Local power coefficient, C_p.

Figure 3.7: Computed blade distributions for NREL 5 MW, LC biplane, and CC biplane at the design tip speed ratio of, $\lambda = 7.55$.

dimensional component due to the spanwise shape variation, and the aerodynamics of this merging region can only be estimated via three-dimensional, geometry-resolved simulations, or measured directly on a model or full-scale turbine.

It is possible, however, to approximate the aerodynamic losses in this region using simplified blade element momentum theory. In BEM theory, it is assumed that the flow everywhere along the blade is locally two-dimensional. Assuming that drag does not affect the wake, as is often done, the only effect of drag is to create a parasitic force which reduces torque and power. Thus, a simple way to estimate the power loss due to the merging region is to model the merging region as an additional two-dimensional element which produces only drag and no lift. In such an analysis, it is assumed that the merging region can be designed to produce enough lift to give the design axial induction at the joint location.

Taking these assumptions, the contribution to rotor power of a non-lifting element with length dr which sits at a radial location r can be written as

$$dP = -\frac{1}{2}\rho U_{\text{rel}}^2 c(C_d \sin\phi) r dr \Omega \tag{3.3}$$

The local velocity U_{rel} can be extracted from an existing BEM solution which does not contain the draggy element. Thus, the power loss due to the merging region is dependent only on its radial location, r, the element's drag coefficient, C_d, and the length of the element, dr.

The C_P loss for varying joint length dr and sectional drag coefficient C_d is shown in Figure 3.8a. Of course, it is desirable to keep both the length of the merging region and its drag coefficient as low as possible. For a merging region that is 10% of the blade length and has a drag coefficient of 0.10 (about 10 times than would typically be expected for a thin airfoil), the relative change in power due to drag is about -1.2%. Such a loss in C_P would more than offset the gains in C_P when considering the "idealized" biplane blades whose performance was shown in Table 3.2. While in this work we do not make any claim about the required length of the merging region, nor its drag coefficient – these are parameters which likely to be dictated primarily by structural requirements – the figure serves to provide an

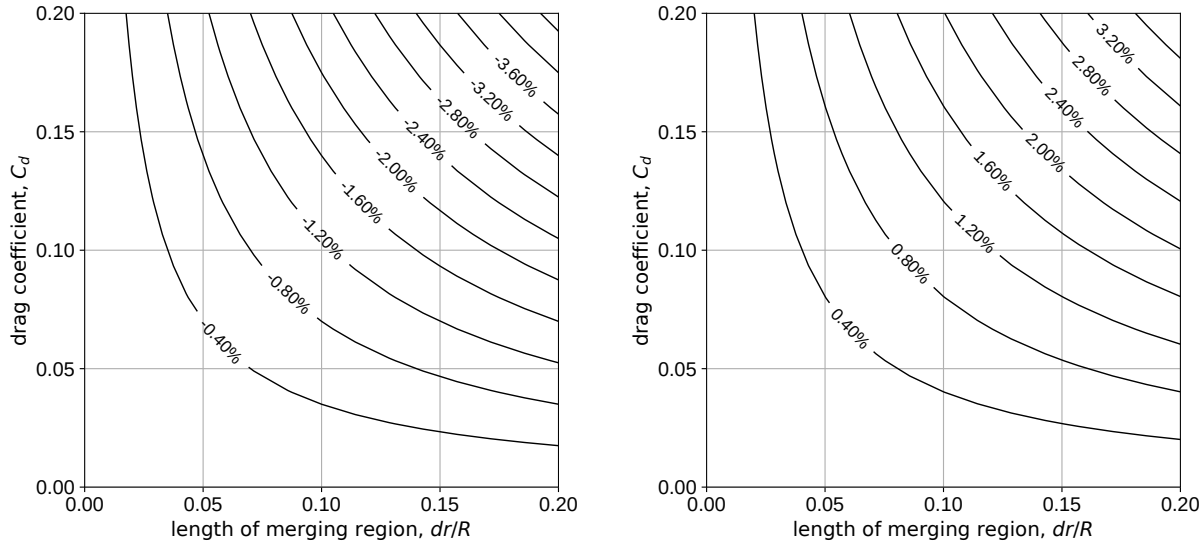

(a) C_P (b) C_T

Figure 3.8: Percent change in rotor power, C_P, and rotor thrust, C_T, attributable to drag of the merging region for varying merging region length, dr, and sectional drag coefficient, C_d.

estimate for the power losses if the value for these two variables can be be estimated.

3.4 Aerodynamic loads

While the aerodynamic performance of blades affects turbine power output, equally important are the aerodynamic loads, which drive the design of the blade structure and the specifications of turbine components downstream of the blade. Wind turbine blades are typically designed for a number of load cases, or combinations of wind events and operating conditions that a turbine may be exposed to in its lifetime. One standard defining a set of such design load cases, or DLCs, is IEC 61400-1 [**?**]. Typically these loads are evaluated using an aeroelastic solver which considers the unsteady aerodynamics and structural dynamics simultaneously. However, for some DLCs, the aerodynamic loads can be estimated without using a full aeroelastic model. In this section, the aerodynamic loads on the NREL 5 MW monoplane blade and those on the LC and CC biplane blades are estimated under a number of conditions – normal operating conditions, under extreme operating gusts, and

under extreme loading while parked. First, the method for calculating the aerodynamic loads is summarized. Then the thrust force distributions, integral rotor thrust, and flapwise root bending for moments for each load case are compared and discussed.

3.4.1 Normal operation - rated speed

In normal operation, the turbine operates at its design tip speed ratio and pitch. Assuming a steady, uniform inflow, the maximum aerodynamic loads occur at the rated wind speed, just before the turbine begins to pitch toward feather after it hits rated power (Region 3). The static loads during normal operation are thus estimated by taking the out of plane force distribution, F'_x, from the BEM simulation at the rated wind speed.

3.4.2 Operating gusts

IEC DLC 2.3 specifies an extreme operating gust which occurs during normal operation. The extreme operating gust for a site with Class A turbulence is plotted in Figure 3.9. As a simplification, instead of computing the dynamic response of the turbine, here the "quasi-steady" gust response is considered. Assuming that the response time of the turbine controller is much longer than the period of the gust step change, then under such gusts, the rotor will operate momentarily at a tip speed ratio above or below its design tip speed ratio, governed by $\lambda_{\text{gust}} = R\Omega/U_{\text{gust}}$. The static loads are then taken by computing the forces on the blade at the tip speed ratio and velocity corresponding to the minimum and maximum velocities in the gust profile. These two conditions are referred to as gust (-) and gust (+), respectively.

3.4.3 Parked extreme wind speed

IEC DLC 6.2 specifies an extreme wind speed event (50 year recurrence period) with loss of turbine connection to the electrical grid. In this event, the turbine experiences an extreme mean wind speed event while idled or parked, with the blades unfeathered and unable to pitch out of the wind; this DLC has been shown to be a design driver for tip deflection and

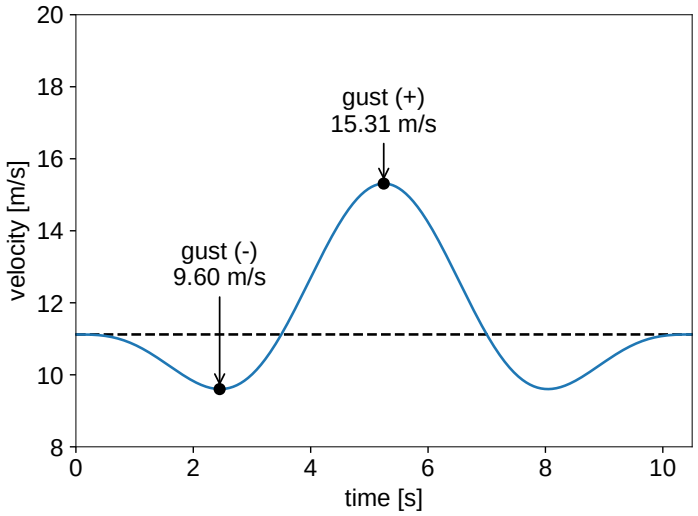

Figure 3.9: Gust velocity profile around the rated velocity (11.4 m/s) for a site with Class A turbulence as specified by IEC 61400-1 [**?**].

ultimate strains in an upscaled version of the NREL 5 MW blade [14]. The magnitude of the extreme wind event, V_{e50} is dependent on the turbine's wind class – 70 m/s for a Class I turbine, 59.5 m/s for a Class II turbine, and 52.5 m/s for a Class III turbine. The static load is estimated using BEM by computing the aerodynamic loads when the turbine operates at a very low tip speed ratio (0.05 is used in the present analysis), and is pitched at 0 degrees.

3.4.4 Comparison of aerodynamic loads

The thrust force distributions for the load cases described above are shown in Figure 3.10, while the integrated blade thrust force and flapwise root bending moments are compared in Figure 3.11. To simplify the comparison, all calculations assume the same rated speed – 11.4 m/s. It should be that the biplane blades, which have higher C_P, would reach rated power at lower wind speeds, and would thus have lower loads than those reported here.

In normal operating conditions, the LC and CC biplane blades have slightly increased thrust in the biplane region, as they are designed for higher axial induction than the mono-plane blade. This manifests as a small increase in total thrust (approximately 4%) over the baseline blade, and a 1.9% increase in flapwise root bending moment. As the thrust increase

is localized to the biplane span of the blade (inboard 50%), the change in root bending moment is smaller than that of the thrust. The negative gust response for the biplane blades is not considerably different from the baseline blade, having small increases in both thrust (3.3%) and root bending moment (1.5%) over the monoplane blade.

The positive gust response of the biplane blades is notably different from that of the baseline blade; the thrust force in the biplane span of the blade is considerably larger than that of the monoplane blade. In positive gusts, the local angle of attack increases; since the biplane airfoils have both increased lift curve slope and max lift coefficient compared to single airfoils, they generate more force at higher angles of attack. This leads to an 11.0% and 9.5% increase in thrust for the CC and LC blades respectively, and a 6.2% and 5.6% increase in flapwise root bending moment. These increased gust forces and moments are undesirable, but could be alleviated by selecting biplane airfoils which have reduced maximum lift coefficients.

In the parked extreme operating condition, the rotor blade presents nearly "flat" to the wind. Since the blade is not rotating, the distributed thrust experienced at any spanwise location is directly proportional to the product of local chord length and drag coefficient (at approximately $\alpha = 90°$). Figure 3.10b, which shows the distributed thrust force for the parked extreme load for a Class I turbine, reflects this – the CC and LC blades, which have much less inboard chord than the monoplane blade, experience much lower distributed thrust forces inboard. For the different biplane blades, the local thrust force is seen to be proportional to the chord for each of the blades; the CC biplane has slighly reduced thrust forces in the biplane region than the LC biplane. These reductions inboard thrust loads lead to 8.6% and 11.0% reductions in the thrust force for the LC and CC biplanes, respectively, and 5.2% and 6.5% reductions in the flapwise root bending moment (these relative differences do not change with the turbine's wind class). For high wind speed (Class I) turbines, it can be seen that the parked extreme load drives both thrust and flapwise root bending moments for all blades considered. For such turbines, the reduced blade thrust of biplane blades enable the use of lower spec and thus cheaper tower/nacelle components. Similarly, the reduced root bending moment allow reductions in blade mass, as the loads are less and less material

is required to support them. Reductions in flapwise root bending moment can also reduce the cost of pitch bearings for biplane blades.

The relative magnitudes of the gust loads and parked extreme loads for varying wind class should be noted. For wind classes I through III, maximum blade thrust always occurs during the parked extreme load; this load case is the driver of thrust forces. For the flapwise root bending moment, however, the driving load case depends on the wind class and on the blade. The maximum flapwise root bending moment of the monoplane blade is always driven by the parked extreme load case. However, for the biplanes, at low mean wind speeds (Class III), it is the operating gust load case which drives maximum flapwise root bending moment – this is due to both the decrease in reduced parked extreme load and the increased gust loads of the biplane blades. For higher wind speeds (Class II, and Class I, and above), it is increasingly the parked extreme load which drives maximum root bending moment. This leads to the following conclusion – in high wind speed sites, the biplane blades experienced reduce flapwise root bending moment, whereas at lower wind speed sites, the increased gust loading provides a lower bound on flapwise root bending moment reductions. As reductions in flapwise root bending moment are closely related to blade mass reductions, this makes biplane blades particularly attractive for higher wind speed sites, including those offshore, where extreme wind speeds can be even higher than a Class I site [74].

In summary, biplanes have the potential to reduce blade thrust and flapwise root bending moment under extreme wind events when compared to the NREL 5 MW monoplane blade. This is due to the reduced chord length of the biplane blades, which reduces loading in the parked extreme load case. The biplane blades do have higher aerodynamic loads under normal operating conditions, and also have have increased loads under operating gusts. However, with the exception of low wind speed (Class III) turbines, the parked extreme load, and not the operating gust load, is the driver for both thrust and flapwise root bending moments. These load reductions act in concert with the improved structural efficiency of the biplane structure to enable further increases in blade mass, and to reduce the cost of downstream turbine components.

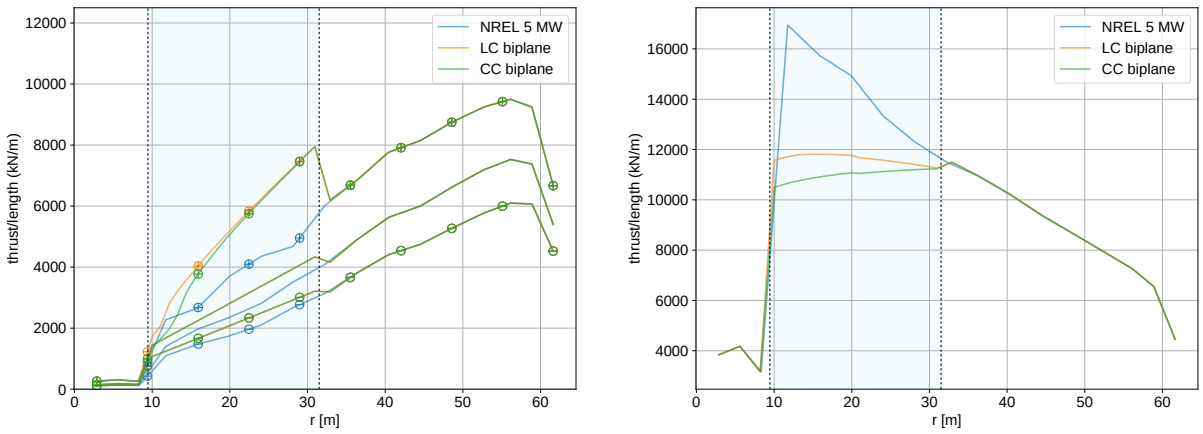

(a) normal operation, rated speed +/- gust

(b) parked extreme (Class I)

Figure 3.10: Out of plane force per unit length, F'_x, for normal operation at rated speed, rated speed operation with extreme gust, and parked extreme load. In Figure 3.10a, the series with + and - markers correspond to the gust (+) and gust (-) conditions, respectively.

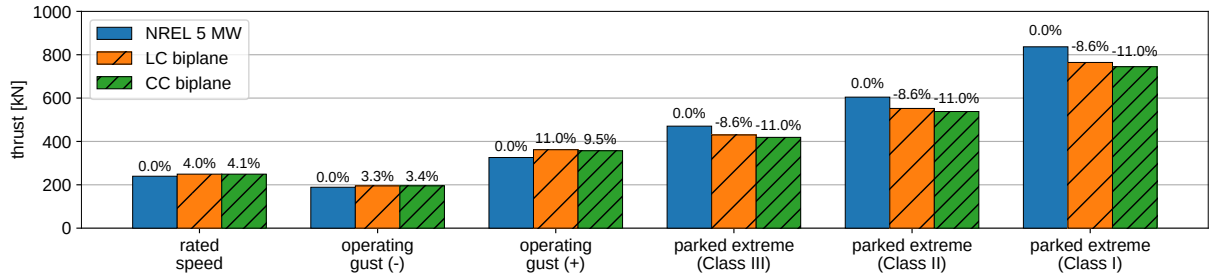

(a) integrated blade thrust

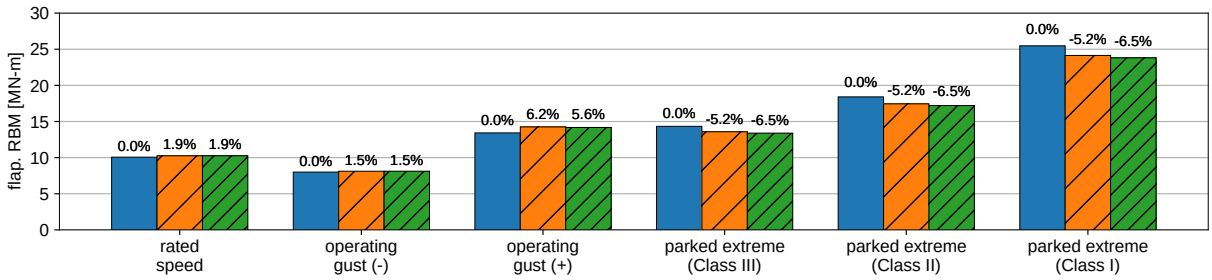

(b) flapwise root bending moment (RBM)

Figure 3.11: Integrated blade thrust and flapwise root bending moment for blades for a variety of operating conditions. Class I can be considered representative of offshore sites, where extreme wind speeds are high and load reductions are significant.

3.5 Conclusions

This work considered the aerodynamic design, performance, and steady loads of biplane wind turbine blades. In summary, the results show that biplane blades can be designed to have comparable or better aerodynamic performance than conventional monoplane blades, with less chord, and with reduced loads in extreme conditions.

Using the NREL 5 MW monoplane blade as a reference, two biplane blades were designed to give optimal loading. In order to prevent discontinuous chord distributions, these blades were designed with different prescribed chord distributions – one with a linear chord (LC) and one with a constant chord (CC). Due to the high lift of the biplane airfoils, both LC and CC biplane blades had reduced chord when compared to the monoplane blade while maintaining higher inboard loading. This chord reduction is a critical advantage for transportability, especially when considering longer blades.

Using blade element momentum (BEM) analysis it was shown that the aerodynamic performance of the biplane blades is slightly improved over the monoplane baseline blade (less than 1% improvement in C_P). The high lift of the biplane airfoils allowed for better loading inboard, where the baseline blade was limited by chord length constraints. Increases in local power coefficient attributable to the more optimal loading of the biplane blades were offset by reductions in local C_P which result from having to run the biplane airfoils at a non-optimal angle of attack in order to enforce a smooth chord distribution for the biplane blades. The effect of the merging region on power performance was also quantified; it was shown that improvements in C_P can be offset by drag losses in the merging region, but the total loss in C_P was dependent both on the length of the merging region and its drag coefficient. The biplane blades had a broader $C_P - \lambda$ curve, indicating that the "real-world" AEP (in unsteady or turbulent inflow) may be improved over that of the baseline blade; however, aeroelastic simulations would be required to quantify this difference. With regards to aerodynamic performance, there is little to choose between the LC and CC biplane blades, indicating that the aerodynamic performance is relatively insensitive to the particular chord distribution used for the biplane span of the blade.

The steady aerodynamic loads were computed for a number of design load cases. As a result of their reduced chord, the biplane blades were shown to reduce parked extreme thrust by as much as 11.0% and root bending moment by as much as 6.5%. These load decreases could enable both mass reductions of the blade itself (acting together with the improved flapwise structural efficiency of the biplane structure). In addition, load reductions enable cost reductions in downstream turbine components such as pitch bearings and the tower. The biplane blades do have increased gust loads, but these gust loads are only design-driving for low wind speed (Class III) turbines and can be mitigated through more judicious choice/design of the biplane airfoils. With regards to aerodynamic loads, the CC biplane, which has less chord than the LC biplane, is preferable, having both lower gust loads and extreme loads. The reductions in extreme loads may be particularly useful for offshore sites which experience extreme wind conditions in hurricanes or typhoons.

It should be noted that in this work, the aerodynamic design and analysis used simple BEM theory. However, it has been shown [21] that designs using BEM can result in rotors which have less loading than what is required for maximum C_P. This is particularly important for biplane blades, as biplane airfoils provide the capacity to generate more inboard loading while still maintaining reasonable chord lengths. In future work, higher fidelity simulations such as actuator line or vortex lattice methods should be explored to investigate the potential for improved C_P through further increased inboard loading enabled by biplane blades.

While the structural performance of the particular blades analyzed here was not examined, past work indicates that biplane blades have significantly improved flapwise structural efficiency compared to monoplane blades; the same is expected to be true of the biplane blades designed here. In conjunction with the demonstrated loads reduction, it is likely that for the same power output, biplane blades can be built significantly lighter than conventional blades. One approach to quantifying this mass reduction would be through an optimization which seeks to minimize blade mass, similar to the approach taken in [75] – this is a direction for future work.

Lastly, it should be noted that the biplane blades considered here were designed using a

relatively simple approach. Considerable improvements in performance and load reductions could be enabled through a more systematic optimization of the biplane blade itself.

Based on the computed aerodynamic performance, extreme load reductions, expected structural performance, and the favorable design characteristics discussed above, biplane blades are an enabling concept for the next generation of large land-based and offshore turbines.

CHAPTER 4

Mass reductions enabled by biplane wind turbine blades

Biplane wind turbine blades have been shown to have improved structual performance, aerodynamic performance, and reduced aerodynamic loads compared to conventional blade designs. Here, the impact of these factors is examined collectively for the first time. The objective of this work is to quantify the mass reductions enabled by biplane wind turbine blades, considering their structures and aerodynamics simultaneously. A numerical optimization approach is used to design the internal structure of biplane wind turbine blades, minimizing blade mass subject to a number of design requirements which are imposed as constraints. The mass reductions are significant, showing that the optimal biplane blades are more than 45% lighter than a similarly-optimized monoplane blade. This is primarily due to the improved resistance to flapwise deflection when compared to the monoplane blades, which allows for considerably less spar cap material to be used in the biplanes. Biplane blades are also shown to have improved resistance to edgewise fatigue damage, and it is shown that longer blades experience greater relative mass reductions than shorter ones. Given such large mass reductions, some criticality is required, and the limitations of the present approach are discussed. The results of the optimization present strong evidence that biplane wind turbine blades are an enabling concept for the next generation of lighter, larger, and more cost-effective wind turbine blades.

4.1 Introduction

Biplane wind turbine blades are a concept in which a biplane inboard merges to a monoplane outboard [45]; this design has improved structural, aerodynamic, and design characteristics when compared to conventional monoplane blades. With regards to the structural performance, biplane blades have approximately 30% less tip deflection than conventional blade designs of the same mass [42, 7]. Concerning aerodynamics, the high lift biplane airfoils enable increased loading in the inboard region of the blade, a region of the blade which for conventional designs is typically underloaded due to chord length constraints; this increased loading leads to improved rotor power coefficients [46, 76]. In addition, less chord length is required in the biplane region, leading to significant load reductions under certain extreme wind events [76]. The lower chord length also improves transportability, as the chord length of turbine blades transported over-land is constrained by road, tunnel, or underpass sizes [72].

Past research has been critical in demonstrating and understanding the structural performance of simple biplane wind turbine blades. In addition, the aerodynamic performance of such blades has also been quantified, showing small improvements over conventional blade designs. The aerodynamic loads of biplane blades are increased in some load cases (gusts) and decreased in others (parked extreme loads). The design of wind turbine blades, however, is a multi-disciplinary process in which all of these factors play a role. Therefore a design approach in which considers the aerodynamic performance, aerodynamic loads, and structural response simultaneously is necessary. The goal of wind turbine blade design is to minimize the turbine's cost of electricity (COE), typically measured in \$/kWh. When considering the design of a blade only, the COE is closely correlated to the cost of a blade/rotor divided by its annual energy production (AEP). Considering that blade cost and mass are also closely correlated (due to material cost), then a blade design should minimize m/AEP.

In this work, an optimization is applied to minimize the mass of a number of biplane wind turbine blades whose chord, twist, and airfoil distributions are defined *a priori* and fixed. This is achieved by formulating the internal structural design of a wind turbine

blade as an optimization to minimize blade mass, subject to realistic constraints on the blade's tip deflection, material strains, and fatigue damage. The objectives of this work are 1) to quantify the mass reductions enabled by a practical biplane blade design, and 2) to understand what drives the optimal internal structure for such blades. A computational framework was developed to solve this optimization problem, and was used to design the internal structure of two 100 m biplane wind turbine blades with different chord distributions. The same framework was applied to optimize a 100 m monoplane blade, which is used as a reference for comparison.

The results of this optimization show dramatic mass reductions for biplane blades. Subject to the same constraints, biplane blades can be designed with as much as 46.2% reduced mass compared to the optimized monoplane blade. This is primarily due to the increased resistance to tip deflection, which allows considerable spar cap material to be removed. The biplane blades are also shown to have reduced edgewise fatigue damage, requiring less trailing edge reinforcement material. This reduction in edgewise fatigue damage is shown to increase relative mass reductions between biplane and monoplane blades as blade size is increased.

First, the optimization problem is formalized and the modeling approaches and computational framework detailed. The optimization is applied to the design of 100 m biplane and monoplane blades, and the results compared and analyzed. Trends with blade length are shown by applying to same optimization to blades with varying lengths. The paper concludes with a discussion of the limitations of the present approach and a discussion of future directions for this research.

4.2 Approach

The approach of this work is to, through numerical optimization, design the internal structure of a biplane wind turbine blade in a way which minimizes mass while still meeting a number of design requirements. Here, a number of design requirements are considered:

- **Tip deflection**. Blades must be designed to prevent tower strike. During normal

operation, the tip deflection of the blade under must be sufficiently small as not to collide with the tower should the turbine experience a sudden gust.

- **Ultimate strength**. Blades must be designed to survive extreme loads. This requires the actual strains in the material under extreme loads to be less than the material's ultimate strains. In addition, no buckling of any form should occur, as this is usually accompanied by failure.

- **Fatigue life**. Blades must endure fatigue loads. In typical wind turbine blades, the primary fatigue load is that due to the gravity, which produces a cyclical and reversing edgewise moment distribution in the blade. The blade must be designed with adequate edgewise stiffness such that this cyclical loading does not cause failure over its lifetime.

- **Natural frequencies**. The natural frequencies of the designed blades should be sufficiently high as to prevent interaction with common turbine oscillation frequencies.

Given these design requirements, the internal structural design can be formulated as an optimization of the form

$$\begin{aligned} &\underset{x}{\text{minimize}} && f(x) \\ &\text{subject to} && g_i(x) \leq 0, \quad i = 1, \ldots, m \end{aligned} \tag{4.1}$$

where x is the set of design variables, $f(x)$ is the objective function and $g_i(x)$ are inequality constraints. Applied to the blade design problem here, the objective function $f(x)$ we seek to minimize is the blade mass, where x is a set of variables parameterizing the blade internal structure. The design requirements for tip deflection, ultimate strength, buckling, fatigue damage, and natural frequency are imposed as inequality constraints $g_i(x)$.

4.2.1 Modeling approaches

The evaluation of the objectives and constraints described above requires modeling of the blade structure to accurately compute blade mass, deflection response to loads, material

stresses/strains, and buckling failure modes. In the present work, a beam model is used for assessing the deflection, natural frequencies, and internal forces and moments of blades under load. A mid-fidelity cross section model is used to compute the beam cross sectional properties and the material stresses/strains under the internal forces and moments. The blade aerodynamic loads themselves are computed using blade element momentum theory. This section details these modeling approaches.

4.2.2 Structural modeling

A simplified beam model is used for the computation of deflections and internal moments under external loading. This model is shown in Figure 4.1. The monoplane blade (Figure 4.1a is modeled as a single cantilevered beam, where the fixed root represents a connection to a presumed rigid blade hub. The biplane blades (Figure 4.1b), are modeled as two cantilevered beams and a single beam outboard of the joint. The cantilevered beams and outboard beam are affixed (rigid connection) at the blade joint with a massless rigid plate. The branches of the biplane region of the blade are separated by one chord distance from each other, which matches the gap of the airfoil configuration which was used in the blade design [76]. The beams are constructed to pass through the elastic centers of the cross sections. For both the monoplane and biplane beam models, the fixed inboard boundary is at $r/R = 15\%$, neglecting the most inboard region of the blade which is responsible primarily for transitioning the blade shape from the root fixture to a lifting shape. For both the monoplane and biplane beam models, the stiffness and mass distributions along the blade span are computed from the cross sections directly. External loads are applied to this model as distributed loads along the beams. Gravitational loads, which are required for calculating the fatigue damage, are computed directly from the distributed beam mass properties.

The multi-body finite element analysis tool *DYMORE* [77] is used to solve the beam problem. A beam model is generated for a blade based on its geometry and cross sectional properties, using 3rd-order 1D Timoshenko elements. The distributed beam properties (6x6 stiffness and mass matrices) are defined at stations along the beam elements. Aerodynamic

loads are applied as static external loads. The finite element problem is solved, and the internal beam forces/moments computed. *DYMORE* is also used to solve for the moments resulting from blade self weight.

A number of simplifications are made in the beam model. The effect of airfoil twist is ignored; this is thought to be a reasonable assumption, as the twist angle is small for most of the blade. A number of simplifications are also made with regards to the distributed cross-sectional stiffness properties. The two diagonal shear stiffness terms and the torsional stiffness term are assumed to be very large compared to all other terms in the stiffness matrix. All off-diagonal terms in the matrix set to be zero, implying no coupling between the stiffnesses in any direction. Thus, the 6x6 stiffness matrix reduces to a diagonal one. The two bending stiffnesses and axial stiffness are populated with real numbers, while the shear and torsional stiffnesses are assigned large values. With these simplifications, the problem reduces to classical Euler-Bernoulli theory. In preliminary analyses of untwisted blades, the effect of these assumptions on tip deflection and internal forces/moments was shown to be small (see Appendix B). While these terms can be important when assessing the aeroelastic response of blades, this was not not a concern of the present study. The described simplifications in the beam properties allow for the cross section properties to be computed using the fast PolyCX tool described in Section 4.2.3 – the speed of this tool is critical in optimization in which the cross section properties must be evaluated many times.

4.2.3 Cross-sectional modeling

The distributed beam properties (mass and stiffness) for the beam model described above are computed from a representative cross section model. This model, shown in Figure 4.2, includes the exterior and interior shell layers, spar caps, trailing edge reinforcement, and shear webs – these are thought to be the primary contributors to mass and bending stiffness for cross sections. The topology is a conventional one, with an exterior and interior shell layers, spar caps to give flapwise bending stiffness, shear webs, and trailing edge reinforcement to provide edgewise bending stiffness.

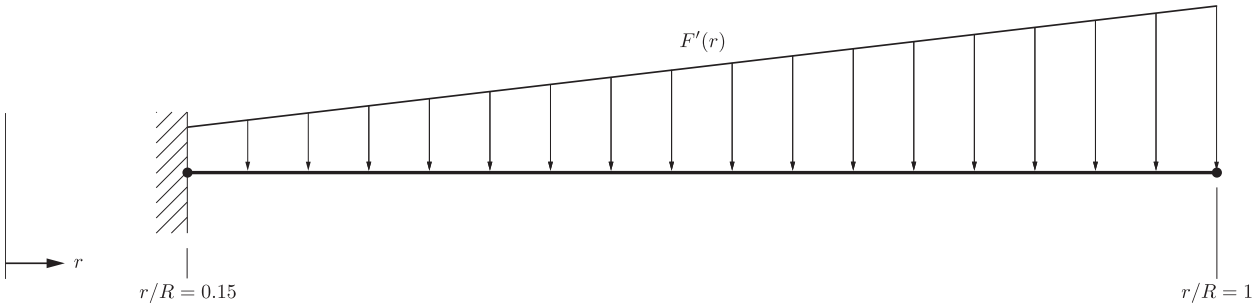

(a) Monoplane

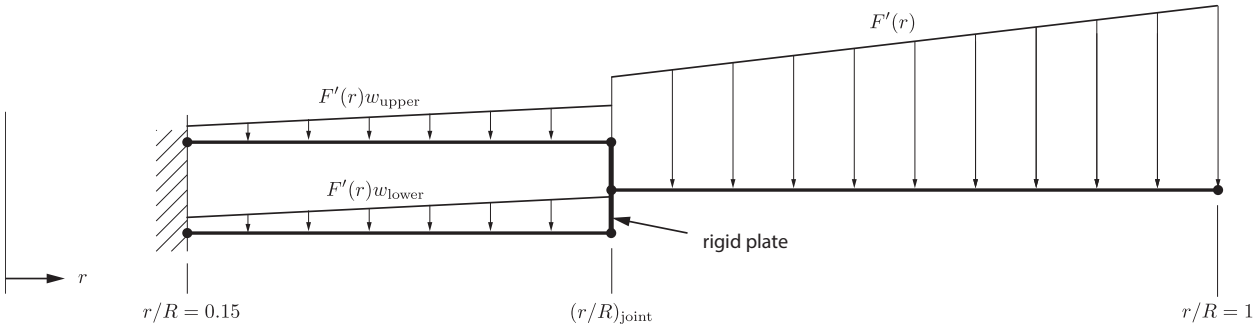

(b) Biplane

Figure 4.1: Beam models used for monoplanes and biplanes. Monoplane blades are modeled as a single cantilevered beam. The biplane blades are modeled as three beams, affixed at the blade joint with a massless rigid plate. Although shown as straight beams, in general these beams are curved and pass through the elastic centers of the cross sections. Aerodynamic external loads are applied as $F'(r)$; a linear load profile is shown, but the applied loads may be of arbitrary shape. For the biplane, aerodynamic loads in the biplane region are split between the upper and lower branches via the weighting factors w_{upper} and w_{lower}. Here, $w_{\text{upper}} = w_{\text{lower}} = 0.5$.

In real blades, core material is typically added in between the shell layers at the leading and trailing edges to prevent panel buckling. In the present analyses, however, panel buckling is not considered. Panel buckling failure is normally encountered in large unsupported panels. The biplane blades, with their smaller chord lengths, have much smaller unsupported panel sizes and are therefore less likely to experience panel buckling failure. Thus, as a simplification, core material between the exterior and interior shell is not modeled; this is likely to lead to conservative estimates of the mass reductions available from biplane blades.

The material properties are taken from the Sandia reference blade. The spar caps and trailing edge reinforcement are comprised of E-LT-5500/EP-3 uniaxial material, while the exterior and interior shell layers are both comprised of "SNL Triax,". Biaxial Saertex/EP-3

is used for the shear web outer laminate, and a representative foam is used for the shear web cores. The relevant properties of these materials are summarized in Table 4.1. These original source of these material properties is the DOE/MSU materials database [78].

Cross sections are generated and analyzed using PolyCX, an in-house tool developed in Python for this effort. This tool has three core functionalities – generation of cross section geometries from a set of parameters, calculation of cross sectional properties (stiffness/mass), and evaluation of local strains/stresses on a cross section from applied forces/moments. In PolyCX, cross sections are comprised of multiple "elements," each of which is defined by its shape (as a polygon) and its material properties. The geometry of the cross sections are generated using an "outside-in" approach, starting with an exterior airfoil shape and building up internal elements sequentially using polygon operations. The generation of the cross section is parameterized – given an airfoil shape, the cross section topology is fully defined by nine parameters: the exterior shell thickness, $t_{\text{shell, ext}}$, spar cap start location, $x_{\text{sc, start}}$, spar cap end location, $x_{\text{sc, start}}$, spar cap thickness, t_{sc}, interior shell thickness, $t_{\text{shell, int}}$, shear web laminate thickness, $t_{\text{sw, lam}}$, shear web core thickness, $t_{\text{sw, core}}$, trailing edge reinforcement width, w_{ter}, and trailing edge reinforcement thickness, t_{ter}. These parameters are depicted in Figure 4.2.

The Python library Shapely [79] is used to perform the geometry-generating polygon operations efficiently and robustly. Shapely is a Python wrapper for the GEOS geometry engine [80], written in C++. The cross section's properties are computed by summing the contributions of each element. The cross sectional mass per unit length, m', is computed as

$$m' = \sum_{i=1}^{n} \rho_i A_i \tag{4.2}$$

Similarly, the total cross sectional stiffnesses $[EI]_x$, $[EI]_y$, $[EI]_{xy}$, and $[EA]$ are computed

by summing the individual element stiffness contributions

$$
\begin{aligned}
[EI]_x &= \sum_{i=1}^{n} E_i I_{i,x} \\
[EI]_y &= \sum_{i=1}^{n} E_i I_{i,y} \\
[EI]_{xy} &= \sum_{i=1}^{n} E_i I_{i,xy} \\
[EA] &= \sum_{i=1}^{n} E_i A_i
\end{aligned}
\tag{4.3}
$$

where I_x, I_y, and I_{xy} are the second moments of area of each element. Since each element is represented as a polygon, the second moments of area, I_x, I_y, I_{xy} can be computed using the following equations which give the second moments of area of arbitary polygons defined by n exterior points

$$
\begin{aligned}
I_x &= \frac{1}{12} \sum_{i=1}^{n} (y_i^2 + y_i y_{i+1} + y_{i+1}^2)(x_i y_{i+1} - x_{i+1} y_i) \\
I_y &= \frac{1}{12} \sum_{i=1}^{n} (x_i^2 + x_i x_{i+1} + x_{i+1}^2)(x_i y_{i+1} - x_{i+1} y_i) \\
I_{xy} &= \frac{1}{24} \sum_{i=1}^{n} (x_i y_{i+1} + 2x_i y_i + 2x_{i+1} y_{i+1} + x_{i+1} y_i)(x_i y_{i+1} - x_{i+1} y_i)
\end{aligned}
\tag{4.4}
$$

From the local bending moments (M_x, M_y) and axial forces (N_z), the local strains are computed as

$$
\epsilon(x, y) = \frac{M_x}{[EI]_x} y - \frac{M_y}{[EI]_y} x + \frac{N_z}{[EA]} \tag{4.5}
$$

From elasticity, local stresses in the i-th element are computed as

$$
\sigma(x, y) = \epsilon(x, y) / E_i \tag{4.6}
$$

It should be noted that existing software tools (e.g., VABS [81, 82], BECAS [83]) are capable of performing similar analyses, and with higher fidelity, computing the full cross sectional

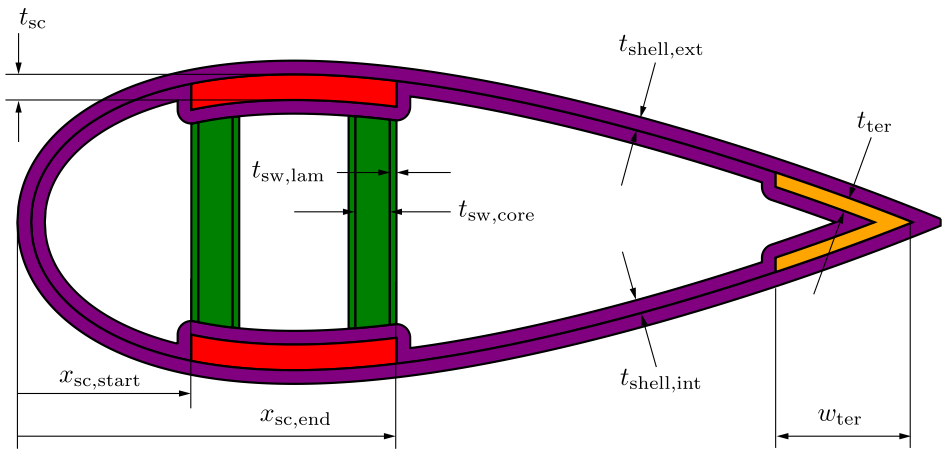

Figure 4.2: Cross section model consisting of exterior and interior shell layers, spar caps, trailing edge reinforcement, and shear webs. The geometry is completely defined by the labeled parameters which define component thicknesses and, where applicable, widths. Elements are not drawn to scale.

Table 4.1: Summary of material properties. Material properties are taken directly from the SNL 100 blade.

Material Name	Mass		Elastic Constants		Tension		Compression	
	VF [%]	Density [kg/m^3]	E_L [GPa]	E_T [GPa]	UTS$_L$ [MPa]	ϵ_{max} [μstrain]	UCS$_C$ [MPa]	ϵ_{min} [μstrain]
E-LT-5500/EP-3	54	1920	41.8	14.0	972	24,400	-702	-15,300
Saertex/EP-3	44	1780	13.6	13.3	144	21,600	-213	-18,000
SNL Triax	-	1850	27.7	13.7	558	23,000	-458	-16,650
Foam	-	200	0.256	0.256	-	-	-	-

properties including shear stiffnesses, torsional stiffnesses, and cross-coupling terms. These tools are based on finite element representations of the cross section, and require meshing of the geometries before the cross sectional properties can be computed, a step which is difficult to automate robustly for use in optimization. In addition, the computational time for the entire process (meshing and computing the cross sectional properties) is considerably slower than that of the approach discussed above. Computational time is of critical importance since the cross sectional properties must be computed many times during an optimization campaign. PolyCX was developed for robustness and speed, using fast, vectorized computations where possible. The cross sectional properties computed by PolyCX are compared to higher fidelity tools in Appendix C.

4.2.4 Aerodynamic loads

Aerodynamic loads are computed using blade element momentum theory. An "extreme operating gust" gust condition is specified in IEC standard 61400-1 [**?**], and it is assumed this gust drives the maximum tip deflection. The aerodynamic loads under the extreme operating gust condition are computed assuming the turbine experiences the gust suddenly and cannot adjust its speed accordingly. It is assumed that the ultimate strains and buckling modes are driven by the "parked extreme" operating condition, an IEC load case in which the blades are pitched at 0°, the rotor is nearly stationary, and a large mean inflow velocity is experienced. Aerodynamic loads under that condition are computed by taking the loads when the rotor is nearly stationary, and experiences a large large mean inflow velocity.

The *WT Perf* BEM code [73], developed by NREL, is used to compute the blade aerodynamics for the purposes of evaluating external loads. Additional details on this approach for computing aerodynamic loads can be found in [76].

4.2.5 Overall computational framework

An object-oriented computational framework was developed in Python to solve the optimization problem described above. This framework consists of an optimizer which wraps the various solvers described in the previous section, pre-processing tools to develop input files for the solvers, and a number of routines to compute the objective and constraint functions from the raw solver outputs. An overall diagram of the framework is shown in Figure 4.3.

4.2.6 Description and computation of constraints

This section describes each of the constraints and its method of calculation in more detail.

4.2.6.1 Tip deflection

The tip deflection of the blades is computed under the IEC "extreme operating gust" (EOG) condition, which specifies a gust experienced by the turbine during otherwise normal

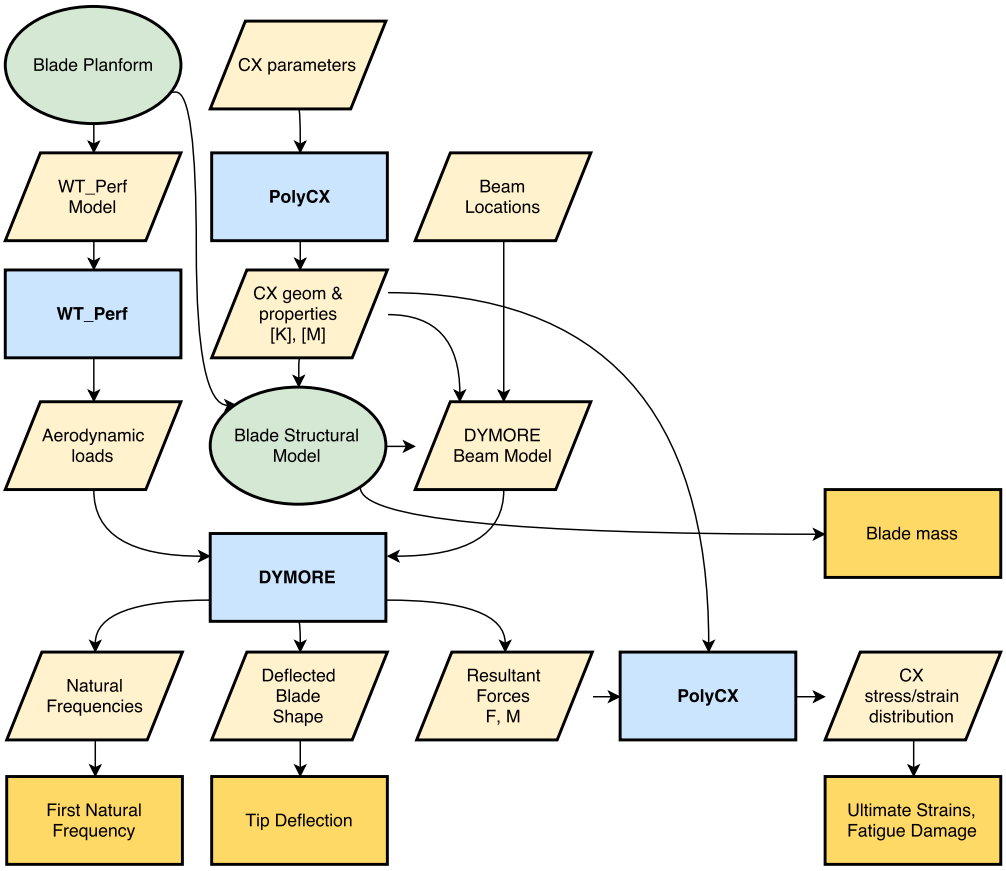

Figure 4.3: Diagram of computational framework showing the data flow for a single "evaluation." The cross section (CX) parameters are varied by the optimizer, which takes gradients of the objective (blade mass) and constraint functions (natural frequency, tip deflection, ultimate strains, fatigue damage), with respect to the CX parameters.

operation. The tip deflection is constrained to be 7% of the blade radius, a value which was chosen to be representative of a typical tip deflection constraint. In reality, maximum allowable tip deflection is related to the blade tip/tower clearance, which is affected by turbine shaft tilt and blade coning. No safety factor is applied to the tip deflection load.

4.2.6.2 Ultimate strains under extreme aerodynamic load

Ultimate strains are computed under the IEC "parked extreme" load case, in which the parked turbine experiences a 50-year mean wind speed event. For this analysis, a Class I wind site is assumed, giving an extreme mean wind speed of $V_{e50} = 70$ m/s (per IEC 61400-4) [**?**]. A partial safety factor (PSF) of 1.35 is used on the aerodynamic loads for this case. The

internal forces are computed from the beam model, and the maximum local strains in each cross section computed using PolyCX. It is assumed that the maximum strains occur in the exterior shell layer, since this layer is guaranteed to be the farthest distance from the cross section's elastic center.

The ultimate strains are constrained to 10,000 μstrain in both tension and compression. The exterior shell material is SNL Triax material, and it can be seen from the material properties in Table 4.1 that this material can endure ultimate strains of 23,000 μstrain in tension and -16,650 μstrain in compression. Thus, the applied limit represents material safety factors of 2.30 in tension and 1.67 in compression.

4.2.6.3 Fatigue damage due to cyclical self-weight moments

Edgewise fatigue damage is computed using Miner's rule. All edgewise fatigue damage is assumed to be attributable to blade self-weight internal moments which fully reverses between the blade's 3 o'clock and 9 o'clock positions. In addition, as a simplification it is assumed that the material lifetime is of the form

$$N_f = \left(\frac{1}{c} S\gamma\right)^b \tag{4.7}$$

where N_f is the number of cycles to failure, c is the single cycle strength, S is the applied stress level, γ is a combined stress/material partial safety factor (PSF), and b is a parameter fitting material test data. Here it is assumed that $b = -10$. The fatigue damage is calculated as

$$D_{\text{fat}} = \frac{N}{N_f} = \frac{N}{\left(\frac{1}{C} S\gamma\right)^b} \tag{4.8}$$

where N is the number of cycles at the given stress level. A value of $D_{\text{fat}} \geq 1$ indicates material failure due to fatigue. As a simplification, the number of cycles N is computed assuming that the blades operate at their rated RPM for 20 years, which is likely to lead to conservative (high) estimates of the damage. It is assumed that fatigue is critical only in the exterior shell of the blade, which is a reasonable assumption as this is the material

layer which experiences the highest stresses. Here, the fatigue properties for the exterior shell material are taken from the DOE/MSU database [78]. The single cycle strength c is determined by taking the y-intercept of a linear fit to log/log fatigue test data. A partial safety factor of $\gamma = 1.634$ is used in the present analyses.

4.2.6.4 Natural frequencies

The natural frequencies are computed via eigenanalysis in *DYMORE*. Here we are only interested in the frequency of the first (lowest) natural frequency; this frequency should be adequately separated from the rotor 3P (three-per-period) frequency. The 3P frequency can be excited as a result from blade passage through sheared inflow, by edgewise gravity loads, or from blade/tower aerodynamic interactions.

4.2.6.5 Beam buckling

For biplane blades, an applied flapwise load leads to tensile and compressive axial loads in the branches of the biplane blade – for an example of this, see Figure 4.8b. For the branch of the biplane which is under compression, this introduces the potential for a beam buckling failure mode. A simple way to estimate the biplane's response to this failure mode is by estimating the critical buckling load of the biplane branch using Euler's critical load formula.

$$P_{\text{cr}} = \frac{n\pi^2 EI}{L^2} \tag{4.9}$$

where L is the length of the column, EI is the minimum principal bending stiffness along the column, and n is a factor which is used to account for boundary conditions at the column ends. In this analysis, $n = 2$ is used, corresponding to fixed/hinged boundary conditions. The column length L is the length of the biplane branch, and the value for EI is chosen as the minimum principal stiffness of any cross section in the beam. Then, a beam buckling load factor, LF_B can be computed as

$$\text{LF}_B = \frac{P_{\text{cr}}}{P} = \frac{n\pi^2 EI}{PL^2} \tag{4.10}$$

where P is the magnitude of the maximum compressive axial force in the biplane branch. A value of $\mathrm{LF}_B < 1$ indicates failure by buckling. For this computation, the internal axial loads are extracted from the output of the beam solver; the minimum cross sectional stiffnesses are computed from the cross sectional properties via PolyCX.

4.3 Problem Setup

4.3.1 Blade planforms – chord and airfoil shapes

In this work, the internal structure of a number of three 100 m blade planforms are optimized – two biplane blades with different chord distributions, and a reference monoplane blade. The monoplane planform used for reference is the SNL 100, a research blade whose planform and aerodynamic/structural details are publicly available [14]. Of the two biplane blades, one uses a linear chord distribution in the biplane region (LC biplane) and one a constant chord (CC biplane); the biplane blades were designed in [76] to produce optimal loading and to have smooth chord distributions. The SNL 100, CC biplane, and LC biplane were all shown to produce rotor power coefficients within 1% of each other, with both biplane blades having slightly higher C_P than the reference monoplane. The chord distributions for all blades are shown in Figure 4.4a. As can be seen, the chords of both of the biplane blades are significantly reduced compared to the monoplane blade; this is due to the higher lift of the biplane airfoils which allows comparable loading to be generated with less chord. Both biplane blades were designed by replacing the inboard region of the SNL 100 blade with a biplane comprised of two 25% thick airfoils; ouboard of the joint, the blade is identical to the SNL 100.

The absolute and relative thickness distributions of the three blades are compared in Figure 4.4b. The relative thickness for both biplane blades is constant at 25% in the biplane region, since both branches of the biplane blade use 25% thick airfoils throughout. In contrast, the relative thickness of the monoplane blade reaches 50% at 15% of the blade span. As expected, the absolute airfoil thicknesses are shown to be linear for the LC biplane and

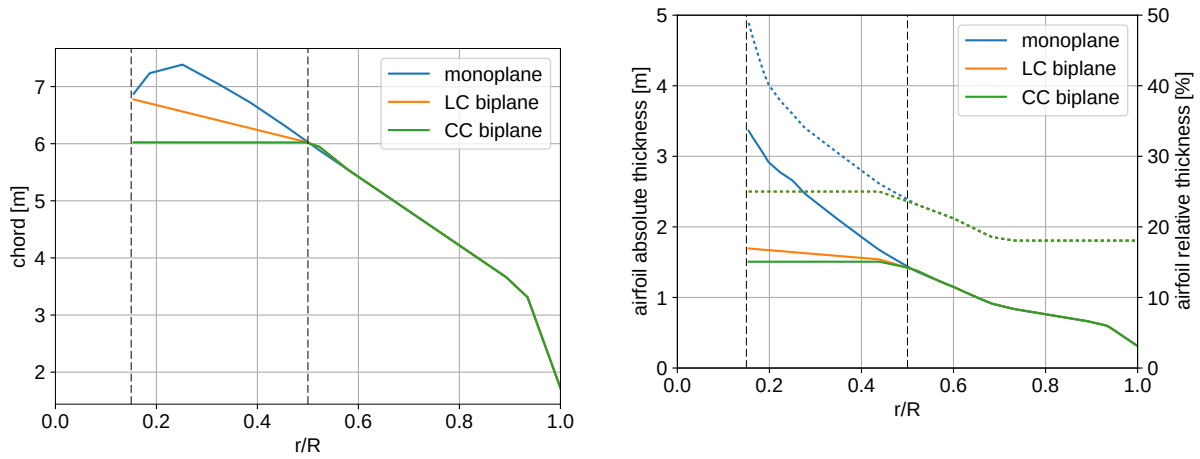

(a) chord

(b) absolute thickness (solid), relative thickness (dotted)

Figure 4.4: Chord and thickness distributions for the monoplane, LC biplane, and CC biplane blades. The relative thickness distributions of the LC biplane and CC biplane (figure 4.4b) are identical.

constant for the CC biplane. For the purposes of this study, the actual airfoil shapes are replaced with NACA 4-digit airfoils of the same thickness as the specified airfoil. This simplification was used to provide distributions of the cross section shapes which vary smoothly along the blade span, as the cross section shapes specified by the original SNL 100 blade do not.

The computed aerodynamic loads on these blades in two design driving conditions are compared in Figure 4.5. It can be seen that the gust loads on the biplane blades are larger than those on the monoplane blade, but that the extreme loads are significantly reduced. The design methodology, aerodynamic performance, and loads on the biplane blades are described in more detail in [76].

4.3.2 Parameterization and parameter reduction

The cross section geometries described in Section 4.2.3 are parameterized using nine independent variables. In order to reduce the number of degrees of freedoms (DOFs), three of these cross-sectional parameters are set to fixed values – the interior and exterior shell thicknesses are fixed at 1.75 mm, and the trailing edge reinforcement width is fixed at 1.0

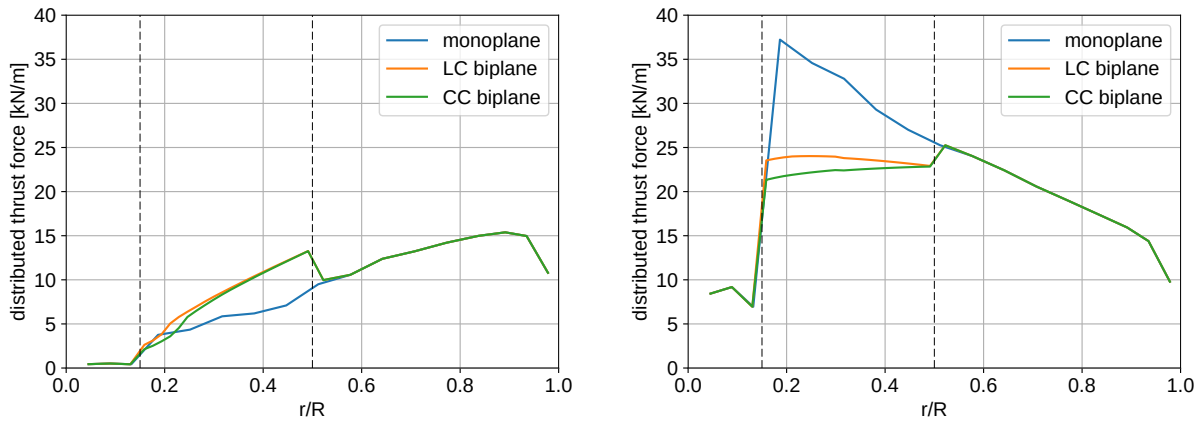

(a) gust loads

(b) parked extreme load

Figure 4.5: Applied aerodynamic loads for the three blades. The biplane blades have higher gust loads than the monoplane blade, but reduced parked extreme loads.

m. These simplifications are justifiable – for blades with publicly available laminate plans, the shell thickness is often constant outside of the root area [14, 17, 84, 85]. In addition, the trailing edge reinforcement is most easily manufactured if it is built as a fixed-width stack of material along the blade span. The start and end locations of the spar cap are also computed from a simple rule, rather than being exposed to the optimizer. For each airfoil, the spar cap location is centered around the airfoil's max thickness location, and a fixed spar cap width of 1.5 m is used ($x_{\text{sc,end}} - x_{\text{sc,xstart}} = 1.5\,\text{m}$). As with the the previous simplifications, this fixed spar cap width reduces complexity in the manufacturing process. The shear web parameters are also fixed, with a 3 mm laminate thickness and a 80 mm core thickness. Thus, only two degrees of freedom are variable for each cross section – the spar cap thickness and the trailing edge reinforcement thickness. These are summarized in Table 4.2.

For both monoplane and biplane blades, the cross sections and thus beam properties are defined at 20 stations along the $0.85R$ length of blade which is modeled. This number was chosen to adequately capture variations in the spanwise structural properties and material thickness distributions, while maintaining a reasonable computation time. For the biplane blades, it is assumed that the cross sections in the both branches of the biplane blade are identical. Based on this parameterization and discretization, for each of the optimizations, there are a total of 40 DOFs, corresponding to 2 DOFs at each of 20 cross sections.

Table 4.2: Fixed and variable cross section parameters. For each cross section, only the spar cap thickness and trailing edge reinforcement thickness are exposed to the optimizer. The spar cap start and end locations are derived, using a fixed-width 1.5 m spar cap centered around each airfoil's location of maximum thickness.

variable	value
trailing edge reinforcement thickness, t_{ter}	**variable**
spar cap thickness, t_{sc}	**variable**
exterior shell thickness, $t_{\text{shell, ext}}$	1.75 mm
interior shell thickness, $t_{\text{shell, int}}$	1.75 mm
spar cap start location, $x_{\text{sc, start}}$	derived
spar cap end location, $x_{\text{sc, start}}$	derived
shear web laminate thickness, $t_{\text{sw, lam}}$	3 mm
shear web core thickness, $t_{\text{sw, core}}$	80 mm
trailing edge reinforcement width, w_{ter}	1 m

In some approaches [75], the number of DOFs is further reduced by parameterizing the *distributions* of cross sectional parameters along the blade span with, for example, a spline. However, such a parameterization assumes that the optimal spanwise distribution of material thicknesses can be adequately captured with said parameterization. If this is not true, then there is a risk of finding a solution which is not optimal. No such parameterization of spanwise cross sectional parameters is made here – this comes at the cost of computational time, but allows the optimization routine the most flexibility in finding optimal solutions. As will be shown later, the optimal distributions of materials in biplane blades are neither intuitive nor smooth.

4.3.3 Optimization algorithm, initial conditions

The gradient-based sequential least squares linear programming (SLSQP) algorithm was selected for this optimization. The implementation itself is that provided with SciPy [86], which uses an algorithm modeled after the original that of Kraft [87]. Forward differencing is used to numerically compute the gradients and was found to give adequate convergence for all blades optimized here. While such a gradient-based approach is only capable of finding the local optima, a multistart approach is used to provide a higher chance of finding the global optima.

4.4 Results - Optimized 100 meter blades

The framework described above was applied to optimize the internal structure of the monoplane, CC biplane, and LC biplane blades to meet the design constraints while minimizing blade mass. All cases were shown to converge to physically realistic solutions within 120 iterations. The blade properties for these optimized blades are shown in Table 4.3.

First, consider the optimized monoplane blade, which is used as a reference for comparison throughout.This blade has a mass of 61.1 t, making it considerably lighter than the SNL 100 blade it is modeled off of, which has a mass of 114 t. A number of factors contribute to this discrepancy. In the SNL 100 blade, the inboard 15% of the blade accounts for 20% of the blade mass, and this segment of the blade is not modeled in the present analysis. Additionally, foam core material in the SNL 100 blade accounts for 13.3% of the blade mass while additional resin and gelcoat account for about 7% of the blade mass; neither of these components are modeled here. In total, these non-modeled elements account for about 40% of blade mass. Neglecting those components, the mass of the SNL 100 blade is 68.4 t, which is much closer to the mass of the optimized monoplane blade here. It should also be noted that no systematic optimization approach was taken in the design of the SNL 100 blade and it is likely that the blade is overdesigned.

Compared to the optimized monoplane blade, *significant* mass reductions are shown for the CC and LC biplanes. The CC biplane and LC biplane are 34.4 t and 32.6 t respectively. This represents relative reductions of 43.7% and 46.2% relative to the 61.1 t monoplane blade. It is worth noting that despite the increased loads, the LC blade has lower mass than the CC blade, although not by much. The total blade masses are broken down by component in Figure 4.10. The most drastic difference between the blades is that the biplane blades have significantly less spar cap mass than the monoplane blade. Both biplane blades have a bit more mass in the shell layers, as well as in the shear webs. This is expected, as the total area of blade surface which must be covered with shell layer is increased for the biplane blades. Similarly, in the biplane region there are four shear webs instead of two as there are in the monoplane blade. The mass of the trailing edge reinforcement is also reduced on the

Table 4.3: Summary of blade properties and constraints for optimized 100 m blades.

blade	m_{total} [t]	m_{inboard} [t]	m_{outboard} [t]	δ_{tip} [m]	$\max \epsilon_{\text{ult}}$ [μstrain]	$\max D_{\text{fat}}$ [-]	ω_0 [Hz]	LF_B [-]
monoplane	61.1	38.0	23.1	7.0	3,950	1.0	3.40	-
LC biplane	32.6	17.1	15.5	7.0	10,000	1.0	3.70	1.45
CC biplane	34.2	18.0	16.2	7.0	10,000	1.0	3.52	1.42

biplanes, but this makes up only a small percentage of the total blade mass.

In this section, the mechanisms contributing to these mass reductions are examined in detail.

4.4.1 Reduced spar cap thickness

The optimized spar cap thickness distributions along the blade span are shown in Figure 4.6a. In the monoplane, spar cap thickness is used to provide flapwise structural stiffness to meet the tip deflection constraint – it can be seen in Figure 4.9b that the ultimate flapwise strain constraint is not active for the monoplane blade. Compared to the monoplane, the optimized biplane blades generally use much thinner spar caps. In the biplane inboard region, very little spar cap is used at all, and it can be seen that that distribution of spar cap thickness within the biplane branches is non-monotonic. In the monoplane outboard of the biplane blades, significantly less spar cap is required, even though the blades are identical in chord and airfoil shape in this region. The reasons for this drastic spar cap thickness reduction are further discussed in this section.

Previous work has shown that biplane blades have significantly improved flapwise structural efficiency when compared to monoplane blades [42]. In that work, structural efficiency was measured in a global sense by taking the quotient of the tip deflection and blade mass. The mechanisms behind this improved structural efficiency was not discussed in detail, however.

There are two primary contributing factors to the improved structural efficiency of biplane blades. First, the resistance to tip deflection of the biplane region is improved. In [42], it was

shown that for the same mass, simplified biplane blades had reduced displacement at the end of the biplane region midboard compared to a monoplane blade. The second contributing factor relates to the deflection angle of the blade at the joint. In biplanes, the deflection angle at the joint is much smaller than that at the same location in a monoplane blade. In a sense, this "resets" the tip deflection of the blade as the monoplane outboard starts at an angle which is nearly perpendicular to the hub plane. The impact of the local deflection angle θ at r on the tip deflection can be computed simply as

$$\Delta y_{\text{tip}} = \tan\theta(r) \cdot (R - r) \tag{4.11}$$

The structurally optimized biplane blades take advantage of both of these mechanisms. The deflected blade shapes and deflection angles are shown in Figure 4.7. All optimized blades have 0.07R deflection at the tip, indicating an active tip deflection constraint in all cases. Despite the biplane region having reduced displacement for the same mass, for both biplane blades, the optimal solutions have increased deflection at the joint location compared to the monoplane. This indicates that significant mass savings are available by allowing the biplane region of the blade to deflect. The weights of the inboard region ($0.15 \leq r/R \leq 0.50$) of the blades for the monoplane, CC biplane, and LC biplane are shown in Table 4.3. The inboard regions of both CC and LC biplane blades are approximately 20 t lighter than that of the monoplane blade.

The deflection angle of the biplane blades at their joint location is also shown to be significantly smaller than that of the monoplane blade (Figure 4.7b). The deflection angle of the monoplane at the joint location ($r/R = 0.5$) is 3.17°, contributing to 2.77 m of tip deflection (from Eq. (4.11)). In contrast, the CC biplane has a much lower deflection angle of 0.997°, contributing to only 0.871 m of tip deflection. The effect of this is that the monoplane outboard of biplane blades are allowed to be more flexible. It can be seen in Figure 4.6a that the optimizer takes advantage of this, reducing the spar cap thickness of the outboard region of the biplane blades significantly when compared to the monoplane blade. This increased flexibility affords significant mass reductions – for the monoplane blade, the outer 50% of

the blade has a mass of 23.1 t. For the CC and LC bipanes, the monoplane segment of the blades has a mass of 16.2 t and 15.5 t, respectively, about a 30% mass reduction.

These reductions in spar cap thickness do come at the expense of margin in the ultimate strains. The ultimate strains (under the parked extreme load case) are shown in Figure 4.9b. It can be seen that the monoplane blade has a maximum ultimate strain of around 3,950 μstrain, whereas, at some inboard locations, the biplane blades experience the maximum allowed ultimate strain of 10,000 μstrain. As the tip deflection constraint in biplanes is much weaker than in monoplanes, spar cap thickness can be reduced to the point of reaching the ultimate strain limit.

As was shown in previous studies on biplane blade structures [42], the moment distributions for biplane blades are very different than those for monoplane blades. This is exemplified in Figure 4.8, which shows the internal flapwise bending moments for the biplane and monoplane blades under the gust loading condition. For monoplanes, the bending moment due to an applied aerodynamic load is monotonic and decreasing in magnitude to zero from root to tip. For biplanes, however, the bending moment distribution is very different. The bending moments in the biplane branches of the blade are much smaller in magnitude than that of the monoplane blade. In addition, the bending moment also changes sign somewhere along the middle of the biplane branches, and there is a location somewhere along the branches where the bending moment is zero.

This bending moment distribution explains the non-monotonic nature of the spar cap thickness distribution in the branches of the biplane blades – spar cap thickness is still needed to satisfy the ultimate strain constraint. The bending moment is largest at the ends of the biplane branches, mandating that spar cap be added to add flapwise stiffness in these locations. Along the middle of the biplane branches, no spar cap is needed, as the bending moment magnitudes here are very low. The fact that the spar cap thickness drops so low in the biplane branches indicates that, for biplanes, tip deflection is extremely insensitive to the flapwise stiffness there. Interestingly, at the innermost station of the biplane blades, the ultimate strain constraint is not active, yet spar cap material was still added at this station; this indicates that the tip deflection is sensitive to the stiffness at the roots of the

two biplane branches.

4.4.2 Reduced trailing edge reinforcement

Trailing edge reinforcement material is typically used to add edgewise stiffness to cross sections to limit fatigue damage. The optimized trailing edge reinforcement thickness distributions along the blade span are shown in Figure 4.6b. The need for trailing edge thickness reinforcement is driven by the fatigue damage constraint, shown in Figure 4.9a. As can be seen, this constraint is active along the monoplane blade up to $r/R = 0.5$. For the LC biplane the fatigue damage constraint is active only to $r/R = 0.25$, and for the CC biplane it is active only to $r/R = 0.35$. This indicates that biplane blades are less driven by fatigue damage than monoplane blades.

It might be thought that the reduced chord length of the branches of the biplane blades would lead to a more active fatigue damage constraint in the biplane blades, since edgewise bending stiffness scales approximately as chord length cubed. The results show otherwise. Compared to the monoplane blade, both CC biplane and LC biplane blades have reduced trailing edge reinforcement thickness, leading to small reductions in blade mass.

The reduced fatigue damage in the optimal biplane blades is due to two factors. The first is that the biplane blades are much lighter overall compared to the monoplane blade. Since fatigue damage due to self-weight is directly related to the blade mass, reducing blade mass significantly reduces fatigue damage. The second reason leading to reduced fatigue damage in biplanes is that the self-weight moments are split in half between the two branches of the biplane blade. This reduces the cyclical stress amplitude by a factor of two. From inspection Eq. (4.7), it can be seen that such a reduction in S leads to the damage D being reduced by a factor of 2^{-b}. For $b = -10$, as is assumed here, this reduction amounts to a 1024 time reduction in damage.

From the results of the optimization, it can be seen that despite the reduction in chord length for biplane blades, edgewise fatigue damage is reduced. Stated in a different way – for a given blade radius, the edgewise fatigue constraint is less active for biplane blades than

for monoplane blades.

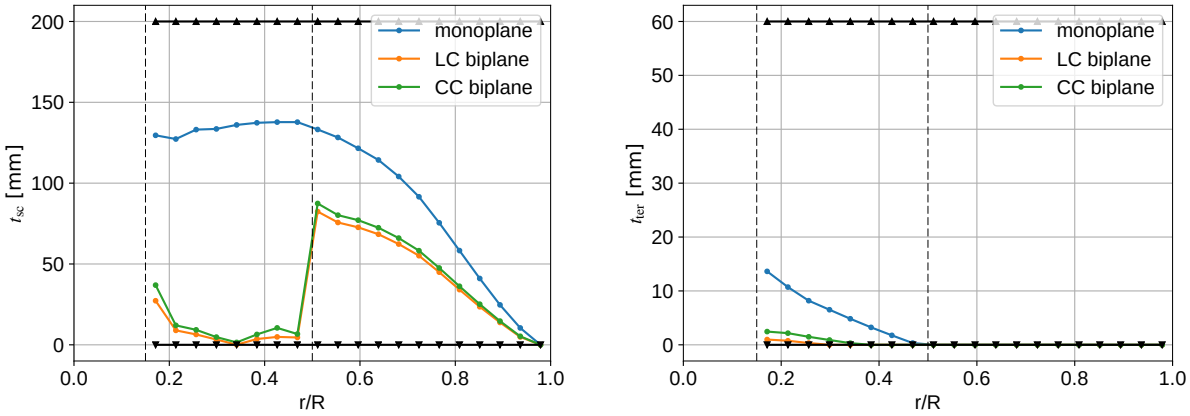

(a) spar cap thickness

(b) trailing edge reinforcement thickness

Figure 4.6: Comparison of internal flapwise bending moment and axial forces for monoplane and CC biplane under a gust aerodynamic load.

4.4.3 Natural frequencies

The natural frequencies for the optimized blades are shown in Table 4.3. The first natural frequency of the optimized monoplane blade was 3.40 Hz, compared to 3.70 Hz for the LC biplane and 3.52 Hz for the CC biplane. The biplane blades have higher first mode natural frequencies, likely due to their reduced masses. From a design perspective, this indicates that the first natural frequency of biplane blades is likely to be adequately separated from the the 3P frequency. It is worth noting that the first vibration modes of the biplane blades correspond to a global edgewise deflection mode, whereas the monoplane blade oscillates first in the flapwise direction.

4.4.4 Beam buckling

The beam buckling load factors for the biplane blades were computed under parked extreme operating condition using the approach described in Section 4.2.3, and are shown in Table 4.3. As can be seen, both biplane blades have beam buckling load factors greater than 1, indicating that beam buckling does not occur in the optimal biplane blades, nor is

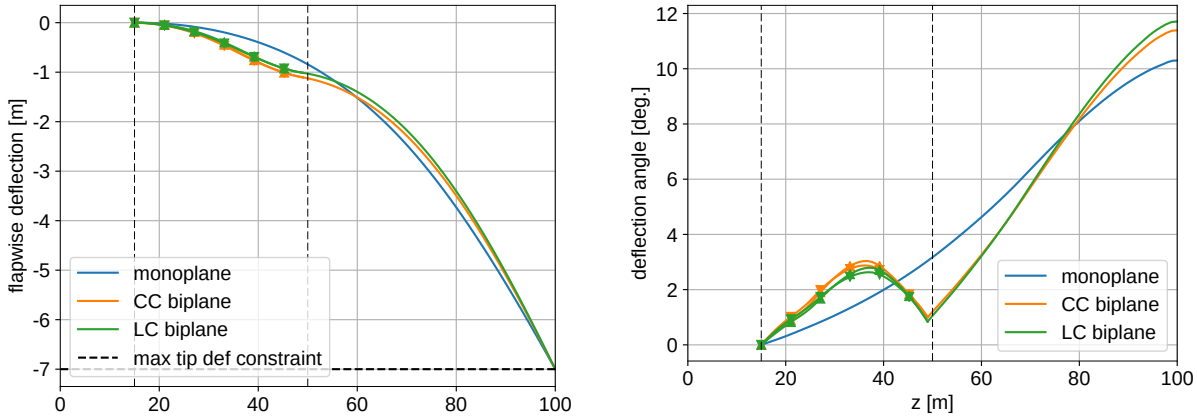

(a) flapwise displacement

(b) deflection angle

Figure 4.7: Displacements and deflection angles for the monoplane and biplane blades under their respective gust loading conditions.

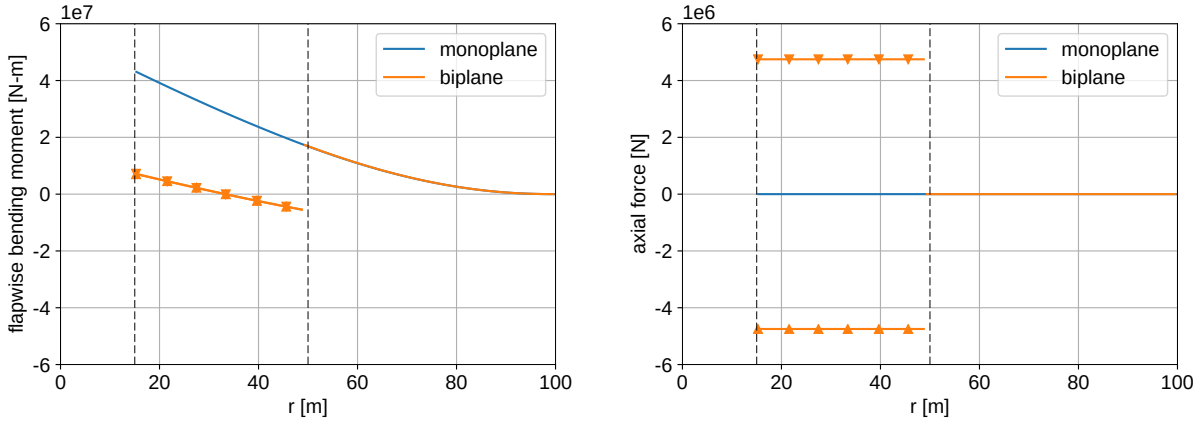

(a) flapwise bending moment

(b) axial force (negative compression)

Figure 4.8: Comparison of internal flapwise bending moment and axial forces for monoplane and CC biplane showing internal forces and moments under a test load. The moments in the biplane branches are significantly reduced when compared to the monoplane blade. Tensile/compressive axial forces, not present in the monoplane blade, are observed in the branches of the biplane blade.

it an active constraint.

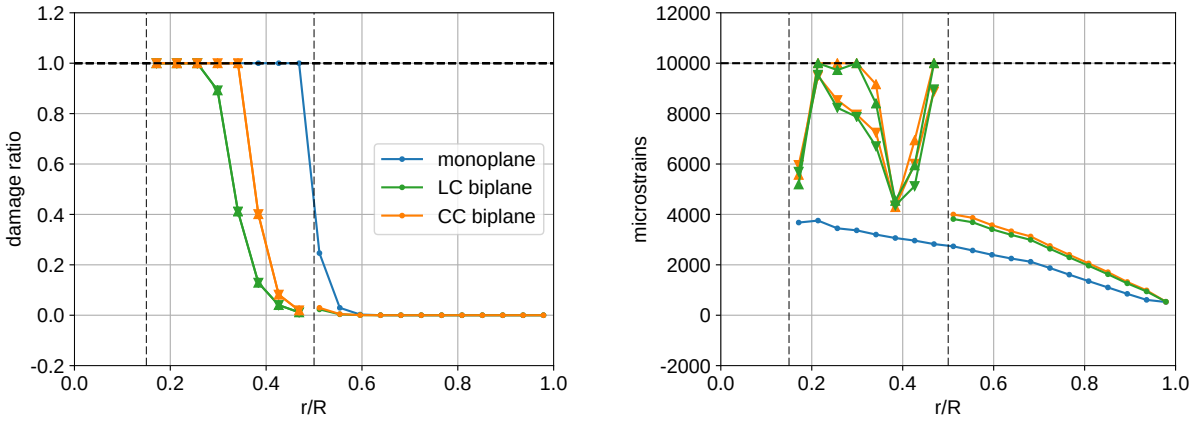

(a) fatigue damage

(b) ultimate strains

Figure 4.9: Spanwise constraints for fatigue damage and ultimate strain. Thick dashed lines show the fatigue damage limit of 1.0 and the ultimate strain limit of 10,000 μstrain.

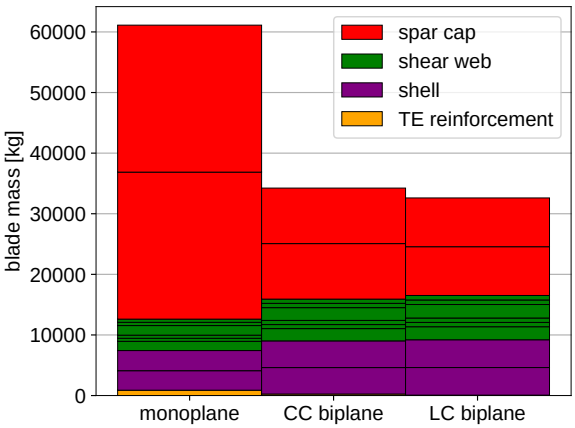

Figure 4.10: Breakdown of total optimized blade masses by component. The majority of mass reductions in the biplanes come from reduced spar cap material. The shell and shear web masses are both increased in the biplanes. Trailing edge reinforcement makes up a very small mass percentage of all blades.

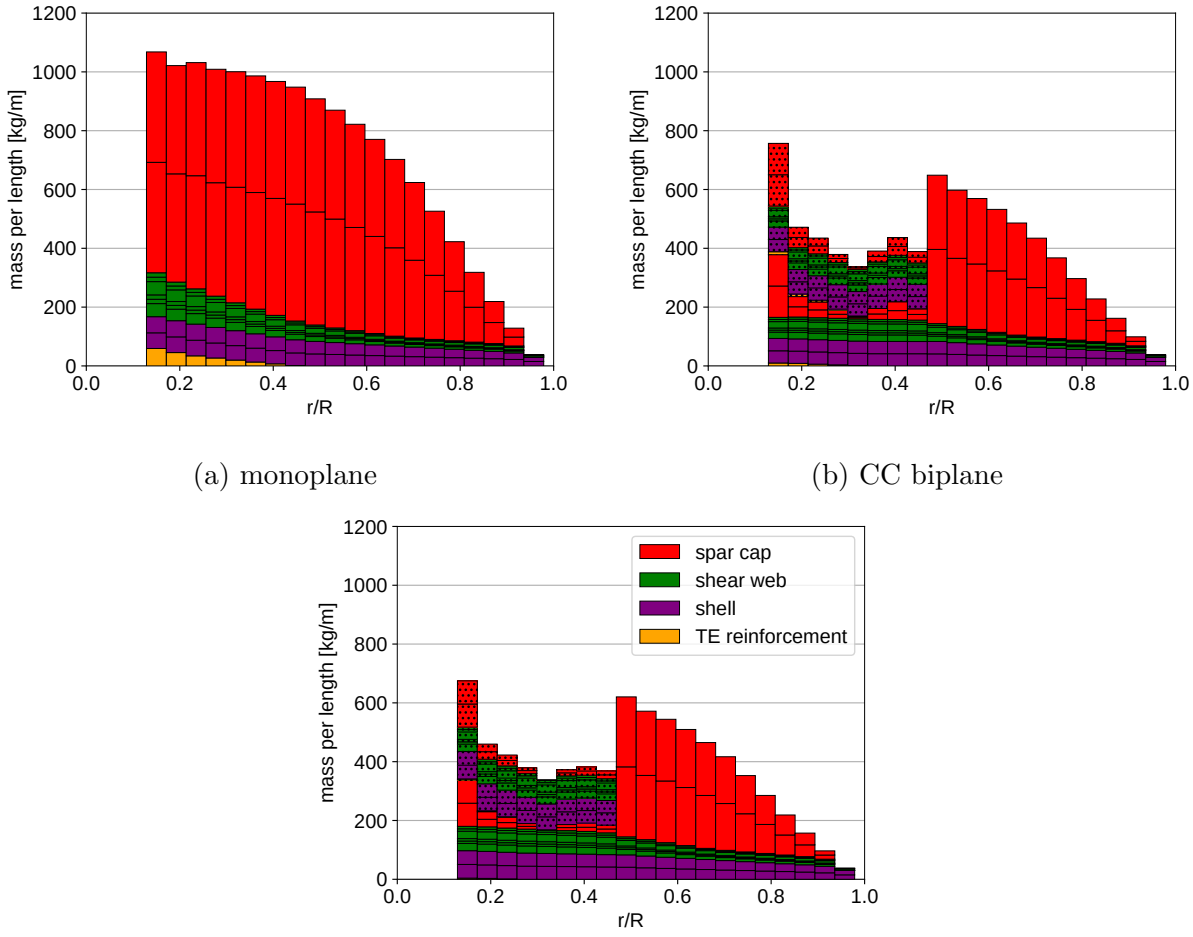

(a) monoplane

(b) CC biplane

(c) LC biplane

Figure 4.11: Distributed blade mass breakdown by cross section and cross section component. For the biplanes, dotted bars represent the mass contribution of the second branch of the biplane.

4.5 Results – trends in blade mass with varying blade length

Using the same optimization framework described above, a parametric sweep was conducted to understand how blade length affects the optimal mass and internal structural design of blades with varying lengths R. The fixed cross section parameters (Table 4.2) and parameter bounds were scaled linearly with radius. The aerodynamic loads were also scaled linearly; this is valid assuming constant tip speed ratio between scaled designs [16]. The tip deflection constraint was held constant at $0.07R$, while the material properties and material constraints were constant.

Analytical scaling laws indicate that for an isometrically upscaled blade operated at constant tip speed ratio, tip deflection and stresses/strains due to aerodynamic forces do not vary. Similarly, geometric deflections due to aerodynamic loads scale with R or, in other words, are non-dimensionally invariant [16]. Bending moments due to self weight, however, scale with R^4. Thus, fatigue damage due to blade self-weight scales linearly with R. Therefore, if the design of the blade is driven by the fatigue damage constraints, then the blade mass will increase greater than cubically with radius.

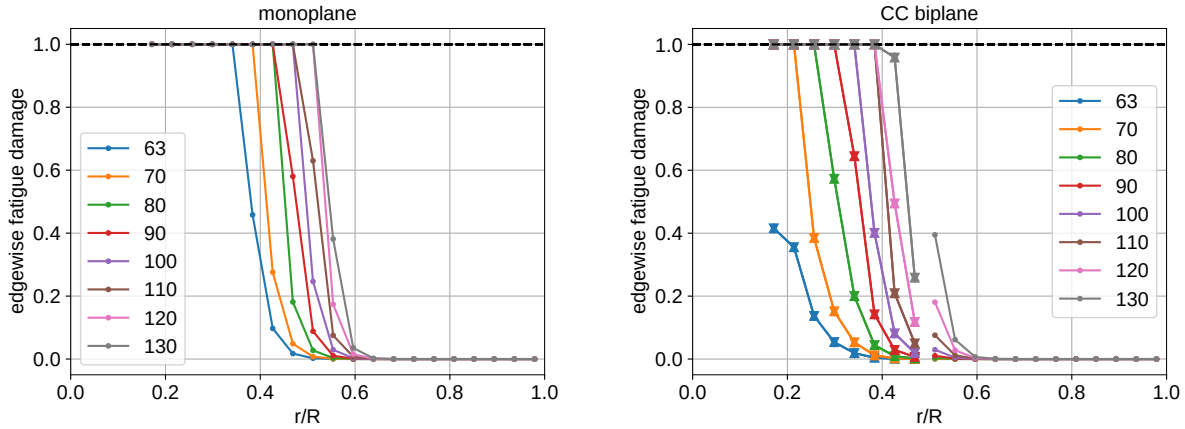

(a) monoplane (b) CC biplane

Figure 4.12: Fatigue damage for monoplane CC biplane blades for varying blade radius, R. The fatigue damage constraint is increasingly active for larger R.

The blade masses for the optimized blades are shown in Figure 4.13. As can be seen, the masses for the LC biplane and CC biplane blades are consistently lower than that of

the optimized monoplane. The results of a power law fit (mass $\propto R^a$) are also shown. For all blades, $a > 3$, as expected based on the discussion in the previous paragraph. However, it can be seen that for the monoplane blades, a is largest at 3.026, but 3.008 and 3.013 for the LC and CC biplane blades, respectively. This is in line with the scaling laws; the mass of monoplane blade, which is heavily driven by edgewise fatigue damage grows fastest with blade size, while the LC and CC biplanes, which are less driven by edgewise fatigue damage, have lower values.

Evidence for this is provided in Figure 4.12, which compares the fatigue damage for the optimal monoplane and CC biplane blades at each R. At smallest blade length of $R = 63\,\text{m}$, the monoplane blade has an active fatigue damage constraint up to $r/R = 0.35$, whereas the CC biplane does not have an active fatigue constraint. As blade length is increased, the fatigue constraint for both monoplane and CC biplane blades becomes active over a longer period of the blade span.

This is reflected in the relative differences between blade masses. The relative mass reductions available from the LC and CC biplane blades grow larger with R – the biplane blades require less mass to meet the edgewise fatigue constraints. This indicates that for larger blades whose design is increasingly driven by self-weight fatigue damage constraints, biplane blades are increasingly favorable.

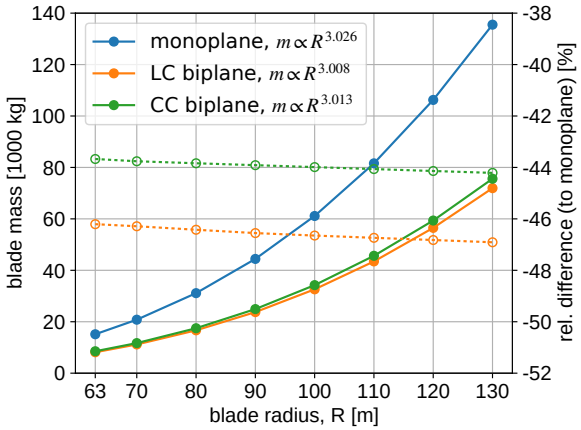

Figure 4.13: Comparison of blade masses for monoplane, CC biplane, and LC biplane blades with varying blade radius.

4.6 Discussion

4.6.1 Other design drivers

The mass reductions shown here are significant, providing strong evidence that biplane wind turbine blades can be built much lighter than conventional blade designs. However, such large mass reductions should be interpreted with some caution. In this work, we considered the design of biplane blades subject to a limited number of constraints – static flapwise tip deflection, ultimate strains, edgewise fatigue due to self-loading, beam buckling, and natural frequency. These constraints are representative of those which drive the design of conventional monoplane blades; however, it is possible that the constraints which drive the mass of *biplane* blades are not fully captured. While every attempt was made to identify the constraints unique to biplanes (e.g., beam buckling), it is possible that not all such constraints have been included.

The dynamic response of biplane blades was not considered here, and it is possible that further constraints can be found through such analysis. For example, through aeroelastic simulations, it may be shown that fatigue damage due to flapwise oscillations is important in biplane blades. If it is shown that this is a design-driving constraint, additional material would need to be added to the spar caps of the biplane blades, offsetting some of the mass reductions shown here. This represents a large step up in fidelity, computational complexity, and effort from the present analyses. The computational time required to execute a single dynamic simulation is orders of magnitude greater than that of the steady evaluation used presently, making the numerical optimization approach here computationally infeasible. In addition, many software packages which exist to analyze the dynamic response of wind turbine blades are not easily generalizable to multi-element blades [88, 89], requiring custom or heavily modified software to be written.

It remains an open question whether the design constraints which may be revealed through dynamic simulations are critical, and, if so, how strongly they impact blade mass. Despite this uncertainty, the results here show very large mass reductions enabled by biplane wind turbine blades. This suggests that even if additional material is required to

design against specific failure modes, biplane blades can still be built significantly lighter than conventional blade designs.

4.6.2 Assumption of a rigid, massless joint

The analyses here assume that the biplane branches are joined at their mid-span location via a rigid and massless joint – this was a simplification for the purposes of modeling. In practicality, a more realistic joint will need to be designed to connect the two branches of the biplane together and to the outboard monoplane branch. This joint will have both mass and flexibility. Segmented conventional (monoplane) blades have been realized commercially using bolted connections to join two blade segments, and similar technology will likely be necessary in the joint connector for biplane blades. Typically, these bolted connections add mass due to the weight of the bolted fasteners themselves, and the weight of the extra material required to reinforce the connection between fasteners and composite blade shell. While the construction of such a joint is likely to add both mass and complexity, it is unlikely that it will come close to offsetting the significant mass reductions for biplane blades shown above. The design of this component should be considered in more detail in future studies.

4.6.3 Opportunities for improvement

Here, a number of simplifications were made in the optimization process in order to provide reasonable computational time and convergence. The blade exterior shape (chord and thickness distributions) was frozen and only the internal structure was optimized. However, given additional computational resources, more optimal designs may be achievable by modifying the blade's exterior shape within the optimization loop. Such an optimization adds considerable complexity.

There is also opportunity for improvement in the cross sectional topology. Conventional cross sectional topologies such as the one used here are optimized for the types of loads experienced by conventional blade designs, with flapwise stiffness provided by uniaxial shear webs and edgewise stiffness provided by uniaxial trailing edge reinforcement. However, it

was shown here that flapwise stiffness contributes little to the tip deflection performance of biplane wind turbine blades. Further improvements may be found by considering alternative cross section topologies and layups in the biplane branches which are optimized for the loads they endure.

4.7 Conclusions

In this work, numerical optimization was applied to design the internal structure of two 100 m biplane wind turbine blades for minimum mass subject to constraints on their tip deflection, ultimate strains, fatigue damage, natural frequencies, and beam buckling load factors. Compared to a monoplane which was optimized subject to the same constraints, it was shown that biplane blades could be designed as much as 46.2% lighter than monoplane blades.

The reason for this large mass reduction is that biplane blades are significantly more mass-efficient in preventing flapwise tip deflection. This allows for considerable material to be removed from the spar caps of the biplane blades while still meeting the tip deflection constraint; however, material can only be reduced up to the point where constraints on ultimate strain become active. Fortunately, due to the reduced chord length on biplane blades, the extreme loads which drive ultimate strain are reduced. In addition to mass reductions in the biplane region of the blade, the improved resistance to flapwise tip deflection allows for mass reductions of approximately 24% in the outboard monoplane segment of the biplane blades. Through a parametric sweep, it was shown that the reduced fatigue damage of biplane blades leads to increased mass reductions as blade length is increased – biplane blades are increasingly attractive for longer blades.

These mass reductions are significant, and, perhaps due to their significance, should be approached cautiously. A physically realizable joint is likely to add some mass to the blade design, although it seems unlikely that the mass requirements for such a joint would offset such large mass reductions. Additionally, only steady analyses were considered here; aeroelastic simulations of biplane blades may reveal other constraints or design drivers which

require additional mass to design against. Such analyses are considerably more computationally expensive than those here, and will likely require custom software to be developed.

The large mass reductions shown here provide strong evidence that biplane wind turbine blades are an enabling concept for the next generation of lighter, larger, and more cost-effective wind turbine blades. Further analysis with higher fidelity, aeroelastic simulations are likely necessary to understand if any additional constraints must be considered in the design of biplane blades. Given the immense potential for mass reductions shown here, these investigations seem warranted.

CHAPTER 5

Conclusions

The overarching objective of this work was to advance the technology maturity of biplane wind turbine blades through understanding of the aerodynamic performance, and aerodynamic/structural design. This work examined a number of aspects regarding the 2-D aerodynamics, blade aerodynamic design and performance, and optimal multi-disciplinary design of biplane wind turbine blades. The results presented here justify future investigation of biplane wind turbine blades and serious consideration by wind turbine manufacturers. Most significantly, the results show that biplane blades may be built more than $> 45\%$ lighter than conventional monoplane blades and with comparable aerodynamic performance, indicating a potential for significant COE reductions.

In this section, the primary findings and conclusions from each chapter are summarized with a focus on their impact to the overall blade design. The limitations of the present analyses are discussed and, with a focus on "next steps" for further technology maturity advancement, ideas for future work are detailed.

5.1 Impact of present work

In Chapter 2 the lift performance of 2-D biplanes with thick airfoils was examined for inviscid, incompressible flows. Compared to biplanes with thin airfoils, a number of unique lift characteristics were shown. These characteristics result from the interactions of the two airfoil profiles, which are increasingly significant for thicker airfoil thicknesses and smaller gaps. Interactions between the two airfoils result in an acceleration of fluid in the channel between the airfoils, creating an attractive force between the two airfoils and heavily-modified

surface pressure distributions in the "inner" airfoil surfaces. The attractive force leads to increasingly unequal airfoil loading and reducing system lift performance as gaps are decreased or airfoil thickness increased. For staggered biplanes with thick airfoils, an effective system camber was also shown. With regards to the design of biplane wind turbine blades, this provides guidance towards the aerodynamic design of the biplane region. First, in the interest of generating the highest lift coefficient, it is desirable to separate the airfoils as much as possible. Separating the airfoils also results in more even loading on the two airfoils, as the attractive force between the two airfoils is reduced. Unequal loading must be considered in the structural design if the airfoils in a biplane are thick and spaced closely together. Secondly, the modifications to surface pressure indicate that the stall characteristics are likely to be significantly modified in biplanes, and that wind tunnel testing is needed if the biplane sections on blades are designed to operate at angles of attack near stall.

In Chapter 3 the overall aerodynamic design of a biplane turbine blade was considered for the first time. The challenge of maintaining a continuous chord distribution at the blade joint was discussed; this was shown to constrain the maximum rotor power coefficient, C_P, achievable by the biplane turbine blades. Two blades with different prescribed chord distributions were designed using blade element momentum theory. It was shown that these blades had slightly increased ($< 1\%$) rotor power coefficient, C_P, over that of a reference monoplane blade, but that these small increases in C_P are likely be offset by the drag penalty arising from the mid-span blade joint. Generally, these findings indicate that the annual energy production (AEP) of biplane blades is likely to be comparable to those that of monoplane blades. The results showed potential for increased real-world AEP due to the broader C_P curve which results from the increased stall margin of the blades. The quasi-steady aerodynamic loads were also quantified. The impact of the loads remained an open question – the gust loads, which can drive blade tip deflection, were shown to be increased, but the extreme loads, which can drive ultimate strains in the blades and ultimate loads in other turbine components, were shown to be reduced significantly.

In Chapter 4, the aerodynamic loads and blade structural performance of biplane blades were considered together. An optimization was applied to design the internal structure of

biplane blades (and a reference monoplane blade) for minimum mass, subject to a number of design requirements which were imposed as constraints. This approach to minimize the blade mass was taken as a proxy for COE – given the results of Chapter 2 which demonstrated that AEP between biplane blades and conventional monoplane blades is comparable, reduced mass leads directly to reduced COE. *Significant* mass reductions of $> 45\%$ were shown for the biplane blades when compared to the similarly-optimized monoplane blade. These mass reductions are primarily the result of the greatly increased resistance of the biplane blade to tip deflection under flapwise loading. The resistance to tip deflection had been shown previously, but this work was the first to quantify the actual mass reductions. For the same blade length, edgewise fatigue performance was shown to be improved for the biplane blades, indicating that these blades can be built longer before edgewise fatigue starts to become design-driving. These findings strongly indicate that biplane blades can be built significantly cheaper than conventional blades and can enable larger turbine sizes.

5.2 Improved modeling and future work

Considerable progress has been made in understanding the performance and design of biplane wind turbine blades. Still, a number of issues must be addressed if these blades are to be considered viable for commercial application. These issues and the means by which they should be investigated are summarized in this section.

5.2.1 Aeroelastic simulations

Aeroelastic simulations are typically used to provide accurate predictions of blade loads, including the effects and interactions of unsteady aerodynamics, structural dynamics, and control. Most commonly, these aeroelastic simulations couple a multi-body dynamics finite element code to an unsteady blade element momentuem (BEM) code [90]. Such simulations are needed to identify aeroelastic issues unique to biplane blades, as these may drive the blade loads (and thus mass) in ways which were not predicted using the simple, quasi-steady analyses of Chapter 4. However, in order to perform run such simulations, existing software

tools [91, 88, 89, 92] for solving the wind turbine aeroelastic problem would need to be generalized to support the modeling of such multi-element blades.

Aeroelastic analyses will also benefit from higher fidelity computation of cross sectional properties. In the present analyses, cross sectional properties of the beams were simplified, assuming infinite shear and torsional stiffnesses, and no cross-coupling of stiffness terms in the off-diagonal terms of the stiffness matrices. These assumptions were taken to permit use of the mid-fidelity cross sectional PolyCX tool, which was used in optimization and thus needed to be both fast and robust. While these assumptions are approximately valid for the steady calculations performed herein, they are likely of critical importance in assessing the aeroelastic stability. Specifically, the coupling of torsion with bendingand shear stiffnesses are of importance in predicting the flutter response of blades, and must be considered in aeroelastic simulations [93]. A number of finite-element based tools exist for computing the full cross-sectional properties, including shear and torsional stiffnesses, and cross-coupling terms [81, 83]. Instead of the simpler PolyCX tool used here, these higher-fidelity tools should be used in calculating the cross-sectional properties for aeroelastic analyses.

5.2.2 Detailed design of the joints/merging region

In the biplane blade concept, joints are needed inboard and mid-blade to join the branches of the biplane with a monoplane outboard blade segment (Figure 5.1). In the present analyses, the mid-blade joint was approximated as a massless plate, while the inboard joint was not modeled at all. In reality, however, both joints will add mass to the biplane blade designs. The design of the joints was not considered here, but their design is critical to enabling biplane blades. What material should the joints be made of, and how should they be constructed? How much will the joints weigh? These questions should be addressed through detailed design. Similarly, the interface of the blade segments (biplane branch segments, monoplane outboard segment) with the joint pieces will also need to be designed. Current segmented blade technologies use alloy fasteners to interface with the composite materials. The amount of added material required to support these bonding pieces should also be

quantified. Given the large mass reductions, it is unlikely that the mass of these additional pieces will outweigh the mass savings of the biplane blade designs, but their masses should be considered. It is likely that high fidelity structural modeling, discussed in further detail below, will be required to design these pieces.

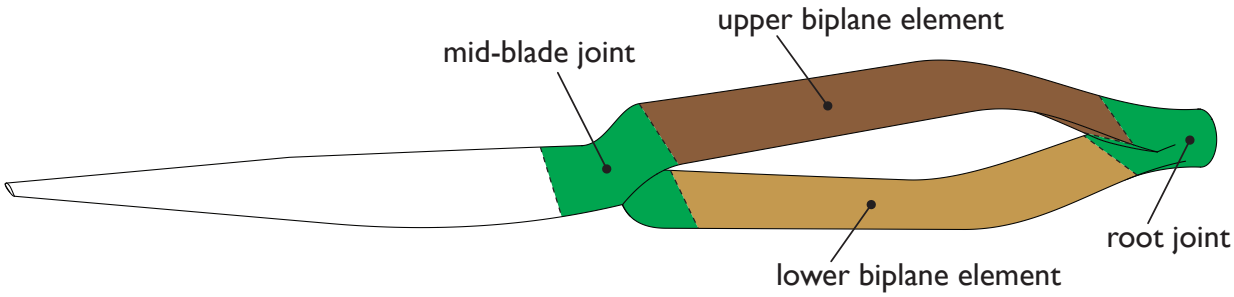

Figure 5.1: Root and mid-blade joints. Figure from [7].

5.2.3 High fidelity structural modeling

In this work, the blade structure was modeled using beam finite elements. This level of fidelity is typically acceptable in the blade design process and in aeroelastic analyses [90]. However, certain structural failure modes including local buckling failure can only be accurately assessed using a 3-D finite element model of the blade, built using either shell or brick elements. Panel buckling, which arises from forces applied to large unsupported panels, was not assessed in the present work; while it is not expected that the biplane blades will experience panel buckling due to their reduced chords, this should still be verified. Spar cap buckling could also be a factor for the branches of the biplane designed in Chapter 4, which very thin spar caps throughout. These failure modes should be assessed using 3-D finite element models – if these failure modes are present, they could be added with the addition of material (and mass) to local regions of the biplane blades.

5.2.4 Improved aerodynamic modeling

In Chapter 3, the aerodynamics of the blades were designed and analyzed using classical BEM theory. BEM is the most commonly used aerodynamic solver in blade design due

to its speed and accuracy when compared to experimental data [94, 95]. However, higher-fidelity methods such as vortex methods, actuator line methods, and geometry-resolved CFD (RANS) are also starting to be considered in the blade design process. These higher-fidelity methods offer improved modeling of certain flow physics. For example, it is known that the flow in the near-root region has a strong spanwise component [96, 97]. The effects of this are not considered in BEM (which assumes locally 2-D flow at all regions of the blade), and can only be captured using geometry-resolved CFD simulations. In addition, the effect of the root vortex, which is created by the coalescence of trailing circulation at the blade roots, is not considered in BEM. There is evidence that if these effects are considered in the design process that blades can be designed with small improvements in rotor power coefficient [21]. Higher-fidelity aerodynamic modeling of the biplane blades should be considered in future studies.

5.2.5 Merging region aerodynamics

The effect of the merging region on the blade performance was estimated in a low-fidelity way in Chapter 3, assuming locally 2-D flow in this region of the blade. However, the true flow physics in this region of the blade is likely to include a significant 3-D aspect, due to the spanwise variation in geometry. Thus, 3-D geometry/surface-resolved CFD simulations should be used to quantify the impact that this region of the blade has on aerodynamic power, and blade loads. These simulations could also be used to optimize the design of this region of the blade to minimize its aerodynamic impact.

5.2.6 Integrated optimization

The blade design approach used in Chapters 2 and 4 can be considered a "sequential" approach, where the blade chord and twist were first designed for maximum aerodynamic performance, and the internal structure was subsequently optimized. This approach was taken to simplify the optimization problem. However, further blade mass reductions, power increases, or blade load reductions could be achieved if the blade chord and twist design

are considered simultaneously. Considering these multiple objectives, care must be taken in formulating the objective function of the optimization (or multi-objective optimization algorithms must be used). The sensitivity of the blade design problem to the choice of objective function is discussed in [75]. It is likely that an "integrated" optimization as described will yield only small improvements over the approach that was used here.

APPENDIX A

Performance of DU 25 biplanes – measurements and computations

A.1 Approach

The 2D aerodynamic performance of biplanes with varying gap and stagger was investigated computationally and experimentally. The biplanes were composed of airfoils using identical DU 91-W2-250 airfoils. The lift and drag of the biplanes were computed using the code MSES. Wind tunnel tests were used to measure the lift performance in stall. The results of the computational analyses were used in the blade design and analyses in Chapter 3.

The following section describes the geometries of the tested biplane configurations and details the computations and experiment.

A.1.1 Tested Airfoil Configurations

In this study a parametric sweep was used to investigate the effects of gap and stagger on biplane aerodynamic performance. To limit the scope of this investigation, the effects of decalage and of unequal chord length were not investigated. Decalage was fixed at 0°. Airfoils of the same size and profile were used in the upper and lower positions of the biplane. The DU 91-W2-250 airfoil, designed specifically for wind turbines and featuring "good maximum L/D and a smooth stall behavior," [29] was chosen for its aerodynamic characteristics and moderate thickness (t/c =25%). The profile of this airfoil is shown in figure A.1.

In total, nine biplane configurations were investigated with gaps of $0.50c$, $0.75c$, and $1.00c$ and staggers of $0.00c$, $0.25c$, and $0.50c$. These ranges for gap and stagger were based on the previously studies of biplane aerodynamics [49, 50, 52, 53] which demonstrated favorable aerodynamic characteristics for positive stagger and large gap. Concerns about the structural performance of excessively large gap or large positive stagger configurations in a wind turbine blade imposed limits on the maxima. The tested configurations are shown in figure A.2.

A.1.2 Computational Approach

The MSES flow solver was used to compute the aerodynamic performance of the biplane configurations. MSES, developed at MIT, is a 2D coupled viscous/inviscid flow solver. The

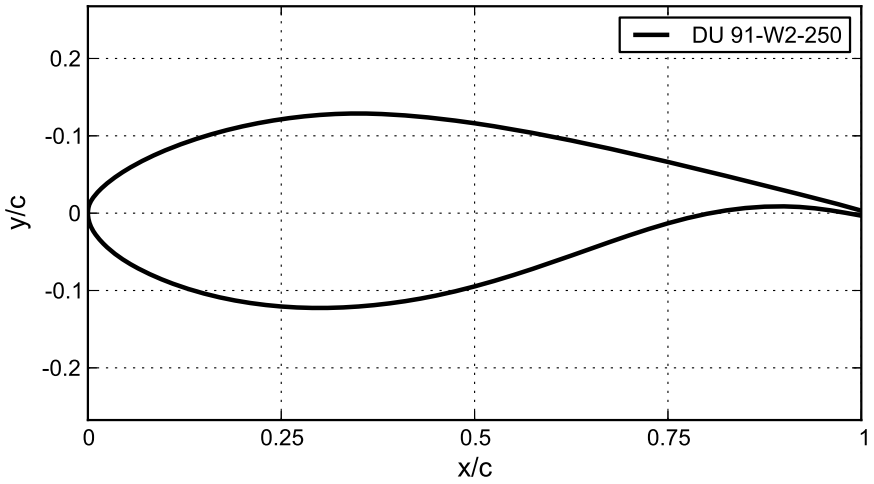

Figure A.1: Profile of the DU 91-W2-250 airfoil ($t/c = 25\%$).

inviscid region is modeled with the Euler equations solved on a streamline grid, while the boundary layers and trailing wakes are described with a two-equation integral formulation [98, 99, 68]. The included grid generation tool MSET was used to generate the initial streamline grids for each configuration.

The biplane airfoil configurations were solved with an "infinite domain," which specifies the velocity and pressure distributions of the far-field boundaries based on the combined potential of a vortex, source, and doublet term. The solver parameters were set to allow for free transition on the pressure and suction sides of both airfoils. The free stream Mach number was fixed for all cases at $M_\infty = 0.07$. The low Mach number allowed usage of the fast subcritical flow solver option MSIS.

The flow field and aerodynamic coefficients of each biplane configurations were computed for an angle of attack from 0° up to just past the point of $C_{L,\max}$ for Reynolds numbers of 500,000. The initial streamline grid for all cases was generated at $\alpha = 0°$. Near $C_{L,\max}$, the angle of attack interval was reduced to 0.1° to more accurately resolve the angle and value of the max lift coefficient.

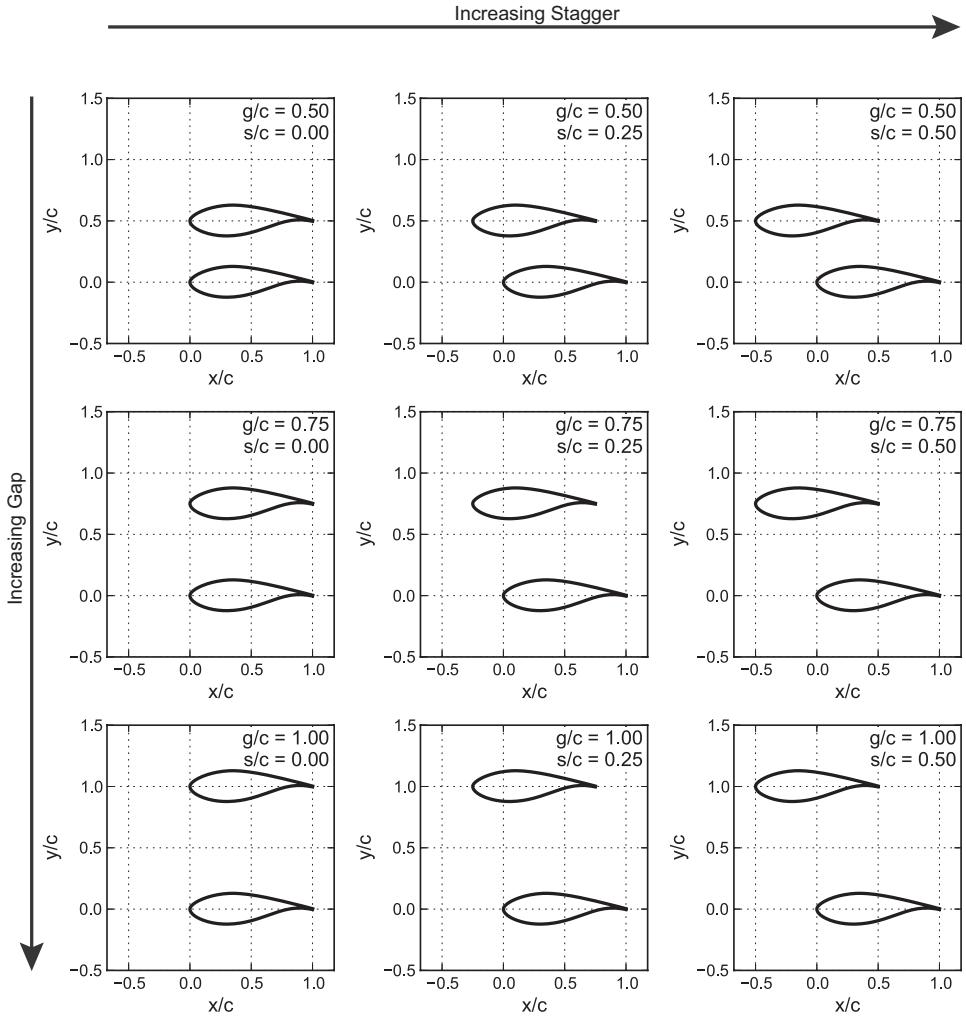

Figure A.2: Nine tested biplane configurations, each with two DU 91-W2-250 airfoils of the same chord length. Gap range is $0.50 < g/c < 1.00$ and stagger $0.00 < s/c < 0.50$.

A.1.3 Wind Tunnel Setup

Force measurements were made in the Lucas Adaptive Wall Wind tunnel at Caltech. The wind tunnel is a closed-return type with a test section 5 ft H × 6 ft W × 25 ft L (1.5 m × 1.8 m × 7.6 m). A ground plane incorporating a motorized turntable reduced height of the test section to 51 inches (1.295 m). The turbulence intensity of this wind tunnel was not characterized.

The airfoils were oriented vertically over the turntable so that the angle of attack could be adjusted by driving the turntable motor. The airfoils were affixed on the bottom to a smooth flat endplate. On the top, a 2 ft × 2 ft × 0.25 in (60.96 cm × 60.96 cm × 0.635 cm) aluminum endplate was used to suppress spanwise flow and to simulate a 2D wind tunnel test by reducing end effects. A 1.5 in (3.81 cm) tall fairing with a 45° beveled edge was used to provide a transition between the tunnel floor and the height of the bottom endplate.

Each CNC-machined ABS plastic airfoil had a 13 in (33.02 cm) chord and 30 in (77.2 cm) span. The chord length was chosen to maximize Reynolds number while giving reasonable solid blockage — 4.5% for the single airfoil tests and 9.0% for the biplane tests. The airfoil surfaces were sanded smooth and finished with a glossy paint. Each airfoil was reinforced with a 1.5 in (3.81 cm) diameter and 1.25 in (3.175 cm) diameter aluminum rods that ran internally through the span. For manufacturing purposes, the trailing edge of the airfoil was fixed to a thickness of 0.08 in (2 mm). The airfoils were positioned behind the the turntable's center of rotation to provide a restoring yaw force in case the yaw motor failed. The experimental setup is shown in figures A.3 and A.4.

Force measurements were taken continuously for -20°$< \alpha <$ 35° by rotating the turntable. The table was rotated slowly (less than 0.96 °/s) to minimize dynamic angle of attack effects. The tunnel wind speed was fixed to give a nominal Reynolds number of 500,000. At higher wind speeds the turntable motor could not provide enough torque to turn through the entire angle of attack range.

The configuration of the wind tunnel did not allow for the airfoil to span the entire height and thus required the use of an upper endplate. The upper endplate did not completely

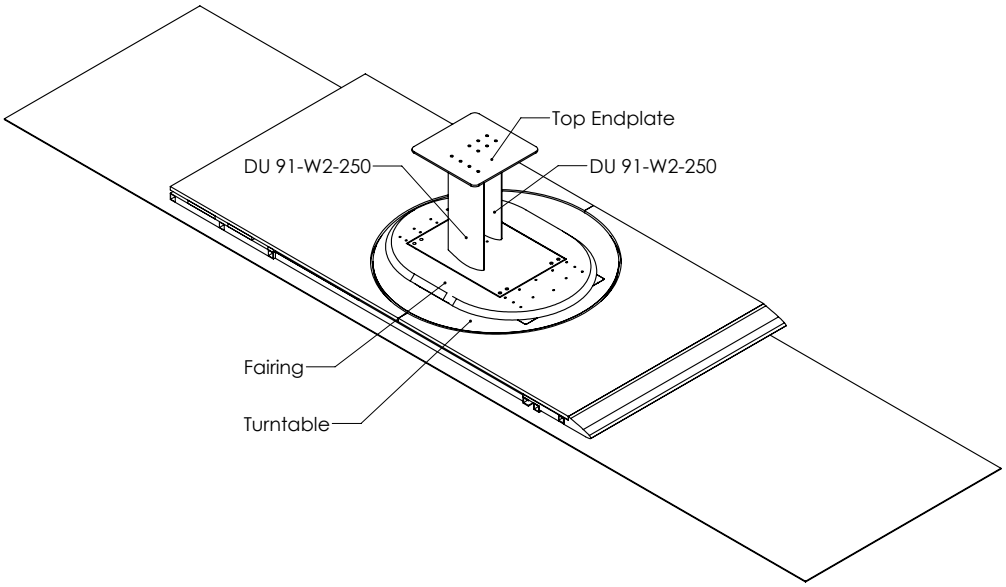

Figure A.3: Experimental setup for wind tunnel, with side walls and ceiling hidden.

remove end effects — tufts, not present during regular testing, revealed spanwise flow after the onset of separation. In addition, the drag contribution of the upper endplate could not be isolated; only lift measurements from the tunnel are presented. Despite these limitations, it is the authors' opinion that the experiment was still capable of revealing trends in the lift and stall performance of biplane configurations and their sensitivities to gap and stagger.

A.1.4 Wind Tunnel Wall Effects

MSES was used to evaluate the effect of the wind tunnel walls on the lift coefficient for each tested configuration. The walls were modeled by applying a solid wall (no flow-through) boundary condition for the upper and lower boundaries of the computational domain. This approach is considered to be valid only before stall. The post-stall wall effects were not investigated in this paper.

A.1.5 Normalization of Force Coefficients

The aerodynamic coefficients for both monoplane and biplane cases are normalized to the chord length of a single airfoil. This is in contrast with previous studies of biplane

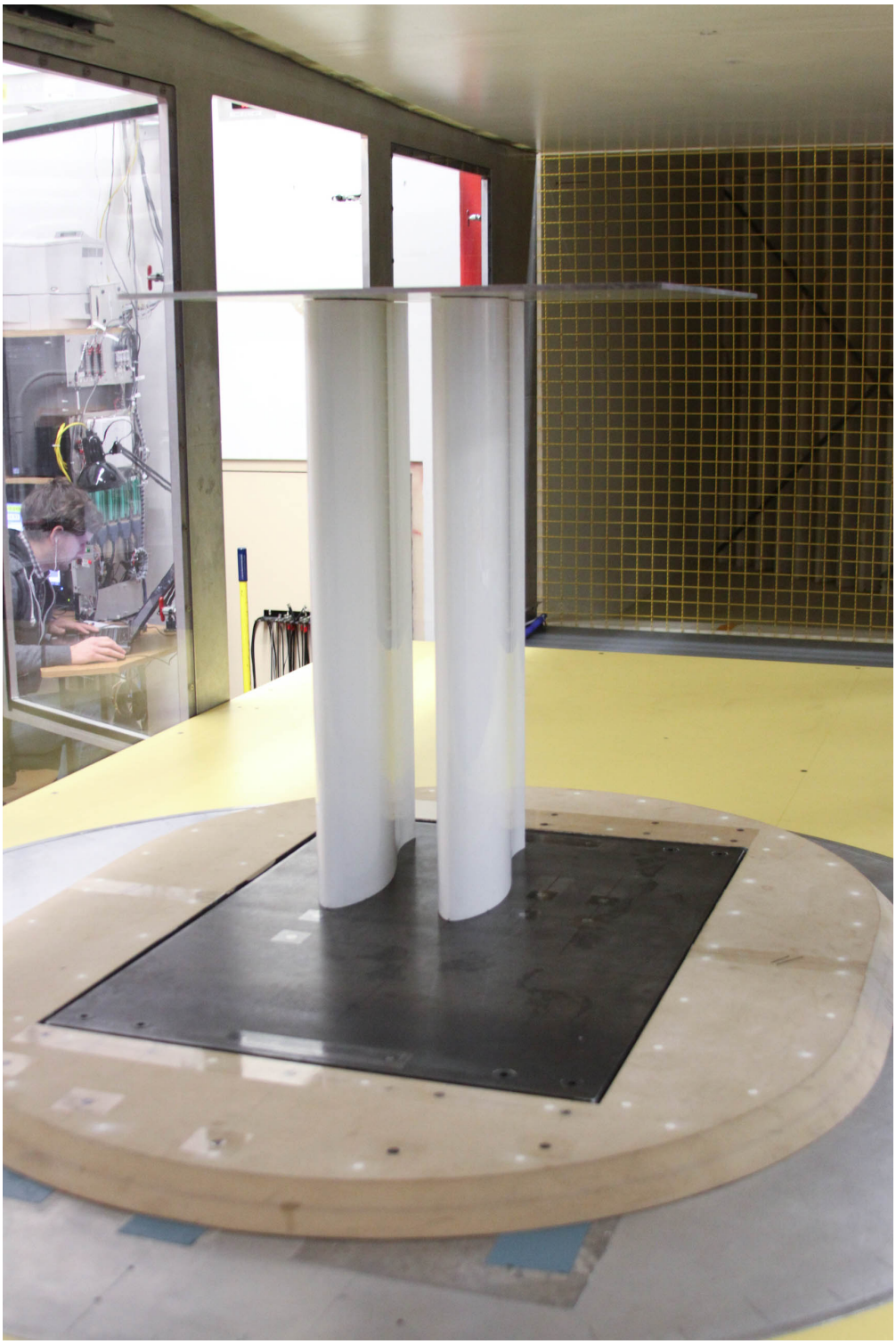

Figure A.4: The test article pictured in the Lucas Adaptive Wall Wind tunnel at Caltech. An endplate on top suppresses spanwise flow. A beveled fairing provides a smooth transition between the tunnel floor and the bottom endplate.

aerodynamics for aircraft, in which it was typical to normalize the force coefficients to the total projected area of both wings, but is in agreement with studies investigating multi-element airfoils [36, 37]. For wind turbine blades, the important design metric is the total amount of lift or drag which is produced from a section of a given length (span). Therefore in the context of wind turbine blades, normalizing the force coefficients for both monoplane and biplane configurations to the chord length of a single airfoil allows a more direct comparison between the two.

A.2 Results

A.2.1 Computed Aerodynamic Performance

The computed lift, drag, and aerodynamic efficiency curves for the biplane configurations are shown grouped by gap distance in figures A.5 to A.7. The $C_{L,\max}$, $(L/D)_{\max}$ and lift curve slope $dC_L/d\alpha$ are tabulated in table A.1. MSES was unable to converge on a solution for the biplane with small gap ($g/c = 0.50$) and no stagger ($s/c = 0.00$).

The computed $C_{L,\max}$ for the biplanes ranged from 2.39 to 2.98, corresponding to a 62.5% to 88.4% increase over the single DU 91-W2-250 airfoil ($C_{L,\max} = 1.54$). The magnitude of $C_{L,\max}$ was shown to increase both with larger gap and positive stagger. For a fixed stagger, larger gaps had higher $C_{L,\max}$. For a fixed gap, increased positive stagger configurations had higher $C_{L,\max}$, although the effect of increasing stagger was reduced at large gaps. The trend showing increasing max lift coefficient with increased gap and stagger agree with past models and studies performed on both finite and infinite aspect ratio biplane configurations [49, 50, 52, 53].

The lift curve slope, $dC_L/d\alpha$, of the tested airfoils was computed using a linear least squares fit for an angle of attack between 1° and 6°. For the biplanes, $dC_L/d\alpha$ was increased 50.4% to 75.0% over the single airfoil. As with the max lift coefficient, $dC_L/d\alpha$ was also shown to be positively correlated with increasing gap and stagger.

The drag of the biplanes also demonstrated sensitivity to relative airfoil positioning. At

low angles of attack, increasing positive stagger was shown to decrease drag. This relationship was inverted as the angle of attack approached $\alpha_{\max}$, above which increasing stagger was correlated with higher drag. In general, increased gap was shown to reduce both the drag and the sensitivity of drag to stagger. The drag of all biplane configurations was always larger than that of the single DU 91-W2-250 airfoil.

The trends in aerodynamic efficiency were similar to those seen in the max lift coefficient — increasing gap and positive stagger were correlated with increasing $(L/D)_{\max}$. Increasing stagger was shown to advance the location of $(L/D)_{\max}$ to a lower angle of attack. Values of $(L/D)_{\max}$ for the biplane configurations ranged from 56.38 (37.5% reduction) to 80.64 (10.7% reduction) compared to the single airfoil which had a computed $(L/D)_{\max}$ of 90.27.

The improved aerodynamic performance with increased gap and stagger is likely due to the reduced interference between the airfoils as their spacing is increased. In order to better understand the effect of interference, also plotted in figures A.5 to A.7 are the lift and drag of the DU 91-W2-250 multiplied by two. This lift and drag would correspond to the lift and drag of a theoretical biplane with the two airfoils infinitely far apart so that each does not interfere with the flow around the other.

It can be seen that all tested biplane configurations had lower $C_{L,\max}$ than the infinitely spaced biplane, demonstrating that interference had a detrimental effect on maximum lift. Generally, increased interference was shown to increase drag. However, interference was shown in some instances to have a "constructive" effect. At low angles of attack, the biplane configurations with high stagger were shown to have higher lift than the infinitely spaced biplane. At high angles of attack, the finitely spaced biplanes with large gap and low stagger were shown to have slightly reduced drag coefficients compared to the infinitely spaced biplane. These results demonstrate that interference in biplanes may under certain circumstances have a positive effect on aerodynamic performance.

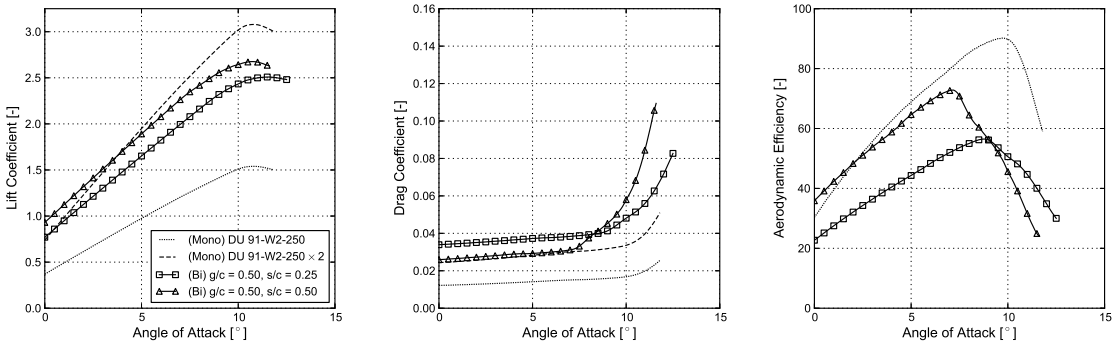

(a) Lift coefficient for small gap.

(b) Drag coefficient for small gap.

(c) Aerodynamic efficiency (L/D) for small gap.

Figure A.5: Computed (MSES) aerodynamic performance of small gap ($g/c = 0.50$) biplane configurations compared to single airfoil.

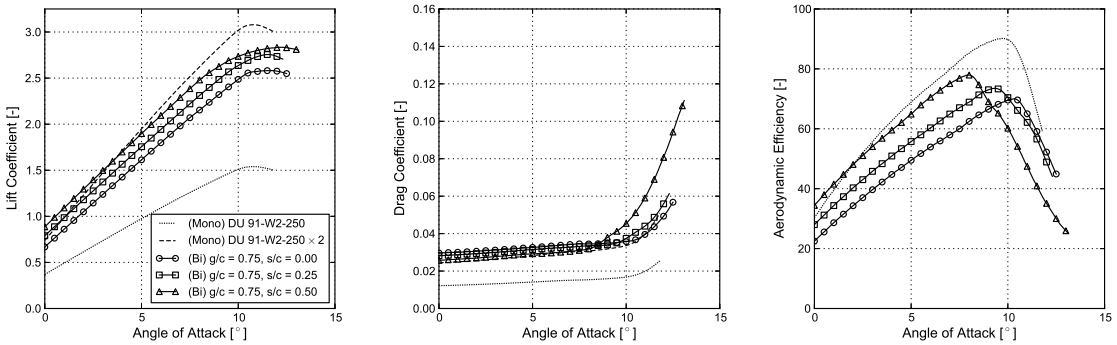

(a) Lift coefficient for medium gap.

(b) Drag coefficient for medium gap.

(c) Aerodynamic efficiency (L/D) for medium gap.

Figure A.6: Computed (MSES) aerodynamic performance of medium gap ($g/c = 0.75$) biplane configurations compared to single airfoil.

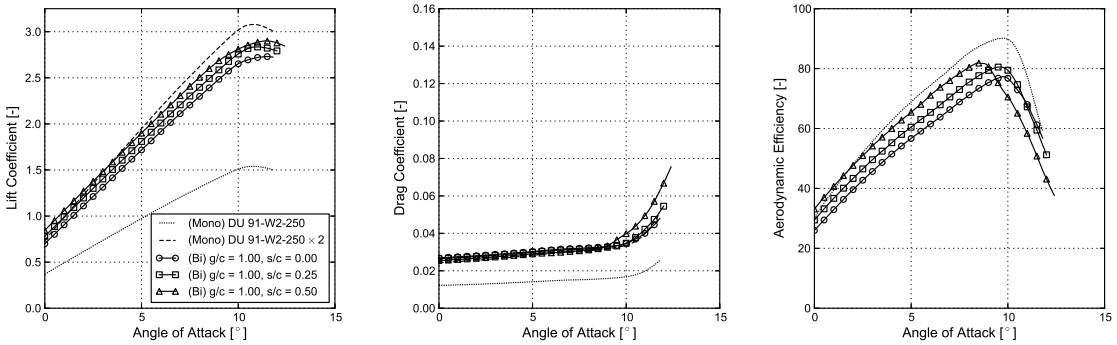

(a) Lift coefficient for large gap.

(b) Drag coefficient for large gap.

(c) Aerodynamic efficiency (L/D) for large gap.

Figure A.7: Computed (MSES) aerodynamic performance of large gap ($g/c = 1.00$) biplane configurations compared to single airfoil.

Table A.1: Computed maximum lift coefficient $C_{L,\max}$, aerodynamic efficiency $(L/D)_{\max}$ and lift curve slope $dC_L/d\alpha$ for nine biplane configurations and single airfoil configuration (Mono). Percent change is shown relative to the single airfoil configuration. The case with gap of $0.50c$ and stagger of $0.00c$ did not converge.

			$C_{L,\max}$		$(L/D)_{\max}$		$dC_L/d\alpha$ [1/°]	
	g/c	s/c	(MSES)	% change	(MSES)	% change	(MSES)	% change
Mono	-	-	1.54	-	90.3	-	0.107	-
Biplane	0.50	0.00	x	x	x	x	x	x
	0.50	0.25	2.50	+ 62.5%	56.4	- 37.5%	0.161	+ 50.4%
	0.50	0.50	2.68	+ 74.0%	72.2	- 20.0%	0.155	+ 44.0%
	0.75	0.00	2.61	+ 69.3%	70.4	- 22.0%	0.174	+ 62.5%
	0.75	0.25	2.76	+ 79.1%	73.6	-18.5%	0.179	+ 67.0%
	0.75	0.50	2.84	+ 84.3%	77.9	- 13.7%	0.173	+ 61.1%
	1.00	0.00	2.77	+ 79.8%	77.6	- 14.0%	0.189	+ 76.1%
	1.00	0.25	2.84	+ 84.5%	80.5	- 10.8%	0.191	+ 78.2%
	1.00	0.50	2.90	+ 88.4%	80.6	- 10.7%	0.188	+ 75.0%

A.2.2 Measured Aerodynamic Performance

The measured lift coefficients for the biplane configurations are shown in figures A.8 to A.10 with $C_{L,\max}$ and $dC_L/d\alpha$ tabulated in table A.2. The lift performance of a single DU 91-W2-250 airfoil was also measured and is superimposed.

The measured lift curves showed the same trends between $C_{L,\max}$ and biplane geometry that were shown with the MSES computations — increasing gap and stagger were shown to increase the maximum lift coefficient. Measured values of $C_{L,\max}$ ranged from 2.39 to 2.98, representing a 45.3% to 80.8% change over the measured $C_{L,\max}$ of the single airfoil. The single airfoil reached $C_{L,\max}$ at $\alpha \approx 13.5°$, while the biplane configurations reached $C_{L,\max}$ at $15.5° \lesssim \alpha \lesssim 18°$. Smaller gap was shown to delay $C_{L,\max}$ to higher angles of attack, indicating that increased interference is a contributing factor to stall delay. This trend is also demonstrated in past studies [50, 52] which showed that for finite-length airfoils, $C_{L,\max}$ occurs later than the monoplane for biplane configurations with positive stagger.

The lift curve slope was also shown to be increased, again showing the trend of increasing $dC_L/d\alpha$ with increased gap and positive stagger. The increases in $dC_L/d\alpha$ (20.0% to 55.6% compared to the DU 91-W2-250 airfoil) were not as significant as shown in the computed results.

The primary goal of the wind tunnel testing was to reveal trends in the stall performance of the biplane configurations. Relative positioning of the two airfoils was shown to have a strong effect on biplane stall performance. At the large gap, the biplane lift curves have roughly the same shape as the single airfoil suggesting that each airfoil performed almost as a single airfoil would. At smaller gaps the shape of the lift curve near $C_{L,\max}$ and in stall deviated significantly from the single airfoil lift curve shape. Generally, the results demonstrated that as gap was decreased, the lift curve shape became more sensitive to changes in stagger. As with the computed results, the increased sensitivity to stagger can be explained by increased interference between the two airfoils.

One particular case showed interesting stall behavior. The small gap, medium stagger biplane ($g/c = 0.50$, $s/c = 0.25$) had extremely flat lift performance across an angle of attack

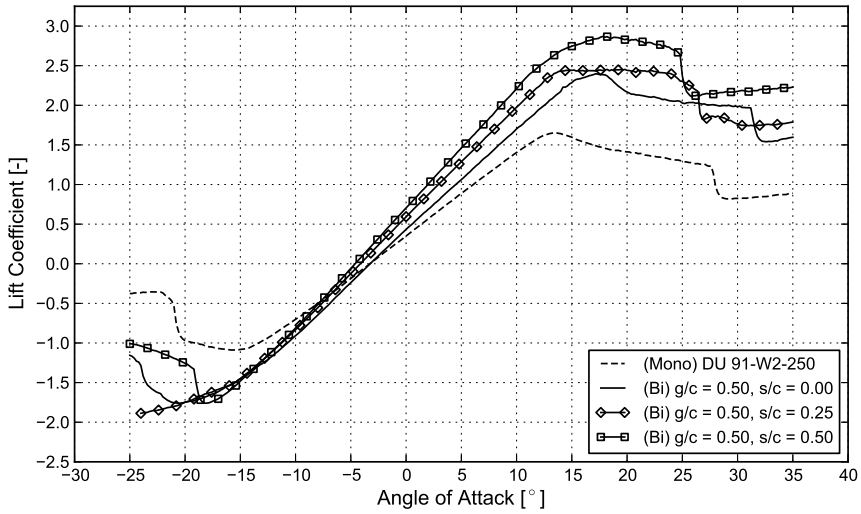

Figure A.8: Measured lift coefficient of small gap ($g/c = 0.50$) biplane configurations compared to single DU 91-W2-250 at $Re = 500{,}000$.

range from $14° \lesssim \alpha \lesssim 24°$. This effect was not demonstrated in the literature and may be unique to the airfoil profile and relative positioning considered.

The measured lift coefficients displayed a sharp drop-off at high angles of attack, corresponding to the point at which flow fully detached from the airfoil. For the single airfoil, this occurred at $\alpha \approx 28°$. For the biplanes, this drop-off occurred between an angle of attack of 25° and 31°. From the data collected, however, it is unclear whether this sharp drop-off in lift was due to flow detachment from the upper airfoil, lower airfoil, or from both simultaneously. For the biplanes, a smaller stagger was shown to delay the detachment to a higher angle of attack. The magnitude of the lift coefficient in deep stall (after flow detachment of at least one airfoil) was shown to be increased with positive stagger.

The measured lift for one biplane configuration ($g/c = 0.75$, $s/c = 0.00$) demonstrated two drop-offs in the lift at high angles of attack, indicating that for this geometric configuration, flow detachment did not occur simultaneously for both airfoils. For the other cases where the second detachment was not observed, it is likely that this was delayed to an angle of attack beyond the range measured in this experiment.

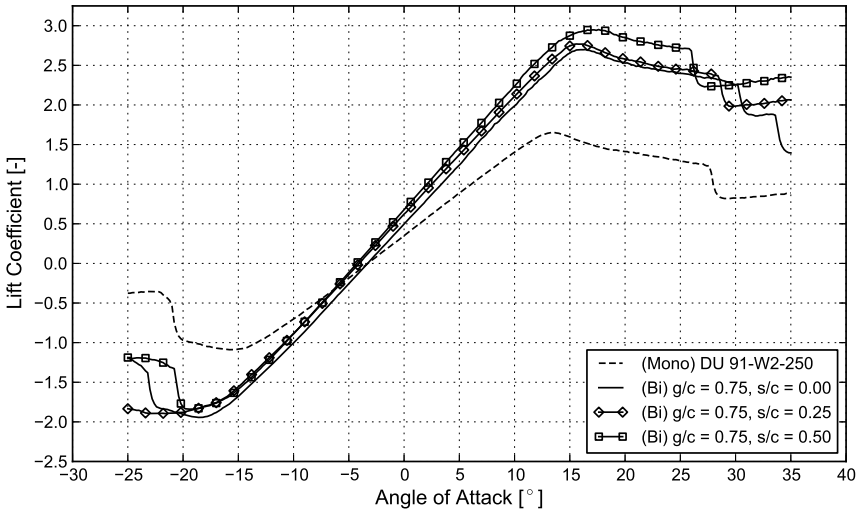

Figure A.9: Measured lift coefficient of medium gap ($g/c = 0.75$) biplane configurations compared to single DU 91-W2-250 at $Re = 500{,}000$.

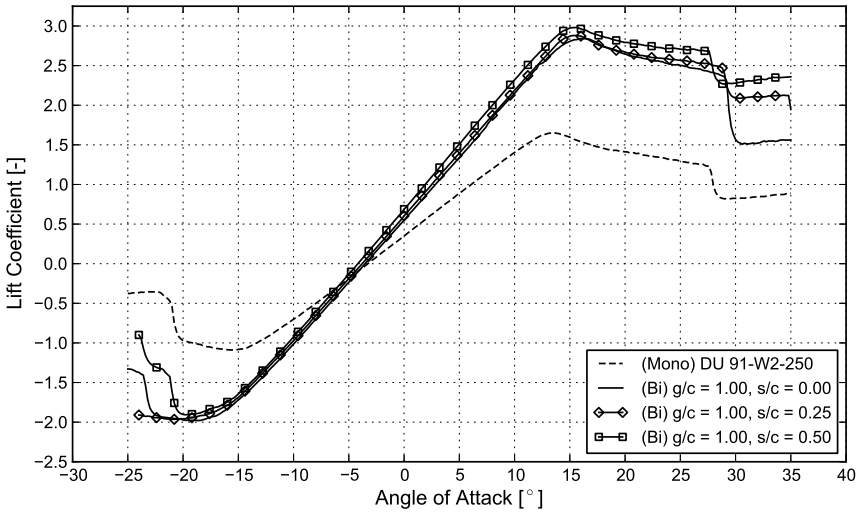

Figure A.10: Measured lift coefficient of large gap ($g/c = 1.00$) biplane configurations compared to single DU 91-W2-250 at $Re = 500{,}000$.

Table A.2: Measured maximum lift coefficient $C_{L,\max}$ and lift curve slope $dC_L/d\alpha$ for nine biplane configurations and single airfoil configuration (Mono). Change is shown relative to the Mono configuration.

			$C_{L,\max}$		$dC_L/d\alpha$ [1/°]	
	g/c	s/c	(WT)	% change	(WT)	% change
Mono	-	-	1.65	-	0.106	-
Biplane	0.50	0.00	2.39	+ 45.3%	0.127	+ 20.0%
	0.50	0.25	2.45	+ 48.5%	0.138	+ 30.7%
	0.50	0.50	2.86	+ 73.6%	0.150	+ 42.6%
	0.75	0.00	2.70	+ 63.8%	0.152	+ 44.1%
	0.75	0.25	2.76	+ 67.9%	0.149	+ 41.3%
	0.75	0.50	2.95	+ 79.0%	0.156	+ 48.2%
	1.00	0.00	2.95	+ 79.0%	0.171	+ 52.3%
	1.00	0.25	2.88	+ 74.7%	0.159	+ 50.4%
	1.00	0.50	2.98	+ 80.8%	0.164	+ 55.6%

A.2.3 Wind Tunnel Wall Effects

The wind tunnel results in this paper are presented uncorrected for wall effects. While established relations [100, 101] exist to correct for wind tunnel wall effects for steady flow single airfoils mounted along a wind tunnel center line, no such corrections have been established for multiple lifting bodes. In addition, the two airfoils of the biplane were in this experiment sometimes mounted off-center from the tunnel center line, further complicating the wall corrections.

The effect of the wind tunnel walls on lift coefficient was evaluated computationally using MSES. The computed lift curves for the "infinite domain" and wall-bounded cases for each tested configuration are compared in table A.3. For the single DU 91-W2-250, the presence of the walls increased $C_{L,\max}$ by 2.5% and delayed its angle of attack by 0.3°. For the biplane airfoils, the presence of the walls increased $C_{L,\max}$ between 3.1% and 9.6%. The location of max lift coefficient, $\alpha_{\max}$, was delayed by 0.60° to 1.33°. No clear trends were observed in the degree to which the walls affected the magnitudes $C_{L,\max}$ for the tested gap and stagger ranges. The lift curve slope was also shown to be increased by wall effects. These increases were more pronounced for the biplane configurations due to the reduced distance between

Table A.3: Modeled effect of wind tunnel walls on maximum lift coefficient, $C_{L,\max}$, location of maximum lift occurs $\alpha_{\max}$, and lift curve slope $dC_L/d\alpha$ for the nine biplane configurations and single airfoil configuration (Mono.)

			$C_{L,\max}$			$\alpha_{\max}$			$dC_L/d\alpha$ [1/°]		
	g/c	s/c	Open	Wall	Change	Open	Wall	$\Delta\alpha_{max}$	Open	Wall	Change
Mono	-	-	1.54	1.58	+ 2.5%	10.8	11.1	0.30°	0.122	0.122	+ 0.7%
Biplane	0.50	0.00	x	x	x	x	x		x	x	x
	0.50	0.25	2.50	2.68	+ 6.9%	11.5	12.1	0.60°	0.176	0.180	+ 2.8%
	0.50	0.50	2.68	2.93	+ 9.6%	10.7	11.7	1.00°	0.193	0.198	+ 2.9%
	0.75	0.00	2.58	2.73	+ 5.9%	11.6	11.9	0.34°	0.190	0.193	+ 1.8%
	0.75	0.25	2.76	2.92	+ 6.1%	11.5	12.3	0.83°	0.193	0.197	+ 1.8%
	0.75	0.50	2.83	3.05	+ 7.6%	12.2	13.0	0.80°	0.203	0.206	+ 1.5%
	1.00	0.00	2.73	2.85	+ 4.3%	11.5	11.8	0.35°	0.204	0.207	+ 1.4%
	1.00	0.25	2.84	2.92	+ 3.1%	11.0	12.3	1.33°	0.206	0.197	− 4.4%
	1.00	0.50	2.90	3.08	+ 6.4%	11.4	12.3	0.90°	0.212	0.211	− 0.4%

wall and airfoils. While the magnitudes of $C_{L,\max}$ and its location were shown to be affected by the presence of wind tunnel walls, the general trends in lift - that increased gap and stagger correspond to increased $C_{L,\max}$ - are the same whether or not the wind tunnel walls are modeled. While wall effects likely affected the magnitudes of the measured lift values, the trends demonstrated between gap, stagger, and aerodynamic performance are unlikely to affected.

A.2.4 Comparison of Computed and Measured Results

Good agreement was shown between the computed and measured results, with key differences between the two tabulated in table A.4. Less than than 7% in $C_{L,\max}$ was shown between the MSES and wind tunnel results. However, there are some discrepancies between the two data sets. In all cases, the lift curve slope in the linear region is higher for the computed results than for the measured results. The MSES computed lift curves also predict $C_{L,\max}$ to occur at a lower angle of attack than the measured results. At small gaps, the measured lift curve slopes of the biplane tests demonstrated a sensitivity to stagger that was not observed in the computed results.

Table A.4: Comparison of measured (WT) and computed (MSES) values for $C_{L,\max}$ and $dC_L/d\alpha$.

			$C_{L,\max}$			$dC_L/d\alpha$ [1/°]		
	g/c	s/c	(WT)	(MSES)	% difference	(WT)	(MSES)	% difference
Mono	-	-	1.65	1.54	6.7%	0.106	0.107	1.6%
Biplane	0.50	0.00	2.39	x	x	0.127	x	x
	0.50	0.25	2.45	2.50	2.3%	0.138	0.161	15.6%
	0.50	0.50	2.86	2.68	6.4%	0.150	0.155	2.7%
	0.75	0.00	2.70	2.61	3.4%	0.152	0.174	13.7%
	0.75	0.25	2.76	2.76	0.2%	0.149	0.179	18.3%
	0.75	0.50	2.95	2.84	3.7%	0.156	0.173	10.0%
	1.00	0.00	2.95	2.77	6.2%	0.161	0.189	16.1%
	1.00	0.25	2.88	2.84	1.2%	0.159	0.191	18.5%
	1.00	0.50	2.98	2.90	2.5%	0.164	0.188	13.3%

A.3 Conclusion

A.3.1 Summary of Results

At a Reynolds number of 500,000, the tested biplane configurations with two 25% DU 91-W2-250 airfoils were shown to have a significantly higher $C_{L,\max}$ than an individual DU 91-W2-250. Aerodynamic performance was shown to be highly sensitive to both gap and stagger. Computational results showed that the lift curve slope $dC_L/d\alpha$ was increased as much as 75.0% over the single airfoil. Compared to the single airfoil configuration, the biplane configurations demonstrated a reduction in $(L/D)_{\max}$ of 10.7% to 37.5%.

It was found that both $C_{L,\max}$ and $(L/D)_{\max}$ were increased with larger gap and positive stagger. The occurrence of $C_{L,\max}$ was found to be delayed for smaller gap configurations. Wind tunnel measurements showed that lift in deep stall was increased with larger positive stagger. These results generally confirm the results of past experimental studies [52, 50] which were which were conducted for thin, finite-span airfoils ($t/c = 11.7\%$) at a lower Reynolds numbers of 150,000.

Generally, increased interference between the two airfoils was shown to reduce aerody-

namic performance. However, small increases in lift and reductions in drag were observed at both high and low angles of attack, suggesting that interference may in some cases increase performance.

The shape of the lift curve in stall was shown to be significantly affected by biplane geometry. The small gap medium stagger configuration ($g/c = 0.50$, $s/c = 0.25$) demonstrated flat lift performance for $14^\circ \lesssim \alpha \lesssim 24^\circ$ indicating that biplane stall performance is strongly affected by the positioning of the airfoils and may be tuned by careful selection of biplane geometric parameters.

A.3.2 Future Work

In this work only gap and stagger were varied, while the decalage, airfoil profiles, and chord lengths all remained fixed. More optimal aerodynamic performance may be achieved by varying the other geometric parameters and also by altering the shape of the airfoils themselves. However, such optimization would need to be constrained so that the structural benefits of the biplane are preserved.

Lift and drag were in this effort examined only in a global sense. Further work would examine the local aerodynamic performance of each airfoil, and the underlying flow phenomena that lead to the observed aerodynamic performance. The stall of each airfoil should be studied in more detail. Wind tunnel testing revealed trends in stall with varying gap and stagger. However, the wind tunnel setup was not ideal for the measurement of 2D aerodynamic performance, and future work seeking to accurately measure quantitative airfoil performance should use a 2D specific wind tunnel which is capable of accurately measuring drag, has reduced wall effects, and can reach higher Reynolds numbers. Lastly, it should be noted that 2D aerodynamic performance is only a predictor of how these airfoils would perform on a rotor. On a moving wind turbine blade, rotational effects typically delay the onset of stall, especially in the inboard region of the blade. The relative 2D performance of tested airfoil configurations may be used to guide the design of wind turbine blades employing biplane airfoils. However, 3D aerodynamic studies of biplanes on a rotor are needed to

explore the flow around biplane airfoils in a rotating system.

APPENDIX B

DYMORE simplification sensitivity studies

This section summarizes studies related to the beam structural models used to assess the blade structural metrics used in Chapter 4.

B.1 Effect of neglecting off-diagonal stiffness terms

In Chapter 4, it was assumed that the off-diagonal terms in the six-by-six stiffness matrices for Timoshenko beams were all zero and that the off-diagonal elements contributed little to the overall steady-state structural response to typical aerodynamic loads. The off-diagonal terms are related to coupling between stiffnesses and deflections in different directions (e.g, flapwise bending/torsion coupling). The effect of neglecting the off-diagonal stiffness terms is investigated in this section by comparing the deflections and internal forces/moments on blades which use the full six-by-six stiffness matrix and those which use a "diagonal" one in which the off-diagonal elements have all been set to zero.

The Sandia SNL 100-00 blade is used as the reference for this study. The full six-by-six stiffness properties were computed using the software package VABS [82]; the data is provided in the thesis of Roth-Johnson [7]. The stiffness matrices are compared in Figure B.1. For the purposes of this study, a typical operating aerodynamic load was applied. The flapwise distributed force is shown in Figure B.2.

The internal beam forces and moments are compared in Figure B.3, where, as expected, it can be seen that there is no difference between the "full" and "diagonal" stiffness matrix sets. The deflections and rotations are compared in Figure B.4. Some differences are seen here, with the largest being in the flapwise deflection; the "diagonal" blade has approximately 4% less tip deflection than the "full" blade. This error is acceptable for the relative comparisons used in the optimization procedure.

The first-mode eigenvalue frequencies were also computed for both "full" and "diagonal" blades, with the "diagonal" blade showing a small (1.2%) increase in frequency as compared to the "full" blade.

Based on these small differences for the quantities of interest used in the optimization

(flapwise tip deflection, first-mode eigenvalue frequency, the approximation of using diagonalized stiffness matrices is considered valid.

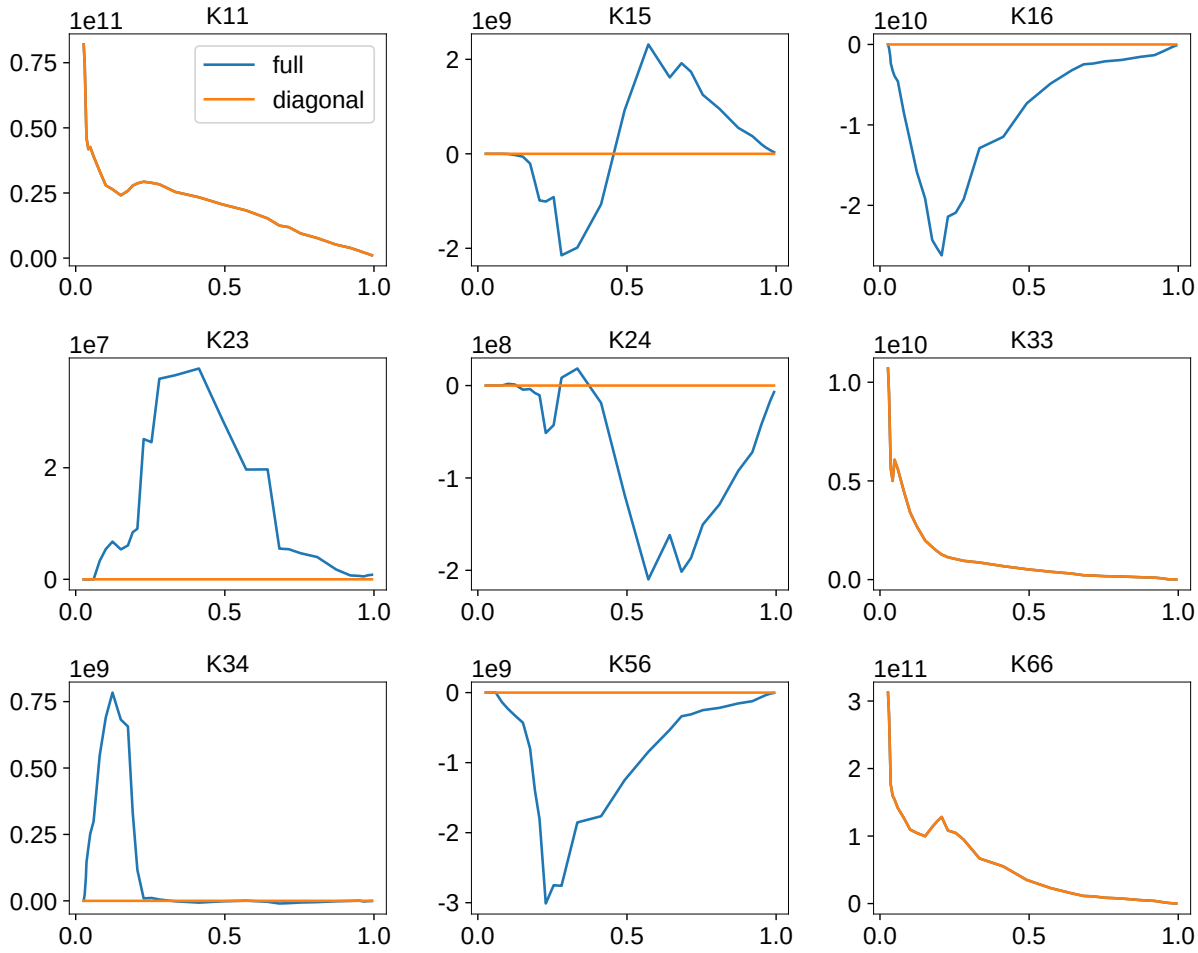

Figure B.1: Stiffness matrix terms for the SNL 100-00 blade with all terms ("full") and with only diagonal terms ("diagonal"). All terms not shown have zero values in both "full" and "diagonal" stiffness properties. The rows/column indices of the stiffness matrix are 1 – axial stiffness, 2 – bending stiffness 1, 3/4 – bending stiffness, 5/6 – shear stiffness.

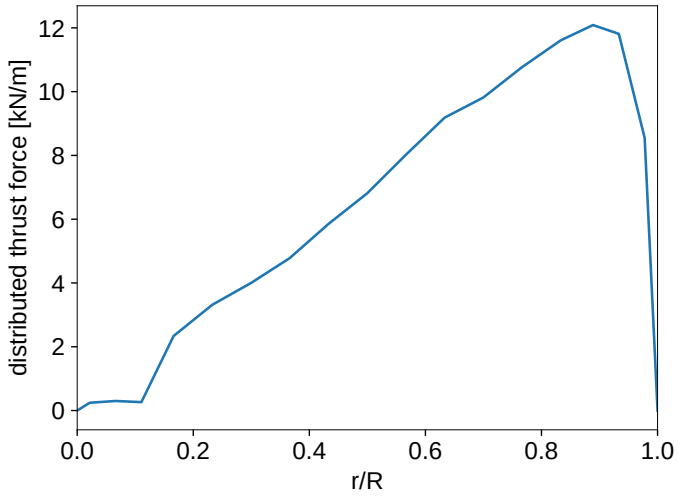

Figure B.2: Aerodynamic load applied, corresponding to the rated power aerodynamic load of the SNL 100-00.

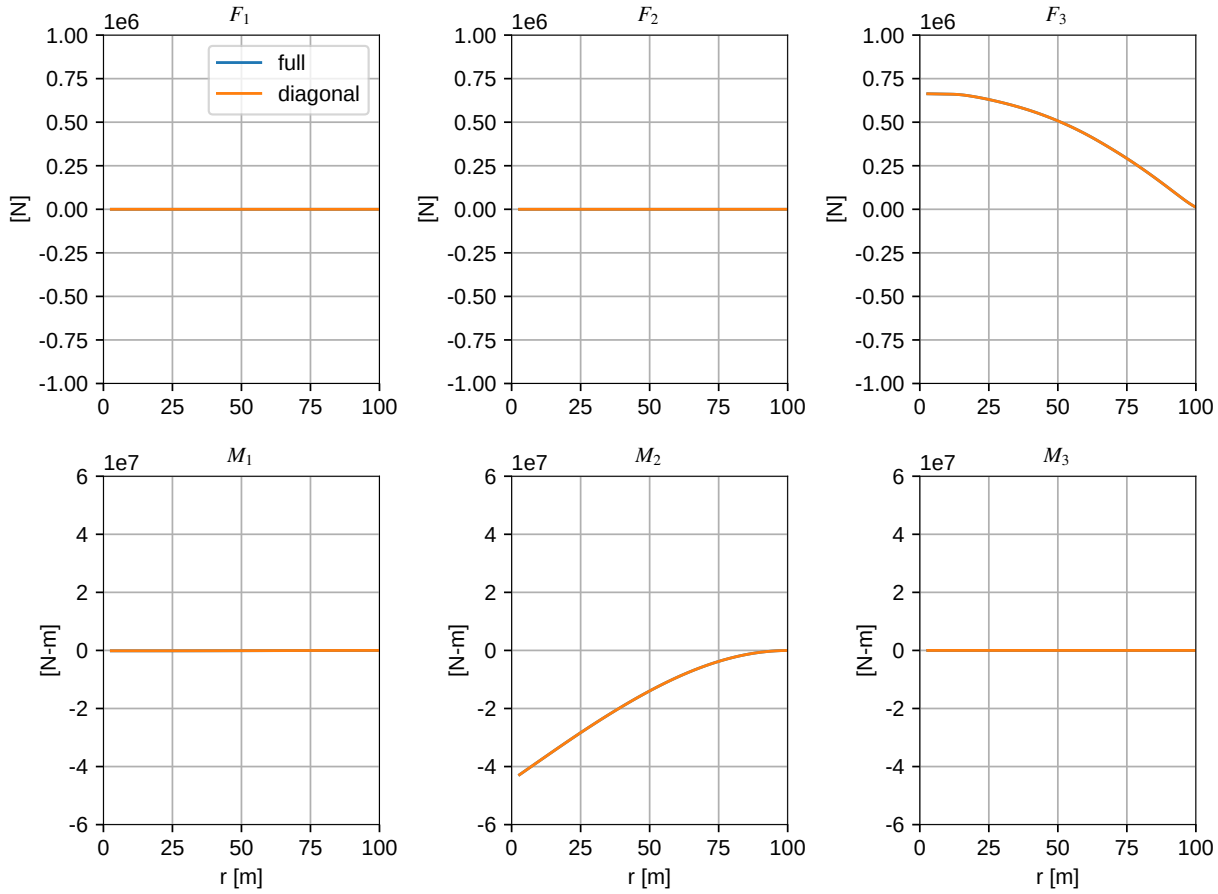

Figure B.3: Comparison of deflections for SNL 100-00 blade using "full" and "diagonal" stiffness matrix sets. Force axis directions are 1 – beam-aligned, 2 – flapwise, 3 – edgewise.

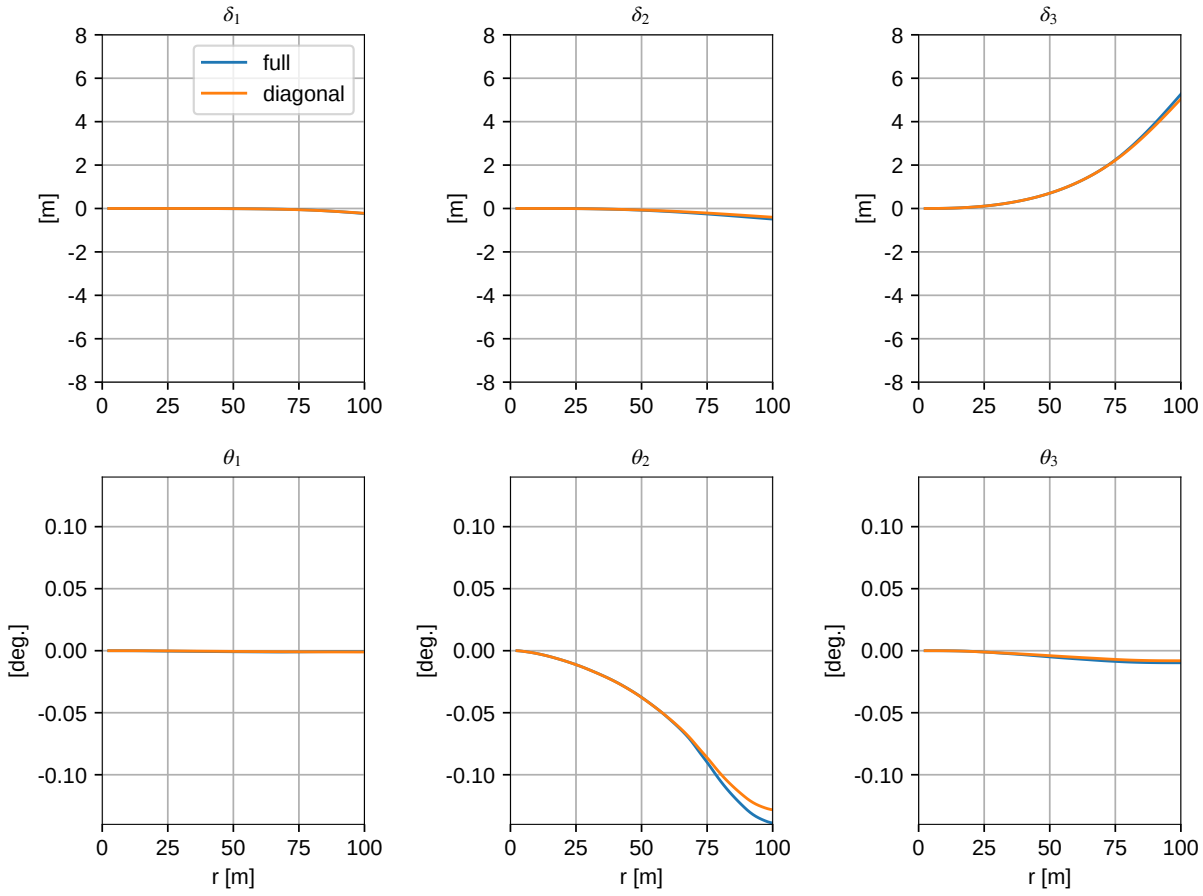

Figure B.4: Comparison of deflections for SNL 100-00 blade using "full" and "diagonal" stiffness matrix sets. Displacement axis directions are 1 – beam-aligned, 2 – flapwise, 3 – edgewise.

APPENDIX C

PolyCX Validation

C.1 Comparison of cross sectional properties against other tools

The cross sectional analysis tool PolyCX was developed for this effort. In this section, the cross sectional properties (stiffnesses and mass per length) are compared against data published by Sandia National Laboratories cross sectional data for the SNL 100-00 blade [14]. PolyCX is used to generate cross sectional geometries from the material width and thickness definitions of the SNL 100-00 blade. These cross sectional geometries are shown for select locations in Appendix C.1.

The cross sectional properties are then computed using PolyCX. The bending stiffnesses, extensional stiffness, and mass per unit length are compared against the Sandia data in Appendix C.1. The Sandia data was computed using the NREL tool PreComp [102], which uses modified form of classical laminate theory. Good agreement is shown between the two methods, especially with regards to the mass and flapwise bending moment. The Sandia data is seen to have higher edgewise bending stiffness and extensional stiffness, particularly inboard. This is likely due to geometrical differences between the Sandia cross sections and those generated by PolyCX – the Sandia cross sections have a third shear web which is not included in the PolyCX cross section geometry.

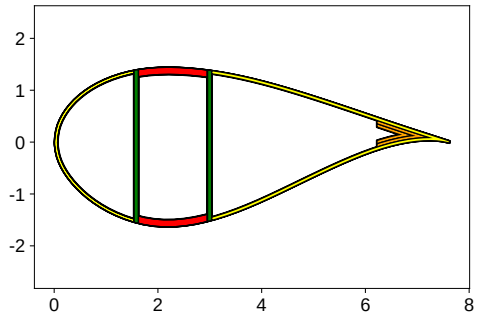

(a) 19.5 m

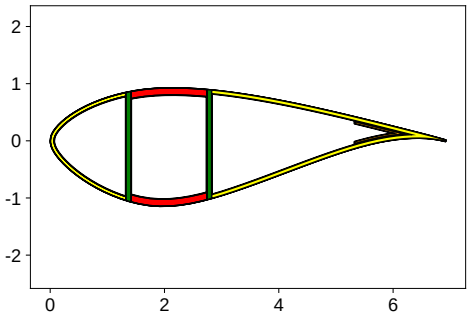

(b) 35.8 m

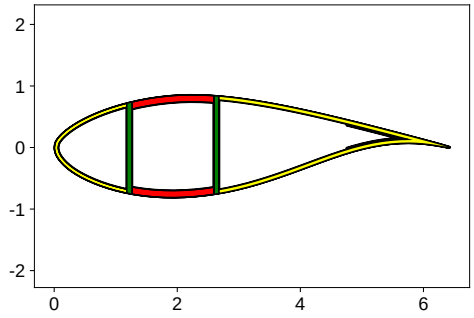

(c) 43.9 m

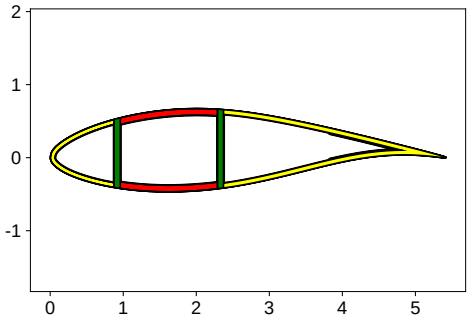

(d) 60.2 m

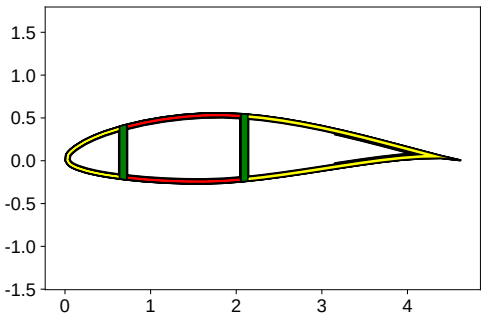

(e) 73.2 m

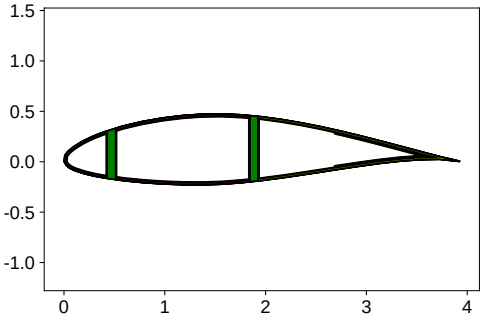

(f) 84.6 m

Figure C.1: Select cross sectional profiles of the SNL 100-00 blade for validation, generated by PolyCX.

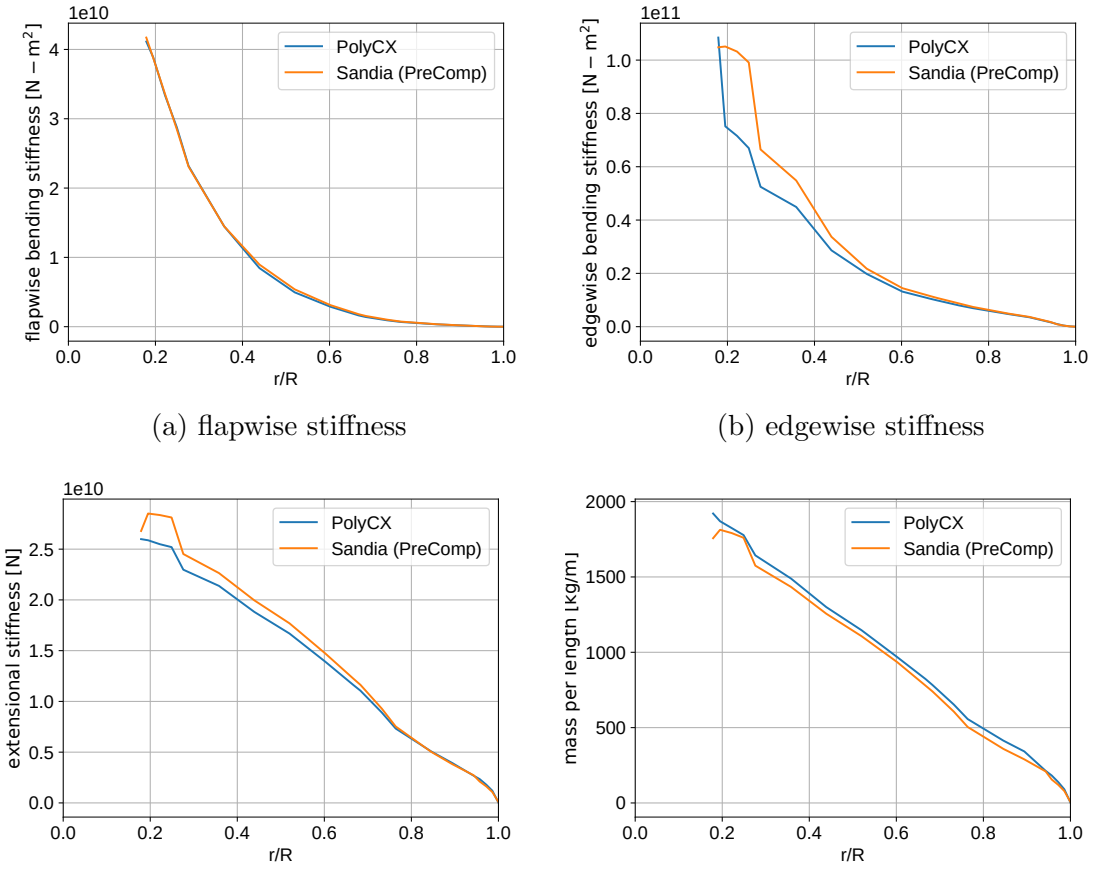

(a) flapwise stiffness

(b) edgewise stiffness

(c) extensional stiffness

(d) mass/length

Figure C.2: Comparison of PolyCX and Sandia (PreComp) computed stiffnesses and mass/length for the SNL 100-00 blade.

REFERENCES

[1] J. Jonkman, S. Butterfield, W. Musial, and G. Scott, "Definition of a 5-MW reference wind turbine for offshore system development," Tech. Rep. NREL/TP-500-38060, National Renewable Energy Laboratory, Golden, CO, 2009.

[2] NREL, "Estimates of Land Area1 and Wind Energy Potential, by State, for areas ¿= 35% Capacity Factor at 80, 110, and 140m." http://apps2.eere.energy.gov/wind/windexchange/docs/wind{_}potential{_}80m{_}110m{_}140m{_}35percent.xlsx, 2014.

[3] NREL, "U.S. 50m - Wind Resource Map." http://www.nrel.gov/gis/pdfs/windsmodel4pub1-1-9base200904enh.pdf, 2009.

[4] S. Lindenberg, B. Smith, and K. O'Dell, "20% Wind energy by 2030," Tech. Rep. DOE/GO-102008-2567, U.S. Department of Energy, Energy Efficiency and Renewable Energy, Oak Ridge, TN, 2008.

[5] U.S. Energy Information Administration, "Electric Power Monthly." http://www.eia.gov/electricity/monthly/current{_}year/december2014.pdf, 2014.

[6] G. Sieros, P. Chaviaropoulos, J. D. Sørensen, B. H. Bulder, and P. Jamieson, "Upscaling wind turbines: theoretical and practical aspects and their impact on the cost of energy," *Wind Energy*, vol. 15, pp. 3–17, 2012.

[7] P. M. S. Roth-Johnson, *Aero-Structural Design Investigations for Biplane Wind Turbine Blades*. Phd, University of California, Los Angeles, 2014.

[8] E. Hau and H. von Renouard, *Wind Turbines*. Berlin, Heidelberg: Springer Berlin Heidelberg, 2006.

[9] B. C. Larsen, "Østerild - National Test Centre for Large Wind Turbines - DTU Wind Energy." http://www.vindenergi.dtu.dk/English/About/Oesterild.aspx.

[10] Renewable Energy World Editors, "Meet The New World's Biggest Wind Turbine." http://www.renewableenergyworld.com/rea/news/article/2014/02/meet-the-new-worlds-biggest-wind-turbine.

[11] W. turbine models.com, "Samsung S7.0-171 - 7.000,0 kW - Turbine." http://en.wind-turbine-models.com/turbines/285-samsung-s7.0-171.

[12] 4C Offshore, "Offshore Wind Turbine: S7.0-171, Samsung Heavy Industries." http://www.4coffshore.com/windfarms/turbine-samsung-heavy-industries-shi-7-mw-tid37.html.

[13] Enercon GmbH, "E-126 / 7,580 kW — ENERCON." http://www.enercon.de/en-en/66.htm.

[14] D. T. Griffith and T. D. Ashwill, "The Sandia 100-meter All-glass Baseline Wind Turbine Blade: SNL100-00," Tech. Rep. SAND2011-3779, Sandia National Laboratories, Albuquerque, NM, 2011.

[15] J. Peeringa, R. Brood, and O. Ceyhan, "Upwind 20 MW Wind Turbine Pre-Design," Tech. Rep. ECN-E–11-017, 2012.

[16] P. Jamieson, *Innovation in Wind Turbine Design*. Chichester, UK: John Wiley & Sons, Ltd, aug 2011.

[17] D. T. Griffith, "The SNL100-01 Blade: Carbon Design Studies for the Sandia 100-meter Blade," Tech. Rep. SAND2013-1178, Sandia National Laboratories, Albuquerque, NM, 2013.

[18] UpWind, "Design limits and solutions for very large wind turbines - A 20 MW turbine is feasible," Tech. Rep. ECN-E–11-017, UpWind, 2011.

[19] K. J. Jackson, M. D. Zuteck, C. P. van Dam, K. J. Standish, and D. Berry, "Innovative Design Approaches for Large Wind Turbine Blades," *Wind Energy*, vol. 8, pp. 141–171, apr 2005.

[20] M. Gaunaa, F. Zahle, N. N. Sørensen, C. Bak, and P.-e. Réthoré, "Rotor Performance Enhancement Using Slats on the Inner Part of a 10MW Rotor," in *European Wind Energy Association Conference 2013*, (Vienna), pp. 1–10, 2013.

[21] J. Johansen, H. A. Madsen, M. Gaunaa, C. Bak, and N. N. Sørensen, "Design of a wind turbine rotor for maximum aerodynamic efficiency," *Wind Energy*, vol. 12, pp. 261–273, 2009.

[22] M. Gaunaa, F. Zahle, N. N. Sørensen, and C. Bak, "Quantification of the Effects of Using Slats on the Inner Part of a 10MW Rotor," in *European Wind Energy Conference 2012*, (Copenhagen), pp. 1–12, 2012.

[23] A. Rosenberg, S. Selvaraj, and A. Sharma, "A Novel Dual-Rotor Turbine for Increased Wind Energy Capture," *Journal of Physics: Conference Series*, vol. 524, pp. 1–10, 2014.

[24] C. L. Bottasso, F. Campagnolo, and A. Croce, "Multi-disciplinary constrained optimization of wind turbines," in *Multibody System Dynamics*, vol. 27, pp. 21–53, 2012.

[25] M. Jureczko, M. Pawlak, and A. Mezyk, "Optimisation of wind turbine blades," *Journal of Materials Processing Technology*, vol. 167, pp. 463–471, aug 2005.

[26] N. Buckney, A. Pirrera, S. D. Green, and P. M. Weaver, "Structural efficiency of a wind turbine blade," *Thin-Walled Structures*, vol. 67, pp. 144–154, jun 2013.

[27] N. Buckney, S. Green, A. Pirrera, and P. M. Weaver, "On the structural topology of wind turbine blades," *Wind Energy*, vol. 16, pp. 545–560, may 2013.

[28] C.-H. Ong and S. W. Tsai, "The Use of Carbon Fibers in Wind Turbine Blade Design: A SERI-8 Blade Example," Tech. Rep. SAND2000-0478, Sandia National Laboratories, Albuquerque, NM, 2000.

[29] W. Timmer and R. van Rooy, "Thick airfoils for HAWTs," *Journal of Wind Engineering and Industrial Aerodynamics*, vol. 39, pp. 151–160, jan 1992.

[30] J. Tangler and D. Somers, "NREL airfoil families for HAWTs," in *AWEA Windpower*, no. 1, pp. 1–12, 1995.

[31] W. A. Timmer and R. P. J. O. M. van Rooij, "Some aspects of high angle-of-attack flow on airfoils for wind turbine application," *Journal of Solar Energy Engineering*, vol. 125, no. 4, pp. 4–7, 2003.

[32] P. Fuglsang, C. Bak, M. Gaunaa, and I. Antoniou, "Design and Verification of the Risø-B1 Airfoil Family for Wind Turbines," *Journal of Solar Energy Engineering*, vol. 126, no. 4, p. 1002, 2004.

[33] K. J. Standish and C. P. van Dam, "Aerodynamic Analysis of Blunt Trailing Edge Airfoils," *Journal of Solar Energy Engineering*, vol. 125, no. 4, p. 479, 2003.

[34] D. D. Chao and C. P. van Dam, "Computational aerodynamic analysis of a blunt trailing-edge airfoil modification to the NREL Phase VI rotor," *Wind Energy*, vol. 10, pp. 529–550, nov 2007.

[35] F. Grasso, "Hybrid Optimization for Wind Turbine Thick Airfoils," in *53rd AIAA/ASME/ASCE/AHS/ASC Structures, Structural Dynamics and Materials Conference*, no. 1354, (Honolulu, HI), pp. 1–12, 2012.

[36] A. M. Ragheb and M. S. Selig, "Multi-Element Airfoil Configurations for Wind Turbines," in *29th AIAA Applied Aerodynamics Conference*, no. June, (Honolulu, HI), pp. 1–13, AIAA, 2011.

[37] S. Narsipur, B. Pomeroy, and M. Selig, "CFD Analysis of Multielement Airfoils for Wind Turbines," in *30th AIAA Applied Aerodynamics Conference*, no. June, (Reston, Virigina), pp. 1–18, American Institute of Aeronautics and Astronautics, jun 2012.

[38] D. Eisenberg, "Secondary airfoil mounted on stall fence on wind turbine blade." U.S. Patent: 8777580B2, issued date April 15, 2014.

[39] R. E. Wirz and P. M. Johnson, "Aero-Structural Performance of Multiplane Wind Turbine Blades," in *29th AIAA Applied Aerodynamics Conference*, (Honolulu, HI), pp. 1–15, AIAA, 2011.

[40] P. Grabau, "Blade for a wind turbine rotor." U.S. Patent: US8469672B2, issued date June 25, 2013.

[41] M. Brodsgaard, *Biplane wing sections for wind turbines*. Msc thesis, DTU, 2012.

[42] P. Roth-Johnson, R. E. Wirz, and E. Lin, "Structural design of spars for 100-m biplane wind turbine blades," *Renewable Energy*, vol. 71, pp. 133–155, nov 2014.

[43] M. Zyskowski, "Incorporating biplane wing theory into a large, subsonic, all-cargo transport," in *Aircraft Engineering, Technology, and Operations Congress*, (Reston, Virginia), American Institute of Aeronautics and Astronautics, sep 1995.

[44] J. Wolkovitch, "The joined wing - An overview," *Journal of Aircraft*, vol. 23, pp. 161–178, Mar. 1986.

[45] P. Roth-Johnson and R. E. Wirz, "Aero-structural investigation of biplane wind turbine blades," *Wind Energy*, vol. 17, pp. 397–411, Mar. 2014.

[46] P. Chiu and R. E. Wirz, "Optimal Aerodynamic Design of a Biplane Wind Turbine Blade," in *34th Wind Energy Symposium*, (Reston, Virginia), pp. 1–14, American Institute of Aeronautics and Astronautics, Jan. 2016.

[47] S. Chatterjee and R. J. Templin, "Biplane wing planform and flight performance of the feathered dinosaur Microraptor gui.," *Proceedings of the National Academy of Sciences of the United States of America*, vol. 104, pp. 1576–80, jan 2007.

[48] B. P. Selberg and K. Rokhsaz, "Disadvantages of thin airfoil formulations for closely coupled airfoils," *Journal of Aircraft*, vol. 20, no. 6, pp. 1982–1984, 1983.

[49] F. Norton, "The effect of staggering a biplane," Tech. Rep. NACA-TN-70, National Advisory Committee for Aeronautics, 1921.

[50] M. Knight and R. Noyes, "Wind tunnel pressure distribution tests on a series of biplane wing models Part I: Effects of changes in stagger and gap," Tech. Rep. NACA-TN-310, National Advisory Committee for Aeronautics, 1929.

[51] M. Knight and R. Noyes, "Wind tunnel pressure distribution tests on a series of biplane wing models Part II: Effects of changes in decalage, dihedral, sweepback and overhang," Tech. Rep. NACA-TN-325, National Advisory Committee for Aeronautics, 1929.

[52] M. Knight and R. Noyes, "Wind tunnel pressure distribution tests on a series of biplane wing models Part III: effects of charges in various combinations of stagger, gap, sweepback, and," Tech. Rep. NACA-TN-330, National Advisory Committee for Aeronautics, 1929.

[53] M. Nenadović, *Recherches sur les cellules biplanes rigides d'envergure infinie*. E. Blondel la Rougery, 1936.

[54] M. Munk, "General Biplane Theory," Tech. Rep. NACA-TR-151, National Advisory Committee for Aeronautics, 1923.

[55] C. Millikan, "An extended theory of thin airfoils and its application to the biplane problem," Tech. Rep. NACA-TR-362, National Advisory Committee for Aeronautics, 1931.

[56] L. Milne-Thomson, *Theoretical aerodynamics*. New York: Dover Publications, 4th ed., 1973.

[57] J. Katz and A. Plotkin, *Low Speed Aerodynamics*. New York: Cambridge University Press, second ed., 2001.

[58] G. McBain, *Theory of Lift: Introductory Computational Aerodynamics in MATLAB/Octave*. Hoboken, NJ: Wiley, 2012.

[59] K. Rokhsaz, *Aerodynamic study of dual lifting surfaces*. M.s. thesis, University of Missouri-Rolla, 1980.

[60] M. Lagally, "Die reibungslose Strömung im Außengebiet zweier Kreise," *ZAMM - Zeitschrift für Angewandte Mathematik und Mechanik*, vol. 9, no. 4, pp. 299–305, 1929.

[61] I. Garrick, "Potential Flow About Arbitrary Biplane Wing Sections," Tech. Rep. NACA-TR-542, National Advisory Committee for Aeronautics, Langley Field, VA, 1937.

[62] D. C. Ives, "A Modern Look at Conformal Mapping Including Multiply Connected Regions," *AIAA Journal*, vol. 14, pp. 1006–1011, aug 1976.

[63] B. Fornberg, "A Numerical Method for Conformal Mapping of Doubly Connected Regions," *SIAM Journal on Scientific and Statistical Computing*, vol. 5, pp. 771–783, dec 1984.

[64] D. Crowdy, "Calculating the lift on a finite stack of cylindrical aerofoils," *Proceedings of the Royal Society A: Mathematical, Physical and Engineering Sciences*, vol. 462, pp. 1387–1407, may 2006.

[65] M. Hepperle, "JavaFoil User's Guide." `http://www.mh-aerotools.de/airfoils/java/JavaFoilUsersGuide.pdf`, 2014.

[66] M. Gaunaa, N. Sørensen, and C. Bak, "Thick Multiple Element Airfoils for use on the Inner Part of Wind Turbine Rotors," in *The Science of Making Torque From Wind*, pp. 135–152, 2010.

[67] T. Burton, N. Jenkins, D. Sharpe, and E. Bossanyi, *Wind Energy Handbook*. Chichester, UK: John Wiley & Sons, Ltd, 2011.

[68] M. Drela, "A User's Guide to MSES 3.05," tech. rep., MIT Department of Aeronautics and Astronautics, 2007.

[69] L. A. Viterna and D. C. Janetzke, "Theoretical and experimental power from large horizontal-axis wind turbines," Tech. Rep. NASA TM-82944, NASA, Cleveland, Ohio, 1982.

[70] Z. Du and M. Selig, "A 3-D stall-delay model for horizontal axis wind turbine performance prediction," in *1998 ASME Wind Energy Symposium*, (Reston, Virigina), American Institute of Aeronautics and Astronautics, jan 1998.

[71] A. J. Eggers, K. Chaney, and R. Digumarthi, "An Assessment of Approximate Modeling of Aerodynamic Loads on the UAE Rotor," in *ASME 2003 Wind Energy Symposium*, pp. 283–292, ASME, 2003.

[72] J. Cotrell, T. Stehly, J. Johnson, J. O. Roberts, Z. Parker, G. Scott, and D. Heimiller, "Analysis of Transportation and Logistics Challenges Affecting the Deployment of Larger Wind Turbines: Summary of Results," Tech. Rep. NREL/TP-5000-61063, National Renewable Energy Laboratory, Golden, CO, 2014.

[73] A. D. Platt and M. L. Buhl, "WT_Perf User Guide for Version 3.05.00," tech. rep., National Wind Technology Center, National Renewable Energy Laboratory, Golden, CO, 2012.

[74] W. D. Musial, R. E. Sheppard, D. Dolan, and B. Naughton, "Development of Offshore Wind Recommended Practice for US Waters," in *Offshore Technology Conference*, Offshore Technology Conference, may 2013.

[75] S. Andrew Ning, R. Damiani, and P. J. Moriarty, "Objectives and Constraints for Wind Turbine Optimization," *Journal of Solar Energy Engineering*, vol. 136, no. 4, p. 041010, 2014.

[76] P. K. Chiu and R. E. Wirz, "Biplane Wind Turbine Blades - Aerodynamic Design, Performance, and Loads," *Wind Energy*, vol. Submitted, 2017.

[77] O. A. Bauchau, "DYMORE 4 User's Manual." `http://soliton.ae.gatech.edu/people/obauchau/`, jun 2010.

[78] J. F. Mandell and D. D. Samborsky, "DOE/MSU Composite Material Fatigue Database-Test, Methods, Materials, and Analysis," 1997.

[79] S. Gillies, "The Shapely User Manual Shapely 1.2 and 1.3 documentation." `http://toblerity.org/shapely/manual.html`.

[80] "GEOS - Geometry Engine, Open Source." `https://trac.osgeo.org/geos/`.

[81] C. E. S. Cesnik and D. H. Hodges, "VABS: A New Concept for Composite Rotor Blade Cross-Sectional Modeling," *Journal of the American Helicopter Society*, vol. 42, no. 1, p. 27, 1997.

[82] W. Yu, "VABS Manual for Users," tech. rep., feb 2010.

[83] J. P. Blasques, R. D. Bitsche, V. Fedorov, and B. S. Lazarov, "Accuracy of an efficient framework for structural analysis of wind turbine blades," *Wind Energy*, vol. 19, pp. 1603–1621, sep 2016.

[84] D. T. Griffith, "The SNL100-02 Blade: Advanced Core Material Design Studies for the Sandia 100- meter Blade," Tech. Rep. SAND2013-10162, Sandia National Laboratories, Albuquerque, NM, 2013.

[85] D. T. Griffith and P. W. Richards, "The SNL100-03 Blade: Design Studies with Flatback Airfoils for the Sandia 100-meter Blade," Tech. Rep. September, Sandia National Laboratories, Albuquerque, NM, 2014.

[86] E. Jones, T. Oliphant, P. Peterson, *et al.*, "SciPy: Open source scientific tools for Python." `http://www.scipy.org/`, 2001–.

[87] D. Kraft, "A software package for sequential quadratic programming," Tech. Rep. DFVLR-FB 88-28, 1988.

[88] J. Jonkman and M. Buhl, "FAST User's Guide," Tech. Rep. NREL/TP-500-38230, National Wind Technology Center, National Renewable Energy Laboratory, Golden, CO, 2005.

[89] "BLADED, Theory Manual," tech. rep., DNV GL, 2014.

[90] L. Wang, X. Liu, and A. Kolios, "State of the art in the aeroelasticity of wind turbine blades: Aeroelastic modelling," *Renewable and Sustainable Energy Reviews*, vol. 64, pp. 195–210, 2016.

[91] A. Elliott and A. Wright, "ADAMS/WT: An industry-specific interactive modelling interface for wind turbine analysis," *The Energy-Sources Technology Conference, New*, 1994.

[92] V. Riziotis and S. Voutsinas, "GAST: A general aerodynamic and structural prediction tool for wind turbines," *EWEC-*, 1997.

[93] M. H. Hansen, "Aeroelastic instability problems for wind turbines," *Wind Energy*, vol. 10, pp. 551–577, nov 2007.

[94] M. O. L. Hansen and H. Aagaard Madsen, "Review Paper on Wind Turbine Aerodynamics," *Journal of Fluids Engineering*, vol. 133, no. 11, p. 114001, 2011.

[95] B. Sanderse, S. P. Van Der Pijl, and B. Koren, "Review of computational fluid dynamics for wind turbine wake aerodynamics," *Wind Energy*, vol. 14, no. February, pp. 799–819, 2011.

[96] H. Himmelskamp, *Profile investigations on a rotating airscrew.* Volkenrode MAP, 1947.

[97] P. K. Chaviaropoulos and Others, "Investigating three-dimensional and rotational effects on wind turbine blades by means of a quasi-3D Navier-Stokes solver," *Journal of Fluids Engineering*, vol. 122, p. 330, 2000.

[98] M. Drela and M. Giles, "Viscous-inviscid analysis of transonic and low Reynolds number airfoils," *AIAA Journal*, vol. 25, no. 10, 1986.

[99] M. Drela, *XFOIL: An analysis and design system for low Reynolds number airfoils.* Springer Berlin Heidelberg, 1989.

[100] E. C. Maskell, "A theory of the blockage effects on bluff bodies and stalled wings in a closed wind tunnel," Tech. Rep. R&M No. 3400, Ministry of Aviation, Aeronautical Research Council, London, 1963.

[101] J. B. Barlow, W. H. Rae, and A. Pope, *Low-speed wind tunnel testing*. Wiley New York, 1999.

[102] G. S. Bir, "User's guide to PreComp (pre-processor for computing composite blade properties)," Tech. Rep. NREL/TP-500-39929, National Renewable Energy Laboratory, Golden, CO, 2006.